



Uni-Parser Technical Report

DP Technology *

December 16, 2025

 <https://uni-parser.github.io>
 <https://huggingface.co/UniParser>

Abstract

This technical report introduces *Uni-Parser*, an industrial-grade document parsing engine tailored for scientific literature and patents, delivering high throughput, robust accuracy, and cost efficiency. Unlike pipeline-based document parsing methods, Uni-Parser employs a modular, loosely coupled multi-expert architecture that preserves fine-grained cross-modal alignments across text, equations, tables, figures, and chemical structures, while remaining easily extensible to emerging modalities. The system incorporates adaptive GPU load balancing, distributed inference, dynamic module orchestration, and configurable modes that support either holistic or modality-specific parsing. Optimized for large-scale cloud deployment, Uni-Parser achieves a processing rate of up to 20 PDF pages per second on $8 \times$ NVIDIA RTX 4090D GPUs, enabling cost-efficient inference across billions of pages. This level of scalability facilitates a broad spectrum of downstream applications, ranging from literature retrieval and summarization to the extraction of chemical structures, reaction schemes, and bioactivity data, as well as the curation of large-scale corpora for training next-generation large language models and AI4Science models.

1 Introduction

The rapid advancement of large language models (LLMs) has significantly expanded the scope of document-centric applications, ranging from intelligent assistants and domain-specific agents to automated knowledge base construction. Central to these developments is the ability to reliably parse and structure information from PDF documents, which remain the dominant medium for disseminating scientific knowledge. High-quality structured data extracted from scientific literature is particularly critical for downstream LLM applications, enabling accurate reasoning, retrieval-augmented generation, and decision-making across a wide spectrum of scientific and industrial tasks.

Among scientific domains, chemical and biomedical literature holds exceptional importance and immense commercial value. Parsing such documents enables the creation of comprehensive molecular and reaction databases, bioactivity repositories, material structure archives, and experimental characterization datasets. These resources not only accelerate drug discovery and materials design but also serve as the foundation for emerging AI4Science research. However, despite decades of progress in OCR, table recognition, and layout analysis, the majority of the hundreds of millions of scientific and patent PDFs remain underexploited. This is largely because the PDF format, while optimized for human readability, poses extraordinary challenges for computational processing: extraction is prohibitively costly.

Current approaches, both pipeline-based [1–4] and VLM-based [5–11], face three major challenges. First, they are computationally inefficient, making it prohibitively costly to parse tens of millions of

* Full authorship contribution statements appear at the end of the document.

documents at scale. Second, their performance on non-textual modalities such as formulas, tables, charts, and chemical structures remains limited, with low accuracy and poor robustness. Third, the complex and heterogeneous layouts of scientific and patent documents often lead to unreliable segmentation and structural analysis, further degrading downstream usability. Pipeline methods offer higher throughput but poor generalization, while VLM methods generalize better but suffer from low efficiency and limited extensibility. Collectively, these limitations hinder the construction of large-scale, high-quality knowledge bases required for both academic research and industrial innovation.

To address these challenges, we present *Uni-Parser*, an industrial-grade, multi-modal PDF parsing engine purpose-built for scientific literature and patents. Uni-Parser follows the pipeline-based methods, and combines high throughput with state-of-the-art accuracy through a modular, loosely coupled architecture composed of specialized expert models for different modalities. The system introduces a set of key innovations:

- **High-efficiency large-scale inference:** A distributed microservice design with dynamic GPU load balancing enables real-time parsing throughput, supporting fast and cost-effective inference over billions of document pages.
- **Accurate multi-modal parsing:** A suite of domain-specialized, lightweight expert models achieves state-of-the-art accuracy across text, equations, tables, figures, and chemical structures.
- **Robust layout recognition for scientific and patent documents:** A newly designed layout analysis and reading order algorithm tailored to complex publishing formats greatly improves reliability in handling dense, irregular, and domain-specific page structures.

Together, these contributions establish Uni-Parser as a scalable and extensible foundation for structured document understanding. By transforming unstructured PDFs into clean, machine-actionable representations, Uni-Parser not only supports immediate applications such as literature retrieval, summarization, and knowledge extraction, but also enables the construction of domain-specific repositories in chemistry, materials science, and biomedicine—paving the way for data-driven AI4Science innovation.

2 Algorithm Framework

2.1 Overall Framework

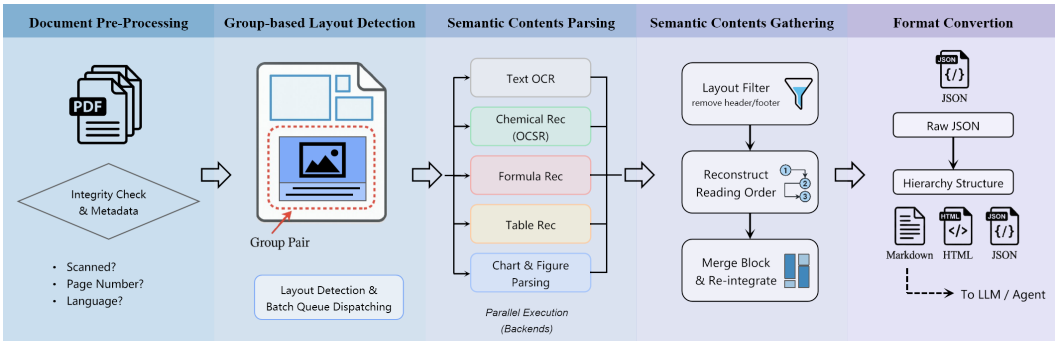


Figure 1: Sketch of the Uni-Parser pipeline. Uni-Parser converts unstructured PDFs into clean, hierarchical, multimodal outputs (text, formulas, tables, figures, and chemical structures). These enriched representations are designed to be readily consumed by large language models, enabling more accurate understanding, reasoning, and document-level operations.

Uni-Parser adopts a modular design with a strong emphasis on extensibility. As shown in the figure, it first conducts validation and pre-processing on PDF file inputs. It then converts these unstructured documents into machine-readable formats (e.g., JSON) or LLM-compatible representations (e.g., Markdown and HTML) through a sequence of models and processing stages. These stages are organized into five principal components:

Document Pre-Processing: During pre-processing, the system ingests PDFs from user uploads or URLs, verifies file integrity and encryption, and extracts metadata such as page count, dimensions, and text accessibility. Documents with corrupted or garbled text are marked as non-extractable. If embedded text layers exist, they are directly extracted; otherwise, a lightweight OCR method provides partial text for language identification. Uni-Parser supports over 80 languages for OCR mode. This stage typically takes around one hundred milliseconds and supports parallel processing of multiple PDFs.

Group-based Layout Detection: The layout detection model locates each semantic block in the PDF pages and identifies its semantic category. Unlike conventional approaches [2, 3], our group-based layout detection model recognizes naturally paired semantic components—such as image–caption, table–title, and molecule–identifier—preserving visual–semantic associations that are critical for structured information extraction and accurate reading-order construction. Finally, different semantic blocks are rendered at dynamic resolutions and forwarded to designated models for image-to-text processing. We employ a greedy batch-stacking strategy for rendering page images, performing layout recognition, and dispatching semantic groups to downstream microservices. As soon as a batch accumulates in the queue, it is immediately processed by subsequent modules, allowing the latency of this stage to be almost entirely masked by other processing steps.

Semantic Contents Parsing: Semantic contents are parsed by routing each block to the appropriate specialized model. General text blocks are processed with OCR, tables with table recognition models, mathematical formulas with formula recognition models, molecular structures with optical chemical structure recognition (OCSR), chemical reactions with dedicated reaction extraction models, and charts with chart parsing models. In total, over ten sub-models and specialized procedures handle diverse content types, including text, tables, molecular structures, chemical reactions, formulas, and charts. All models operate in parallel to maximize efficiency. For image blocks, the system can retain either visual descriptions or raw image data, depending on downstream application requirements. This stage is the most time-consuming stage.

Semantic Contents Gathering: Building on the parsed results from the previous stage, this phase filters out non-essential elements such as headers and footers while preserving key combinations like figure–caption or table–caption pairs and horizontal separators. Content blocks within each page are reordered to reflect the logical structure of the document. Multimodal elements embedded in text lines or table cells—such as inline equations, chemical structures, or charts—are reintegrated into their corresponding text or table. Cross-page and multi-column content, including tables, paragraphs, and reaction schemes, is merged to maintain coherence. The system also incorporates the original PDF’s section hierarchy to guide the final organization. The output of this stage provides a fully structured, semantically enriched representation of the document, suitable for downstream analysis and reading-order reconstruction.

Output Formatting and Semantic Chunking: To support diverse downstream tasks, the fully parsed document can be exported in task-specific formats, or as a complete plain text, interleaved image–text, Markdown, or HTML. Thanks to group-based layout detection and the merging of semantic content across columns and pages, reconstructed paragraphs or semantic groups are output as properly chunked data, which improves semantic coherence. This approach streamlines chunking and facilitates more efficient downstream processing, such as retrieval-augmented generation (RAG). Furthermore, PDF section headings are integrated into the document structure when available. These metadata elements enrich the final representation with hierarchical navigation cues, improving both user-facing applications and LLM-driven analysis.

2.2 Group-based Layout Analysis

Layout detection is a foundational prerequisite for all subsequent document analysis tasks and represents a pivotal component within document parsing systems. Its efficacy ultimately establishes the performance ceiling for the entire system. Acknowledging the profound diversity and complexity of scientific document layouts, along with the critical importance of grouping relationships among heterogeneous semantic elements, we introduce a layout understanding paradigm that diverges significantly from conventional approaches [1, 2, 12, 13]: a group-based tree-structured layout representation.

Operationally, we conceptualize the layout of a document page as a hierarchical organization, enabling the aggregation of semantically related elements into coherent and logical groups. For instance, figures are paired with their captions, tables with their titles, equations with their reference numbers, and molecular structures with their identifiers, among other relational pairings. Figure 2 shows an example of the layout tree structure. Although document layouts inherently involve multiple levels of hierarchy, in our annotation we restrict the structure to only two layers: the bottom layer and the top layer. The bottom layer covers all fundamental semantic components, serving as the parent nodes of the layout structure tree, whereas the top layer comprises content nested within the bottom layer or other top level semantic elements, functioning as child nodes. The corresponding semantic categories are summarized in Table 1. Importantly, this design still allows downstream post-processing to recover the nested semantic content across multiple hierarchical levels. Based on these concepts, we constructed a group-based layout detection model named *Uni-Parser-LD*.

Table 1: Layout type used in Uni-Parser-LD

Layout Type	Layout Layer	Role	Semantic Parsing Category
Document Title		Main Text & Structure Role	OCR
Section Title		Main Text & Structure Role	OCR
Paragraph		Main Text	OCR
References	Bottom Layer	Supplementary Text	OCR
Table of Contents		Supplementary Text	OCR
Key-value Item		Main Text	OCR
Code Block		Figure / Multi-modal Text	OCR / Code Parsing
Header		Functional Role	–
Footer		Functional Role	–
Footnote		Supplementary Text	OCR
Sidebar	Bottom Layer	Functional Role	–
Page Number		Functional Role	OCR
Watermark		Functional Role	–
Divider Line		Functional Role	–
Formula ¹		Multi-modal Text	Formula Recognition
Table ²	Bottom Layer	Multi-modal Text	Table Structure Recognition
Image ³		Figure / Multi-modal Text	-
Formula (Inline)		Multi-modal Text	Formula Recognition
Molecule ⁴		Multi-modal Text	OCSR
Chemical Reaction ⁵	Top Layer	Figure / Multi-modal Text	Reaction Parsing
Chart ⁵		Figure / Multi-modal Text	Chart to Table
Figure ⁵		Figure / Multi-modal Text	Image Caption

¹ Grouped with formula ID.

² Grouped with table caption and table footnote.

³ Grouped with image caption.

⁴ Grouped with molecule identifier and Markush description.

⁵ Grouped with figure legend and figure caption.

Considering the wide variety of authoring and rendering styles across layouts and modalities, we employ a large-scale dataset of PDF pages for training. We built an in-house layout detection dataset containing 500k pages. Of these, 220k pages are carefully human annotated with group-based layout labels from a diverse corpus. The database primarily consists of scientific journal data and patent data from various patent offices. It also includes preprints, books, and other types of data across different fields, spanning a total of 85 languages. For more details, refer to Section 4. The remaining pages are synthetic data used for pretraining. Our experiments show that when high-quality, large-scale real data is available, pretraining with existing synthetic datasets, such as DocSynth300K [12], can be counterproductive. This is due to their low-fidelity rendering, stylistic deviations from authentic documents, and limited diversity imposed by manually defined generation rules, which fail to capture the complexity of real-world layouts. To address this, we generate synthetic samples from real layouts using controlled modifications—including element merging, spatial perturbations, and semantic content substitutions—allowing the model to effectively leverage synthetic data for pretraining.

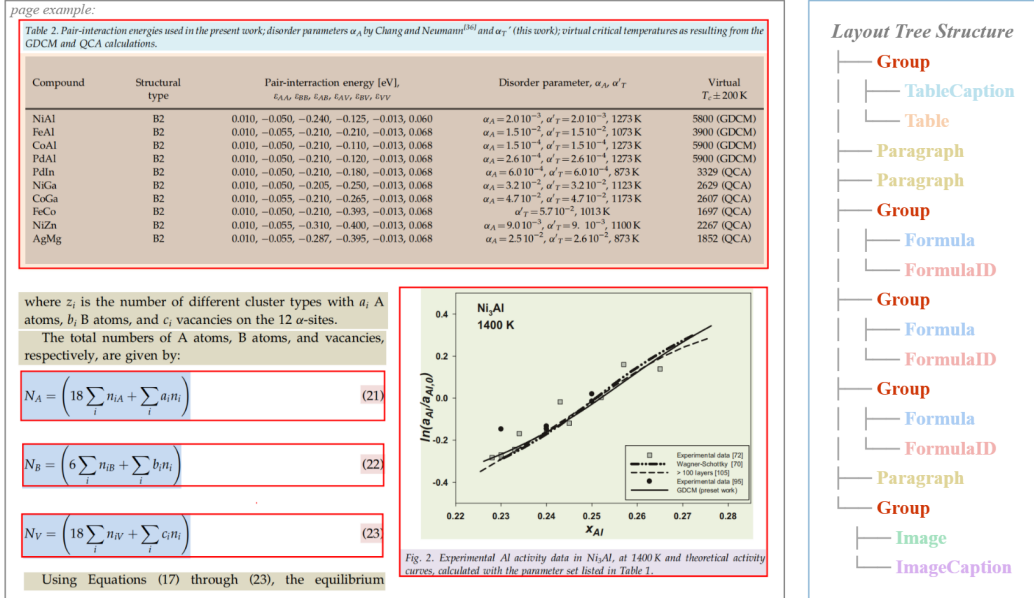


Figure 2: An inference example of group-based layout detection used Uni-Parser-LD. The final output is a hierarchical layout tree structure.

To meet real-time processing requirements, our selection of a backbone architecture for layout detection prioritizes high efficiency. A survey of contemporary object detection methods reveals that models such as RT-DETRv2 [14], YOLOv12 [15], and D-FINE [16] can exhibit training instability in our layout detection task. Meanwhile, the extensive modifications made to YOLOv8 [17] in DocLayout-YOLO [12] yield only marginal performance improvements in our setting. Consequently, after balancing performance with inference speed, we select a modified DETR-based architecture as the backbone for our group-based layout detection model.

The choice of input resolution presents another critical trade-off between processing speed and detection accuracy. While prior research [18] suggests that a resolution of 896×896 suffices for most documents, our empirical evaluations demonstrate its insufficiency for achieving consistently high performance. Therefore, to accommodate diverse document aspect ratios and strike a superior balance between speed and accuracy, we adopt an input resolution of 1024×768 .

2.3 OCR

Uni-Parser operates in two complementary OCR modes: extraction and recognition. When textual content can be directly extracted from the PDF in the first stage, the system bypasses OCR and utilizes the extracted text directly. Otherwise, or when explicitly requested by the user, Uni-Parser performs recognition using OCR model, such as the PP-OCRv5 [2] series. The default OCR backbone supports a broad character set encompassing Simplified and Traditional Chinese, English, Japanese, and a wide range of special symbols. For other languages, the system automatically invokes the corresponding language-specific PP-OCRv5 model. For more complex cases—such as multilingual mixtures or documents containing numerous out-of-vocabulary OCR symbols—we additionally support switching to PaddleOCR-VL [19] in a high-quality mode, trading inference speed for improved robustness in challenging scenarios, with support for more than 109 languages (ISO 639). In practice, additional preprocessing is applied in certain scenarios. For example, when text is embedded within tables, Uni-Parser employs a text orientation detector to ensure accurate recognition.

After OCR, the system reconstructs the document by aligning recognized text with the spatial layout returned by the layout detection module. Inline non-textual elements—such as chemical structures and mathematical expressions embedded within text lines—are explicitly identified and preserved. Shown in Figure 3, during OCR, these elements are temporarily replaced with modality-specific placeholders, which are subsequently parsed by dedicated modules (e.g., OCSR or formula recognition) and reintegrated into the final semantic representation of the document.

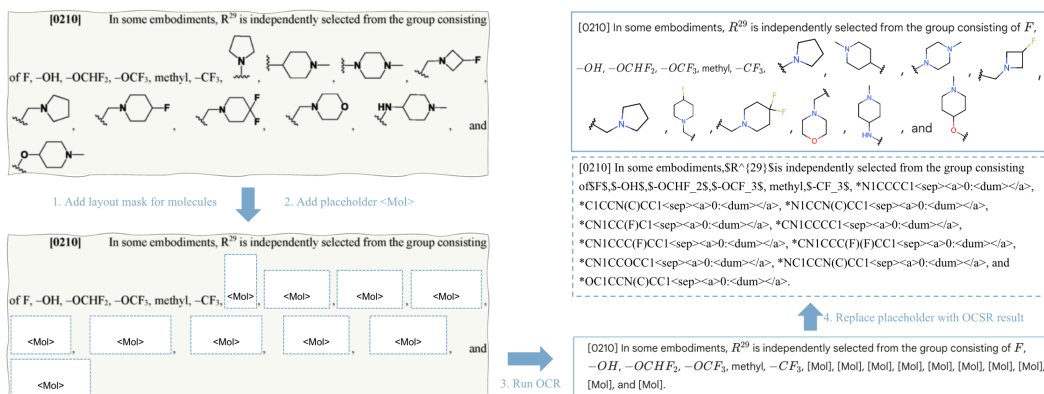


Figure 3: An example of the OCR model inference workflow in Uni-Parser. When a top-layer layout element overlaps a bottom-layer layout block, the system substitutes it with a placeholder before performing OCR. The placeholder is then resolved during post-processing, enabling fast and accurate multimodal parsing.

2.4 Table Structure Recognition

Tables represent compact yet structurally complex layouts, as each cell may contain heterogeneous semantic blocks, including plain text, mathematical formulas, molecular structures, reaction schemes, images, or even nested sub-tables. The presence of such multi-level nesting makes it challenging for a single end-to-end model to perform generalized OCR on tables. To address this, we adopt a modular strategy that decouples table structure recognition from multimodal content parsing. This approach not only improves interpretability but also enhances robustness and overall performance.

Before structure recognition, Uni-Parser recovers the orientation of tables, since rotated layouts frequently occur in patents and supplementary materials of scientific articles, particularly when tables are extended across pages. Instead of employing a dedicated orientation model, we leverage layout predictions and auxiliary metadata to perform lightweight orientation recovery, achieving accuracy comparable to that of specialized models while significantly improving efficiency.

We adopt an efficient table structure recognition model, SLANet [20], trained on a corpus of one million tables that integrates a cleaned version of PubTabNet [21], SynthTabNet [22], and our in-house synthetic dataset of line-based tables enriched with multimodal content. The synthetic dataset covers both bordered and borderless formats and incorporates diverse elements, including molecule structures, charts, images, formulas, and text. This comprehensive training strategy allows SLANet to achieve strong generalization and superior performance on complex real-world table layouts.

MOLSTRUCTURE	COMPOUND NAME	IC50
	3-[(2-CHLORO-BENZOYL)-METHYL-AMINO]-5-PHENYL-THIOPHENE-2-CARBOXYLIC ACID	++
	3-[(2-METHYL-BENZOYL-AMINO)-5-PHENYL-THIOPHENE-2-CARBOXYLIC ACID	++
	3-[(METHYL-(2-METHYL-BENZOYL)-AMINO)-5-PHENYL-THIOPHENE-2-CARBOXYLIC ACID	+

Figure 4: An example of table structure recognition results produced by Uni-Parser. By decoupling table structure recognition from table content recognition, the system achieves improved robustness, supports multimodal nesting within tables.

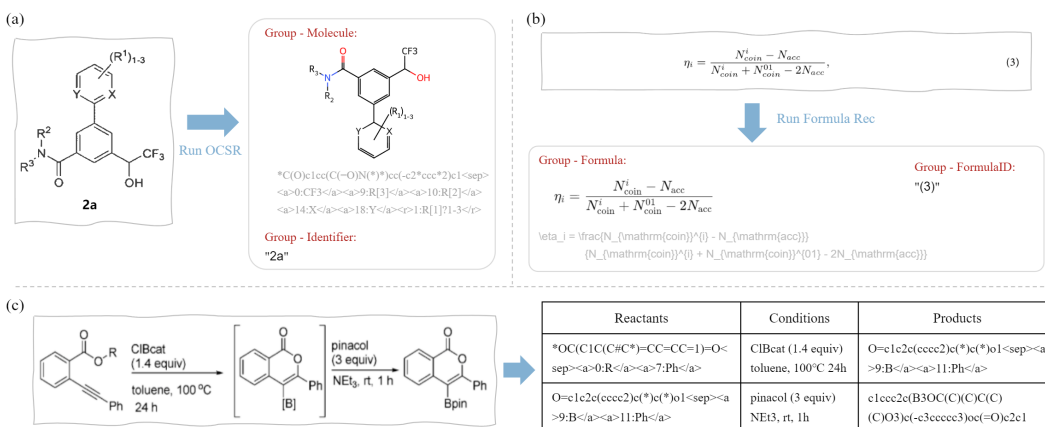


Figure 5: Examples of multi-modal recognition results produced by Uni-Parser. (a) Molecular structures are correctly associated with their corresponding identifiers. (b) Mathematical formulas are accurately linked to their formula IDs. (c) An organic chemical reaction is parsed into a structured reactant–condition–product triplet.

2.5 Formula Recognition

The system integrates a mathematical formula recognition module fine-tuned from PP-Formula [2]. The module converts mathematical expressions and chemical equations into LaTeX sequences in an end-to-end manner. It handles both standalone formulas and inline formulas or equations within paragraph text. For standalone formulas, the layout stage groups the expression with its reference number to form a structured representation.

2.6 Chemical Expression Recognition

Chemical structures are a fundamental modality in scientific literature and patents, particularly in chemistry, pharmaceuticals, biology, and materials. Uni-Parser adopts the end-to-end OCSR architecture MolParser [23] for molecular recognition, which translates molecular images into an Extended SMILES (E-SMILES) representation. We further introduce *MolParser 1.5*, which extends MolParser with an expanded pretraining corpus. In addition to the synthetic MolParser-7M dataset, we add a real-world dataset of 10 million images pseudo-labeled via cross-validation using multiple MolParser models and a fine-tuned MolScribe [24]. With a larger proportion of in-the-wild chiral molecules and Markush structures, MolParser 1.5 yields a more balanced and comprehensive pretraining dataset, and after fine-tuning on the MolParser-SFT dataset, it produces a more robust end-to-end OCSR model.

For chemical reaction image recognition, we adopt a pipeline approach. First, we detect the texts and molecular structures within the reaction in layout stage. Then, we identify the associations among blocks to construct a reactant–condition–product graph. Finally, we aggregate the results to obtain the parsed reaction equation.

2.7 Chart and Scientific Figure Understanding

Uni-Parser incorporates an optional module for chart and scientific figure understanding. When activated, the system converts charts into their underlying data tables. For figures that are not amenable to accurate tabular representation—such as spectra or complex scientific diagrams—the system generates detailed image captions that convey essential information, including key numerical values.

For chart understanding, we fine-tuned a Qwen-2.5-VL-3B [25] model on a dataset consisting of 500k generated samples, 300k open-source samples, and 170k real-world charts. This training significantly enhances the model’s ability to convert charts into tables, with a particular focus on multi-subplot charts, which frequently appear in scientific literature.

To support accurate scientific figure captioning, we curated a large-scale, high-quality dataset of 4 million samples. The core of this dataset consists of 3 million scientific images meticulously collected from high-impact publications. To enhance caption quality, we leveraged multiple multi-modal large language models (MLLMs), including but not limited to GPT-5 [26] and Gemini 2.5 [27], to rewrite the original captions by integrating visual content with raw captions and relevant contextual information from the associated papers. The dataset is further augmented with additional sources, including ChemPile [28], molecular descriptions from PubChem, Electron Microscopy image captions [29], and other experimental characterization datasets. Leveraging this comprehensive dataset, we fine-tuned a Qwen-2.5-VL-3B model, which named as *SciParser*, enabling it to generate precise, context-aware captions for a diverse range of scientific figures.

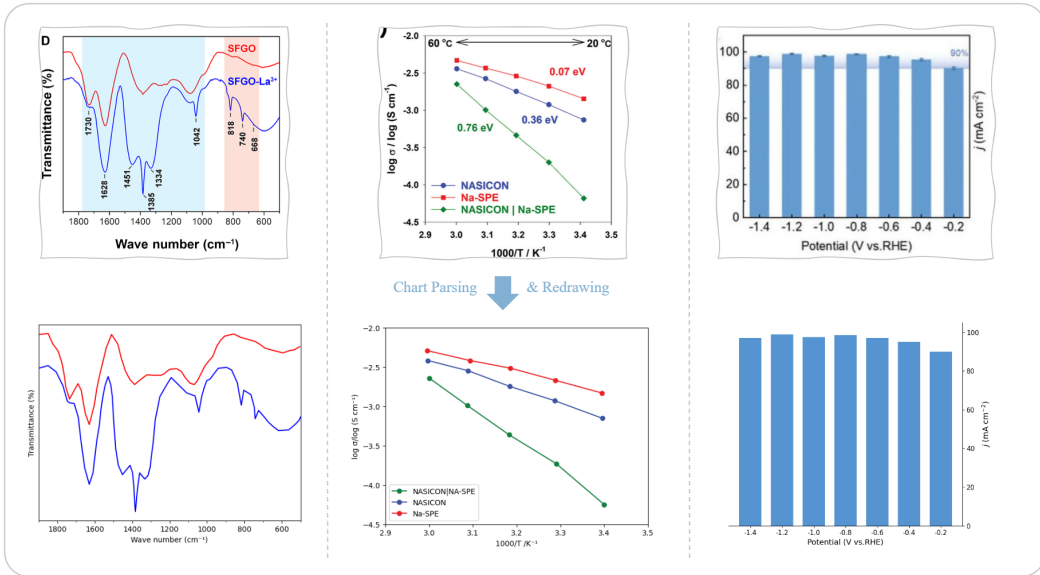


Figure 6: Examples of chart recognition results produced by Uni-Parser. Chart images are first parsed into underlying data tables, which are then re-rendered in a style consistent with the original figures for visualization and presentation.

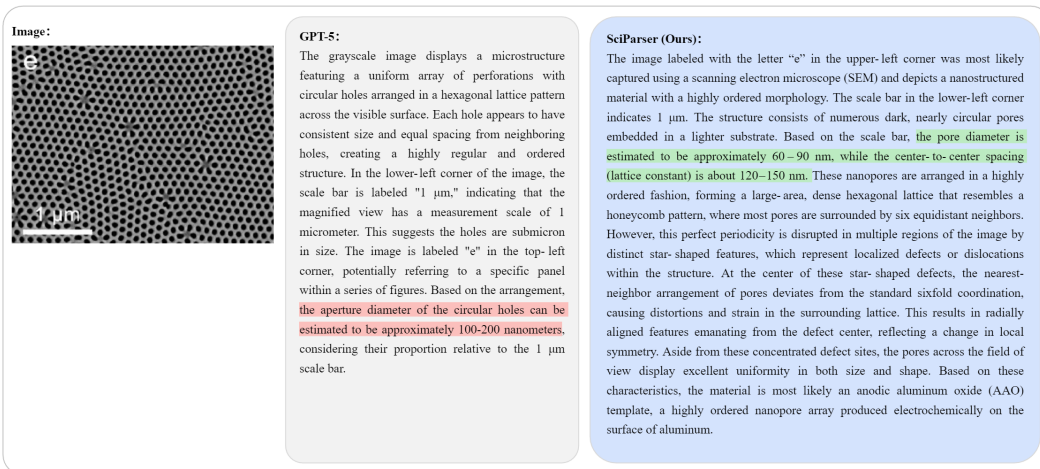


Figure 7: Examples of scientific figure captioning results produced by Uni-Parser. SciParser, a dedicated scientific image captioning submodule within Uni-Parser, converts scientific figures into high-information-density textual descriptions that capture key semantic and structural attributes, facilitating downstream understanding, retrieval, and database construction.

2.8 Reading Order Recovery

To accurately reconstruct the reading order of content blocks on each page, our system integrates a set of spatial and semantic heuristics tailored for complex, real-world documents.

XY-cut. This method recursively partitions the page along dominant whitespace regions, yielding a hierarchical binary reading tree that captures coarse layout structure.

Gap-tree analysis. It leverages inter-block whitespace, geometric proximity, and alignment cues to infer plausible reading flows, particularly in dense or irregular layouts.

Group-based strategies. These strategies cluster semantically related elements—even when spatially distant—such as linking figures with captions or molecules with identifiers, thereby preserving logical semantics prior to global ordering.

By combining these complementary techniques, the system produces a natural and coherent reading sequence across multi-column, multi-lingual, and multi-modal layouts.

2.9 Cross-column and Cross-page Consolidation

After establishing the per-page reading order, the system further consolidates items that are visually separated but semantically continuous:

- **Cross-column merging:** reconnecting paragraph fragments split by column boundaries using text-flow continuity and linguistic coherence.
- **Cross-page merging:** linking entities that span pages—such as long tables, multi-step reaction schemes, or running paragraphs—based on layout carry-over cues and semantic consistency.
- **Multimodal linkage:** Associating diagrams with their corresponding identifiers or descriptions, even when they appear on adjacent pages. Representative examples are provided in Appendix B.2.

This second-stage consolidation restores logically unified content into coherent units, improving the fidelity of the reconstructed document structure.

3 Infrastructure

3.1 Distributed Multi-Expert Architecture

Microservice architecture: Uni-Parser adopts a microservice-based multi-expert architecture that enables large-scale distributed inference. Each modality-specific expert (e.g., text, molecules, formulas, tables, reactions, and charts) is deployed as an independent microservice, with multiple nodes running in parallel to process inference requests. Layout analysis first partitions documents into batches, which are distributed across nodes for concurrent processing. Detected regions are then enqueued into modality-specific task queues, where batched requests are asynchronously dispatched to the corresponding expert services. Finally, outputs from all modules are aggregated into a unified generalized OCR representation, followed by post-processing and structured result generation.

Dynamic load balancing: A fine-grained scheduling layer dynamically allocates computational resources both within and across modules. This design supports adaptive scaling under varying workloads, prevents bottlenecks in individual experts, and ensures stable throughput in heterogeneous multi-modal parsing.

Pipeline Parallel: The inference runtime is optimized for efficient GPU parallelism and scheduling, employing multi-process server execution, micro-batching, and asynchronous task management to minimize idle time and sustain high GPU occupancy, while simultaneously ensuring effective utilization of CPU and memory resources across heterogeneous workloads. In particular, CPU pre-processing and post-processing, GPU model inference, and inter-service data transfer are orchestrated in a pipelined manner, enabling time-overlapping execution across stages and thereby further reducing latency in each instance. An analysis of bubble time is presented in Figure 8.

Decoupled module updates: Independent component upgrades that support rapid iteration and performance tuning without full system redeployment, with zero service interruption during updates.

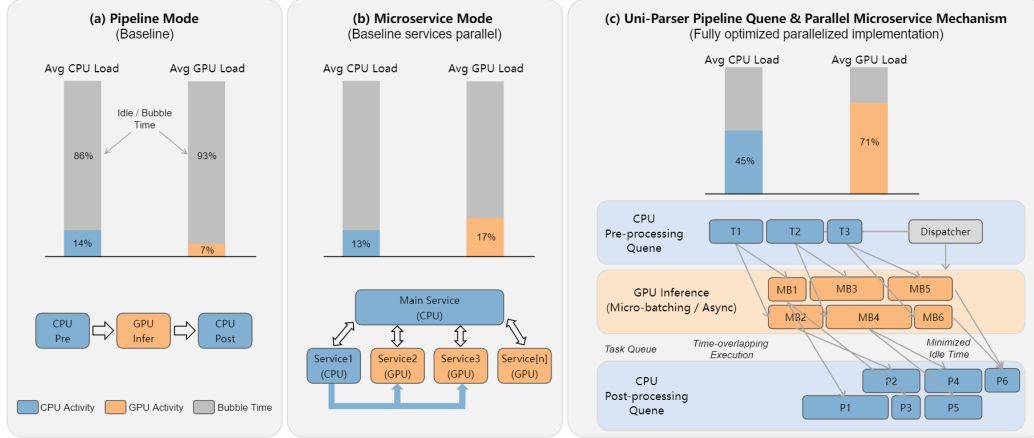


Figure 8: Comparison of document parsing infrastructures. (a) Sequential pipeline: Most existing document parsing frameworks adopt a strictly serial workflow, in which layout analysis is completed first, followed by generalized OCR tasks and subsequent post-processing. (b) Microservice-based parallelism: The tasks are dispatched to multiple microservices that operate in parallel, and the final results are aggregated through a gather stage. (c) Our Uni-Parser pipeline-parallel design: By enabling more frequent lightweight communication and non-blocking execution across modules, Uni-Parser fully exploits parallelism across heterogeneous microservices. Computation and communication are effectively overlapped across GPU and CPU resources, substantially improving throughput and reducing end-to-end latency.

This enables a self-reinforcing data flywheel loop, allowing models to be updated on an hourly basis and continuously enhanced with newly acquired active learning samples.

3.2 Deployment Scaling

Uni-Parser is designed for elastic scaling in distributed inference environments. System throughput can be increased almost linearly by expanding the number of nodes assigned to each load-balanced microservice. Benchmark experiments demonstrate that the average parsing speed per PDF page scales almost linearly with the number of backend GPUs.

The Uni-Parser system is deployed on a cluster of 240 NVIDIA L40 GPUs (48 GB each), with 22 CPU cores and 90 GB of host memory per GPU. Under this setting, Uni-Parser parses over 16 million documents within 6 days in the fast mode. Moreover, the system scales to a hybrid cluster of up to 1,000 GPUs (A800 + L20), exhibiting near-linear throughput scaling with respect to available computational resources. These results indicate that Uni-Parser provides a computationally efficient, scalable, and stable infrastructure for large-scale document parsing.

4 Data Engineering

4.1 Uni-Parser Data Engine

The *Uni-Parser Data Engine* is designed to efficiently generate and curate high-quality training data for PDF parsing models, combining synthetic generation, active learning on real documents, and self-training on unlabeled data to minimize human annotation effort while maintaining high accuracy.

Step 1: Synthetic Data for Model Bootstrapping. Since all PDFs are human-generated rather than naturally structured, we employ large-scale synthetic data to bootstrap various models, including layout detection and several generalized OCR models. Diverse synthetic documents are generated and augmented extensively to pretrain models, providing a strong initialization that accelerates downstream learning and improves generalization.

Step 2: Active Learning on Real Documents. After endowing the model with fundamental capabilities using large-scale synthetic data, we further improve its performance by iteratively

incorporating real-world documents through an active learning framework. Our in-house training corpus is curated from multiple high-quality sources, including:

- approximately 170 million pages of scientific literature spanning a broad range of disciplines;
- over 140 million pages of patent documents collected from patent offices worldwide;
- around 20 million pages of books, technical reports, and miscellaneous documents obtained from Fine-PDFs [30].

An active learning data flywheel, similar to the one used in MolParser [23], is employed to select the most informative samples for annotation. Specifically, cross-model inference consistency is used as the primary scoring criterion to estimate sample uncertainty and guide data selection during each active learning cycle. In addition, this process is integrated with a curriculum learning strategy, whereby the model is progressively trained on examples of increasing structural and semantic complexity, enabling stable optimization and improved generalization in challenging real-world scenarios.

Step 3: Self-Training on Unlabeled Data. To further scale training without additional manual labeling, we apply self-training on large collections of unlabeled documents. Predictions from multiple ensembled models are aggregated to estimate confidence scores, and only high-confidence predictions are treated as pseudo-labels. This approach effectively expands the training set at minimal cost while maintaining label quality.

By combining synthetic pretraining, active learning, and self-training, we construct a data flywheel that substantially reduces the amount of human annotations required, accelerates model convergence, and enables high-throughput, low-cost data preparation. Using this three-step approach, we reduce the total annotation volume by 95% and cut per-page or per-block annotation time by 90%, with 90% of annotations for our various models completed in just two months, ensuring rapid, scalable, and efficient model development for large-scale PDF parsing tasks.

4.2 Uni-Miner Annotation Platform

To better establish a data flywheel for Uni-Parser with an effective human-in-the-loop pipeline, we designed the *Uni-Miner Annotation Platform* to ensure that samples selected through active learning can be corrected and refined by human annotators with high quality and low cost. The platform integrates a molecular drawing interface and supports annotation across multiple modalities, including molecular structures, text, and layout elements. In addition, we incorporate a recommendation module that assigns the most suitable samples to domain experts based on their specialization and past performance. Each annotator and reviewer is dynamically scored according to accuracy metrics, enabling the system to route the most critical or ambiguous cases to the most experienced and reliable individuals. This design significantly reduces annotation cost, improves throughput, and ensures consistent data quality through mechanisms such as inter-annotator agreement monitoring. In practice, each sample is reviewed by at least two annotators, providing further quality assurance for the downstream learning process.

5 Performance

5.1 Construction of the Uni-Parser Benchmark

The Uni-Parser benchmark is designed to evaluate layout detection and semantic content recognition in scientific documents. It comprises 150 PDF files collected from international patent documents and research articles, with an emphasis on diversity in document structure, subject matter, domain, and language. The distribution of the benchmark is summarized in Table 2. To ensure high data quality, the benchmark is annotated by more than ten domain experts, followed by two rounds of cross-review and an additional round of random quality inspection.

5.2 Overall Results

We evaluate scientific document parsing performance using an end-to-end evaluation protocol following OmniDocBench [31]. The *Overall* metric excludes molecular-related scores, as existing baselines

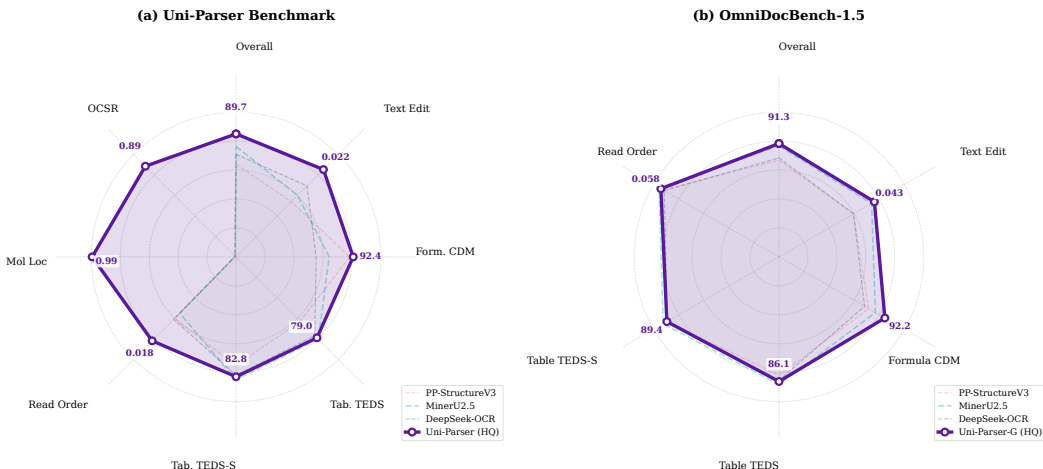


Figure 9: Performance comparison of Uni-Parser with representative document parsing systems across two benchmarks. (a) Uni-Parser Benchmark, a benchmark proposed in this work to evaluate multimodal parsing capabilities on scientific documents and patent literature. (b) OmniDocBench-1.5 [31], a general-purpose benchmark for document parsing. Uni-Parser demonstrates strong and well-balanced performance across most evaluation dimensions, indicating favorable overall capability and robustness compared to existing methods.

Table 2: Distribution of document sources in Uni-Parser benchmark.

Source Type	Sub-Source	#PDFs	Total Pages
Patent Documents	From 20 Patent Offices (5 langs)	50	1455
	xRxiv (bioRxiv, medRxiv, ChemRxiv, etc.)	35	696
	arxiv	20	231
Scientific Articles	ChinaXiv	15	168
	Nature Communications	15	164
	Scientific Reports	15	173
Total (All Documents)		150	2887

generally lack molecular recognition and localization capabilities and therefore consistently obtain zero scores on these components. Table 3 reports the comparative results on the proposed Uni-Parser benchmark.

Table 3: Performance comparison of scientific document parsing methods on Uni-Parser Benchmark

Type	Methods	Overall \uparrow <i>excl. Mol.</i>	Text \downarrow <i>Edit</i>	Form. \uparrow <i>CDM</i>	Tab. \uparrow <i>TEDS</i>	Tab. \uparrow <i>TEDS-S</i>	Read Order \downarrow <i>Edit</i>	Mol Loc \uparrow <i>mAP@50</i>	OCSR \uparrow <i>Acc</i>
Pipeline Tools	MinerU2-pipeline 2.1.1 [3]	83.24	0.063	86.14	69.88	78.25	0.065	0.000	0.000
	PP-StructureV3 [2]	82.41	0.069	91.42	62.71	75.21	0.040	0.000	0.000
	Uni-Parser (Fast)	83.06	0.061	91.74	63.54	74.97	0.047	0.994	0.886
	Uni-Parser (HQ)	89.74	0.022	92.37	79.04	82.79	0.018	0.994	0.886
Specialized VLMs	MinerU2-VLM [3]	84.93	0.049	85.09	74.60	79.43	0.041	0.000	0.000
	MinerU2.5 [3]	86.72	0.060	85.73	80.41	84.82	0.045	0.000	0.000
	DeepSeek-OCR [32]	84.80	0.046	82.13	76.88	81.72	0.039	0.000	0.000
	PaddleOCR-VL [19]	89.80	0.034	90.59	82.21	84.91	0.030	0.000	0.000

We further report results on OmniDocBench-1.5 [31], although this benchmark is not fully aligned with the core strengths of Uni-Parser. It mainly targets broad non-academic document domains (e.g., presentations and newspapers) and exhibits noticeable annotation noise. Nevertheless, for completeness, we include this evaluation. Leveraging the modular design of Uni-Parser, we replace

the layout analysis module with PP-DocLayoutV2 [19] to accommodate this general-document OCR setting. In Table 4, this variant is denoted as *Uni-Parser-G*.

Table 4: Performance comparison of general document parsing methods on OmniDocBench-1.5 [31].

Model Type	Methods	Overall \uparrow	Text ^{Edit} \downarrow	Formula ^{CDM} \uparrow	Table ^{TEDS} \uparrow	Table ^{TEDS-S} \uparrow	Read Order ^{Edit} \downarrow
Pipeline Tools	Marker-1.8.2 [33]	71.30	0.206	76.66	57.88	71.17	0.250
	MinerU2-pipeline [3]	75.51	0.209	76.55	70.90	79.11	0.225
	PP-StructureV3 [2]	86.73	0.073	85.79	81.68	89.48	0.073
	Uni-Parser-G (Fast)	83.00	0.087	82.16	75.55	83.78	0.131
	Uni-Parser-G (HQ)	91.33	0.043	92.23	86.06	89.42	0.058
General VLMs	GPT-4o	75.02	0.217	79.70	67.07	76.09	0.148
	InternVL3-76B [34]	80.33	0.131	83.42	70.64	77.74	0.113
	InternVL3.5-241B [34]	82.67	0.142	87.23	75.00	81.28	0.125
	Qwen2.5-VL-72B [25]	87.02	0.094	88.27	82.15	86.22	0.102
	Gemini-2.5 Pro	88.03	0.075	85.82	85.71	90.29	0.097
Specialized VLMs	Dolphin [35]	74.67	0.125	67.85	68.70	77.77	0.124
	OCRFlux-3B [36]	74.82	0.193	68.03	75.75	80.23	0.202
	Mistral OCR [11]	78.83	0.164	82.84	70.03	78.04	0.144
	POINTS-Reader [37]	80.98	0.134	79.20	77.13	81.66	0.145
	olmOCR-7B [38]	81.79	0.096	86.04	68.92	74.77	0.121
	MinerU2-VLM [3]	85.56	0.078	80.95	83.54	87.66	0.086
	Nanonets-OCR-s [39]	85.59	0.093	85.90	80.14	85.57	0.108
	MonkeyOCR-pro-1.2B [8]	86.96	0.084	85.02	84.24	89.02	0.130
	DeepSeek-OCR (9-crops) [32]	87.36	0.073	84.14	85.25	89.01	0.085
	MonkeyOCR-3B [8]	87.13	0.075	87.45	81.39	85.92	0.129
	dots.ocr [10]	88.41	0.048	83.22	86.78	90.62	0.053
	MonkeyOCR-pro-3B [8]	88.85	0.075	87.25	86.78	90.63	0.128
	MinerU2.5 [3]	90.67	0.047	88.46	88.22	92.38	0.044
	PaddleOCR-VL [19]	92.86	0.035	91.22	90.89	94.76	0.043

Overall, Uni-Parser demonstrates a clear performance advantage in parsing scientific and patent documents. Its modular design enables adaptation to diverse document types while maintaining competitive accuracy, together with industrial-grade inference speed and robustness, making it well suited for large-scale deployment.

Additional qualitative results are provided in the appendix. Appendix B.3 highlights Uni-Parser-LD’s more fine-grained layout categorization, stronger group and sub-figure localization, and support for molecular structure localization. Appendix B.4 demonstrates robust reading-order determination under complex layouts via a rule-based strategy, while Appendix B.5 presents overall comparisons with other PDF parsing frameworks.

5.3 Chemical Structure Parsing

Chemical structures play a pivotal role in conveying molecular information, making their accurate recognition crucial for applications ranging from drug discovery and materials design to knowledge extraction from patents and scientific literature. However, most existing document parsing systems provide limited or no support for chemical structure recognition. To address this gap, Uni-Parser integrates two specialized submodels: *Uni-Parser-LD*, which tackles molecular localization within layout detection, and *MolParser 1.5*, which handles chemical structure recognition.

We evaluate Uni-Parser on both the Uni-Parser Benchmark and the recent third-party BioVista benchmark [40]. As shown in Table 5a, our group-based layout detection model, Uni-Parser-LD, outperforms our previous state-of-the-art molecular detection model, MolDet [23], while also establishing correspondences between molecules and their identifiers—a capability absent in MolDet. Table 5b shows that MolParser 1.5 consistently surpasses its predecessor across all benchmark subsets, delivering notable improvements in both accuracy and inference speed over mainstream open-source OCSR methods. Moreover, our approach remains highly competitive against costly commercial models [41, 42]. Representative case studies are provided in Appendix B.1.

To further evaluate the capability of existing PDF parsing frameworks in handling chemical structures, we conduct a controlled comparison on a small test set of 141 simple molecules (excluding Markush structures). Since batch access to competing systems is not feasible, we restrict the evaluation to this limited set. We compare four key metrics: (i) molecule localization recall, (ii) the proportion of successfully parsed molecules (OCSR success rate), (iii) the final recognition accuracy, and (iv) molecule-identifier matching rate. As shown in Table 6, Uni-Parser achieves consistently strong

Table 5: Comparison of chemical structure detection and recognition performance.

(a) Molecule location performance			(b) OCSR accuracy for different types of molecules				
Model	mAP@50	mAP@50-95	Model	Full	Chiral	Markush	All
<i>Uni-Parser Benchmark</i>			<i>Uni-Parser Benchmark</i>				
Uni-Parser-LD	0.994	0.968	MolParser 1.5	0.979	0.809	0.805	0.886
MolDet-Doc-L[23]	0.983	0.919	MolParser 1.0[23]	0.953	0.676	0.664	0.800
MolDet-General-L[23]	0.974	0.815	MolScribe[24]	0.617	0.274	0.168	0.417
<i>BioVista Benchmark</i>			<i>BioVista Benchmark</i>				
Uni-Parser-LD	0.981	0.844	MolParser 1.5	0.800	0.622	0.769	0.786
MolDet-Doc-L[23]	0.961	0.871	MolParser 1.0[23]	0.669	0.352	0.733	0.703
MolDet-General-L[23]	0.945	0.815	MolMiner[43]	0.774	0.497	0.185	0.507
BioMiner[40]	0.929	-	MolScribe[24]	0.703	0.481	0.156	0.455
MolMiner[43]	0.899	-	MolNexTR[44]	0.695	0.419	0.045	0.401
			DECIMER[45]	0.545	0.326	0.000	0.298

performance across all metrics, whereas existing PDF parsing frameworks that claim to support chemical structure recognition perform significantly worse on this task.

Table 6: Comparison of PDF parsing systems with OCSR support on a tiny test set, provided purely as a qualitative analysis rather than a quantitative evaluation.

Method	Test Date	Recall \uparrow	OCSR Success \uparrow	OCSR Acc \uparrow	Id Match \uparrow	Time \downarrow
Uni-Parser	2025-08-27	100%	100%	96.5%	100%	1.8 s
MathPix [4]	2025-08-27	100%	75.9%	59.6%	-	66.1 s
MinerU.Chem [46]	2025-09-17	66.7%	63.1%	22.7%	-	\sim 7 min

6 Applications

Uni-Parser opens up a wide range of downstream applications, spanning literature understanding, structured knowledge extraction, patent analysis, and large-scale data generation. Together, these applications demonstrate the framework’s versatility in advancing both scientific research and industrial practice.

Document Understanding. Uni-Parser significantly enhances scientific literature workflows by supporting automatic document summarization, document-level question answering [47], paper-to-poster [48] and paper-to-PPT [49] generation, as well as intelligent retrieval and deep research [50]. Collectively, these capabilities streamline both knowledge consumption and dissemination for researchers across diverse disciplines.

Structured Data Extraction. By converting unstructured documents into structured representations, Uni-Parser supports the large-scale construction of domain-specific databases, such as paper citation database, scholar database, molecular libraries, reaction repositories, bioactivity database [40], experimental characterization database [29, 51, 52], and comprehensive entity knowledge bases. Such resources are critical for accelerating data-driven scientific discovery.

Patent Retrieval and Protection. The framework further facilitates patent retrieval and prior-art verification, providing robust support for innovation discovery and intellectual property protection [53, 54]. This enables more efficient navigation of complex patent landscapes in scientific and industrial settings.

Foundation Model Training. Finally, Uni-Parser can serve as a powerful engine for large-scale training data generation, supplying high-quality structured inputs that reduce the cost and effort of manual curation. This capability is particularly valuable for advancing foundation models in scientific domains, where large, reliable datasets are indispensable [55–57].

7 Failed Approaches

We summarize things that didn’t work during the development of Uni-Parser.

In most scenarios of document intelligence, large-scale pretraining on synthetic data is a simple and effective strategy, because natural documents are largely computer-rendered and therefore exhibit strong domain consistency. However, as discussed in Section 2.2, this intuition breaks down for layout recognition in scientific literature. The layouts of scientific articles are shaped extensively by human editorial practices and creative design choices, making them difficult for heuristic layout engines to reproduce. As a result, synthetic data not only fails to cover the diversity of real-world layouts but can even distort the true data distribution.

For the OCSR task, atom–bond (graph-based) methods are intuitively appealing and have a long history of successful applications; they were also the first direction we explored. While these methods offer clear advantages for handling chirality, they struggle with the wide variety of challenging cases present in real scientific literature. Their strong reliance on rigid, hand-crafted rules fundamentally limits scalability—simply increasing training data provides little benefit. In addition, these methods require substantially more manual annotation effort, typically over 20× that of end-to-end approaches, further constraining their practicality. As a result, compared with end-to-end models, graph-based methods suffer from lower performance ceilings, slower inference, and prohibitively high annotation costs.

8 Future Work

Enhancing Core Components. Uni-Parser’s distributed and modular pipeline architecture allows individual components to be easily upgraded or replaced, facilitating continuous improvement across different document types. We plan to iteratively update the core components to further improve extraction quality across diverse document types:

- **Layout detection:** Our current models are primarily tailored to scientific and patent documents. However, the diversity of document types and layouts is virtually limitless. We will continue to enhance our layout recognition models to support an increasingly broader range of scenarios, including newspapers and magazines, PPT slides, various book formats, and financial statements.
- **OCSR model:** Although our MolParser 1.5 already outperforms previous state-of-the-art methods, the recognition of chiral molecules still presents significant challenges. We will focus on exploring how to address the challenge of chirality recognition within end-to-end OCSR models.
- **Chemical reaction understanding:** Parsing chemical reactions in real-world literature remains highly challenging, with substantial room for improving generalization performance.
- **Chart understanding:** Currently, all existing Chart2Table models and general-purpose MLLMs fall far short of meeting industrial-level requirements for parsing charts in scientific literature, which exhibit a wide variety of types and styles. Chart parsing therefore still holds substantial room for further exploration.
- **Reading order:** We plan to incorporate machine learning–based reading order predictors, to enhance the generalization ability of reading order prediction under complex layouts.
- **Deployment optimization:** Techniques such as quantization (PTQ and QAT), distillation, pruning, and other inference acceleration methods will be explored, along with support for diverse hardware platforms, including Ascend NPUs.

Uni-Parser-Tools for Easy Access. We will release an open-source toolkit, *Uni-Parser-Tools*, providing remote access to Uni-Parser without requiring local compute. The toolkit includes example pipelines for downstream tasks, enabling rapid construction of structured scientific databases and supporting generative AI applications for scientific discovery.

Benchmark Construction. Existing benchmarks (e.g., OmniDocBench and the Uni-Parser benchmark) are limited by inconsistent layout annotations and heterogeneous OCR outputs, and fail to adequately capture complex layouts and cross-page content. We plan to explore more robust, task-driven benchmarks tailored to downstream applications such as document understanding and structured data extraction, enabling fairer and more informative evaluations.

References

- [1] N. Livathinos, C. Auer, M. Lysak, A. Nassar, M. Dolfi, P. Vagenas, C. B. Ramis, M. Omenetti, K. Dinkla, Y. Kim *et al.*, “Docling: An efficient open-source toolkit for ai-driven document conversion,” *arXiv preprint arXiv:2501.17887*, 2025.
- [2] C. Cui, T. Sun, M. Lin, T. Gao, Y. Zhang, J. Liu, X. Wang, Z. Zhang, C. Zhou, H. Liu *et al.*, “Paddleocr 3.0 technical report,” *arXiv preprint arXiv:2507.05595*, 2025.
- [3] B. Wang, C. Xu, X. Zhao, L. Ouyang, F. Wu, Z. Zhao, R. Xu, K. Liu, Y. Qu, F. Shang *et al.*, “Mineru: An open-source solution for precise document content extraction,” *arXiv preprint arXiv:2409.18839*, 2024.
- [4] MathPix Team, “MathPix,” <https://mathpix.com/>, 2025.
- [5] L. Blecher, G. Cucurull, T. Scialom, and R. Stojnic, “Nougat: Neural optical understanding for academic documents,” *arXiv preprint arXiv:2308.13418*, 2023.
- [6] H. Wei, C. Liu, J. Chen, J. Wang, L. Kong, Y. Xu, Z. Ge, L. Zhao, J. Sun, Y. Peng *et al.*, “General ocr theory: Towards ocr-2.0 via a unified end-to-end model,” *arXiv preprint arXiv:2409.01704*, 2024.
- [7] A. Nassar, A. Marafioti, M. Omenetti, M. Lysak, N. Livathinos, C. Auer, L. Morin, R. T. de Lima, Y. Kim, A. S. Gurbuz *et al.*, “Smoldocling: An ultra-compact vision-language model for end-to-end multi-modal document conversion,” *arXiv preprint arXiv:2503.11576*, 2025.
- [8] Z. Li, Y. Liu, Q. Liu, Z. Ma, Z. Zhang, S. Zhang, Z. Guo, J. Zhang, X. Wang, and X. Bai, “Monkeyocr: Document parsing with a structure-recognition-relation triplet paradigm,” *arXiv preprint arXiv:2506.05218*, 2025.
- [9] OCRFlux Team, “OCRFlux: Mastering complex layouts and seamless page merging,” <https://ocrflux.pdfparser.io/>, 2025.
- [10] rednote-hilab, “dots.ocr: Multilingual document layout parsing in a single vision-language model,” <https://huggingface.co/rednote-hilab/dots.ocr>, 2025.
- [11] Mistral Team, “MistralOCR,” <https://mistral.ai/news/>, 2025.
- [12] Z. Zhao, H. Kang, B. Wang, and C. He, “Doclayout-yolo: Enhancing document layout analysis through diverse synthetic data and global-to-local adaptive perception,” *arXiv preprint arXiv:2410.12628*, 2024.
- [13] B. Pfizmann, C. Auer, M. Dolfi, A. S. Nassar, and P. Staar, “Doclaynet: A large human-annotated dataset for document-layout segmentation,” in *Proceedings of the 28th ACM SIGKDD conference on knowledge discovery and data mining*, 2022, pp. 3743–3751.
- [14] Y. Zhao, W. Lv, S. Xu, J. Wei, G. Wang, Q. Dang, Y. Liu, and J. Chen, “Detrs beat yolos on real-time object detection,” in *Proceedings of the IEEE/CVF conference on computer vision and pattern recognition*, 2024, pp. 16965–16974.
- [15] Y. Tian, Q. Ye, and D. Doermann, “Yolov12: Attention-centric real-time object detectors,” *arXiv preprint arXiv:2502.12524*, 2025.
- [16] Y. Peng, H. Li, P. Wu, Y. Zhang, X. Sun, and F. Wu, “D-fine: Redefine regression task in detrs as fine-grained distribution refinement,” *arXiv preprint arXiv:2410.13842*, 2024.
- [17] G. Jocher, J. Qiu, and A. Chaurasia, “Ultralytics yolo,” Ultralytics, 2025. [Online]. Available: <https://ultralytics.com>
- [18] A. Steiner, A. S. Pinto, M. Tschannen, D. Keysers, X. Wang, Y. Bitton, A. Gritsenko, M. Minderer, A. Sherbondy, S. Long *et al.*, “Paligemma 2: A family of versatile vlms for transfer,” *arXiv preprint arXiv:2412.03555*, 2024.
- [19] C. Cui, T. Sun, S. Liang, T. Gao, Z. Zhang, J. Liu, X. Wang, C. Zhou, H. Liu, M. Lin, Y. Zhang, Y. Zhang, H. Zheng, J. Zhang, J. Zhang, Y. Liu, D. Yu, and Y. Ma, “Paddleocr-vl: Boosting multilingual document parsing via a 0.9b ultra-compact vision-language model,” 2025. [Online]. Available: <https://arxiv.org/abs/2510.14528>
- [20] C. Li, R. Guo, J. Zhou, M. An, Y. Du, L. Zhu, Y. Liu, X. Hu, and D. Yu, “Pp-structurev2: A stronger document analysis system,” *arXiv preprint arXiv:2210.05391*, 2022.
- [21] X. Zhong, E. ShafieiBavani, and A. J. Yepes, “Image-based table recognition: data, model, and evaluation,” *arXiv preprint arXiv:1911.10683*, 2019.

- [22] A. Nassar, N. Livathinos, M. Lysak, and P. Staar, “Tableformer: Table structure understanding with transformers,” *arXiv preprint arXiv:2203.01017*, 2022.
- [23] X. Fang, J. Wang, X. Cai, S. Chen, S. Yang, H. Tao, N. Wang, L. Yao, L. Zhang, and G. Ke, “Molparser: End-to-end visual recognition of molecule structures in the wild,” *arXiv preprint arXiv:2411.11098*, 2024.
- [24] Y. Qian, J. Guo, Z. Tu, Z. Li, C. W. Coley, and R. Barzilay, “Molscribe: robust molecular structure recognition with image-to-graph generation,” *Journal of Chemical Information and Modeling*, vol. 63, no. 7, pp. 1925–1934, 2023.
- [25] S. Bai, K. Chen, X. Liu, J. Wang, W. Ge, S. Song, K. Dang, P. Wang, S. Wang, J. Tang *et al.*, “Qwen2. 5-vl technical report,” *arXiv preprint arXiv:2502.13923*, 2025.
- [26] OpenAI, “Introducing gpt-5,” 2025. [Online]. Available: <https://openai.com/index/introducing-gpt-5/>
- [27] DeepMind, “Gemini 2.5 pro,” 2025. [Online]. Available: <https://deepmind.google/models/gemini/pro/>
- [28] A. Mirza, N. Alampara, M. Ríos-García, M. Abdelalim, J. Butler, B. Connolly, T. Dogan, M. Nezhurina, B. Şen, S. Tirunagari *et al.*, “Chempile: A 250gb diverse and curated dataset for chemical foundation models,” *arXiv preprint arXiv:2505.12534*, 2025.
- [29] Z. Xia, Y. Li, S. Tang, Z. Fan, X. Fang, H. Tao, X. Cai, G. Ke, L. Zhang, Y. Hong *et al.*, “Uniem-3m: A universal electron micrograph dataset for microstructural segmentation and generation,” *arXiv preprint arXiv:2508.16239*, 2025.
- [30] H. Kydlíček, G. Penedo, and L. von Werra, “Finepdfs,” <https://huggingface.co/datasets/HuggingFaceFW/finepdfs>, 2025.
- [31] L. Ouyang, Y. Qu, H. Zhou, J. Zhu, R. Zhang, Q. Lin, B. Wang, Z. Zhao, M. Jiang, X. Zhao *et al.*, “Omidocbench: Benchmarking diverse pdf document parsing with comprehensive annotations,” in *Proceedings of the Computer Vision and Pattern Recognition Conference*, 2025, pp. 24 838–24 848.
- [32] H. Wei, Y. Sun, and Y. Li, “Deepseek-ocr: Contexts optical compression,” *arXiv preprint arXiv:2510.18234*, 2025.
- [33] V. Varma, “Marker: Convert pdf to markdown and json quickly with high accuracy,” <https://github.com/datalab-to/marker>, 2023.
- [34] J. Zhu, W. Wang, Z. Chen, Z. Liu, S. Ye, L. Gu, H. Tian, Y. Duan, W. Su, J. Shao *et al.*, “Internvl3: Exploring advanced training and test-time recipes for open-source multimodal models,” *arXiv preprint arXiv:2504.10479*, 2025.
- [35] H. Feng, S. Wei, X. Fei, W. Shi, Y. Han, L. Liao, J. Lu, B. Wu, Q. Liu, C. Lin *et al.*, “Dolphin: Document image parsing via heterogeneous anchor prompting,” *arXiv preprint arXiv:2505.14059*, 2025.
- [36] ChatDOC, “Ocrflux-3b: A high-accuracy multimodal ocr model for document parsing,” <https://huggingface.co/ChatDOC/OCRFlux-3B>, 2024.
- [37] Y. Liu, Z. Zhao, L. Tian, H. Wang, X. Ye, Y. You, Z. Yu, C. Wu, X. Zhou, Y. Yu, and J. Zhou, “Points-reader: Distillation-free adaptation of vision-language models for document conversion,” *arXiv preprint arXiv:2509.01215*, 2025.
- [38] J. Poznanski, A. Rangapur, J. Borchardt, J. Dunkelberger, R. Huff, D. Lin, C. Wilhelm, K. Lo, and L. Soldaini, “olmocr: Unlocking trillions of tokens in pdfs with vision language models,” *arXiv preprint arXiv:2502.18443*, 2025.
- [39] S. Mandal, A. Talewar, P. Ahuja, and P. Juvatkar, “Nanonets-ocr-s: A model for transforming documents into structured markdown with intelligent content recognition and semantic tagging,” 2025.
- [40] J. Yan, J. Zhu, Y. Yang, Q. Liu, K. Zhang, Z. Zhang, X. Liu, B. Zhang, K. Gao, J. Xiao *et al.*, “Biominer: A multi-modal system for automated mining of protein-ligand bioactivity data from literature,” *bioRxiv*, 2025.
- [41] XtalPi, “Molvision,” 2025. [Online]. Available: <https://www.xinsight-ai.com/mol-recognition?mol-recognition=%2Fmol-recognition>
- [42] J. Xiong, X. Liu, Z. Li, H. Xiao, G. Wang, Z. Niu, C. Fei, F. Zhong, G. Wang, W. Zhang *et al.*, “ α extractor: a system for automatic extraction of chemical information from biomedical literature,” *Sci. China: Life Sci.*, vol. 67, pp. 618–621, 2023.

- [43] Y. Xu, J. Xiao, C.-H. Chou, J. Zhang, J. Zhu, Q. Hu, H. Li, N. Han, B. Liu, S. Zhang, J. Han, Z. Zhang, S. Zhang, W. Zhang, L. Lai, and J. Pei, "Molminer: You only look once for chemical structure recognition," *Journal of Chemical Information and Modeling*, vol. 62, no. 22, pp. 5321–5328, 2022.
- [44] Y. Chen, C. T. Leung, Y. Huang, J. Sun, H. Chen, and H. Gao, "Molnextr: A generalized deep learning model for molecular image recognition," *arXiv preprint arXiv:2403.03691*, 2024.
- [45] K. Rajan, H. O. Brinkhaus, M. I. Agea, A. Zielesny, and C. Steinbeck, "Decimer. ai: an open platform for automated optical chemical structure identification, segmentation and recognition in scientific publications," *Nature communications*, vol. 14, no. 1, p. 5045, 2023.
- [46] MinerU Team, "Mineru.chem," 2025. [Online]. Available: <https://mineru.net/chem/>
- [47] H. Cai, X. Cai, S. Yang, J. Wang, L. Yao, Z. Gao, J. Chang, S. Li, M. Xu, C. Wang *et al.*, "Uni-smart: universal science multimodal analysis and research transformer," *arXiv preprint arXiv:2403.10301*, 2024.
- [48] W. Pang, K. Q. Lin, X. Jian, X. He, and P. Torr, "Paper2poster: Towards multimodal poster automation from scientific papers," *arXiv preprint arXiv:2505.21497*, 2025.
- [49] D.-A. D. Team, "Dataflow-agent: Ai-powered data & paper workflow orchestration platform," <https://github.com/OpenDCAI/DataFlow-Agent>, 2025.
- [50] OpenAI, "Deep research," <https://openai.com/deep-research>, 2025, [AI research tool].
- [51] F. Xu, W. Guo, F. Wang, L. Yao, H. Wang, F. Tang, Z. Gao, L. Zhang, W. E, Z.-Q. Tian *et al.*, "Toward a unified benchmark and framework for deep learning-based prediction of nuclear magnetic resonance chemical shifts," *Nature Computational Science*, pp. 1–9, 2025.
- [52] J.-J. Wang, Y. Jin, C.-Y. Zhi, Y.-J. Liu, X.-H. Huang, F. Xu, X. Ji, X. Fang, H. Tao, W. E *et al.*, "Nmrex: A database of 3.3 million experimental nmr spectra," *Scientific Data*, vol. 12, no. 1, p. 1954, 2025.
- [53] Y. Shi, S. Li, T. Zhang, X. Fang, J. Wang, Z. Liu, G. Zhao, Z. Zhu, Z. Gao, R. Zhong *et al.*, "Intelligent system for automated molecular patent infringement assessment," *arXiv preprint arXiv:2412.07819*, 2024.
- [54] J. Zhuang, K. Li, J. Hou, M. Xu, Z. Gao, and H. Cai, "Doc2sar: A synergistic framework for high-fidelity extraction of structure-activity relationships from scientific documents," *arXiv preprint arXiv:2506.21625*, 2025.
- [55] S. Li, J. Huang, J. Zhuang, Y. Shi, X. Cai, M. Xu, X. Wang, L. Zhang, G. Ke, and H. Cai, "Scilitlm: How to adapt llms for scientific literature understanding," *arXiv preprint arXiv:2408.15545*, 2024.
- [56] N. Liao, X. Wang, Z. Lin, W. Guo, F. Hong, S. Song, G. Yu, Z. Zhao, S. Xie, L. Wei *et al.*, "Innovator: Scientific continued pretraining with fine-grained moe upcycling," *arXiv preprint arXiv:2507.18671*, 2025.
- [57] D. D. Team, "Dataflow: A unified framework for data-centric ai," <https://github.com/OpenDCAI/DataFlow>, 2025, accessed: 2025-07-08.

A Authorship and Acknowledgments

Please cite this work as “DP Technology (2025)”.

Correspondence regarding this technical report can be sent to fangxi@dp.tech

Principal Contributor

Haoyi Tao

Project Lead

Xi Fang

Core Contributors*

Chaozheng Huang

Han Lyu

Haocheng Lu

Junjie Wang

Shuwen Yang

Suyang Zhong

Xi Fang

Team Management

Guolin Ke

Linfeng Zhang

Xinyu Li

Contributors & Acknowledgments*

Changhong Chen

Chenkai Wu

Fanjie Xu

Hanzheng Li

Hengxin Cai

Jialu Shen

Jian Zhou

Jiankun Wang

Jiaxi Zhuang

Jinbo Hu

Jindi Guo

Jingwen Deng

Lin Yao

Mingjun Xu

Nan Wang

Ning Wang

Qingguo Zhou

Qiushi Huang

Shang Xiang

Shangqian Chen

Shaojie Chen

Shengyu Li

Xiaochen Cai

Xiaohong Ji

Xinyu Xiong

Xuan Xie

Yanhui Hong

Yaorui Shi

Yaqi Li

Yixuan Li

Yuan Gao

Zhenhao Wong

Zhifeng Gao

Zhiyuan Chang

Zhiyue Wang

*Contributors listed in alphabetized order.

B Examples and Comparisons

B.1 MolParser-1.5 Case Study

Raw Image	Simple				
	MinerU.Chem	MolScribe	MolVision	AlphaExtractor	MolParser 1.5
	Atom-Bond Based Algorithm				End-to-End Algorithm
Raw Image	Chirality				
	MinerU.Chem	MolScribe	MolVision	AlphaExtractor	MolParser 1.5
	Atom-Bond Based Algorithm				End-to-End Algorithm
				Error	
Raw Image	Abbreviation				
	MinerU.Chem	MolScribe	MolVision	AlphaExtractor	MolParser 1.5
	Atom-Bond Based Algorithm				End-to-End Algorithm
Raw Image	Colored				
	MinerU.Chem	MolScribe	MolVision	AlphaExtractor	MolParser 1.5
	Atom-Bond Based Algorithm				End-to-End Algorithm
		Error			
	Error				

*The evaluation was conducted on August 27, 2025.

Markush					
Raw Image	MinerU.Chem	MolScribe	MolVision	AlphaExtractor	MolParser 1.5
Atom-Bond Based Algorithm			End-to-End Algorithm		

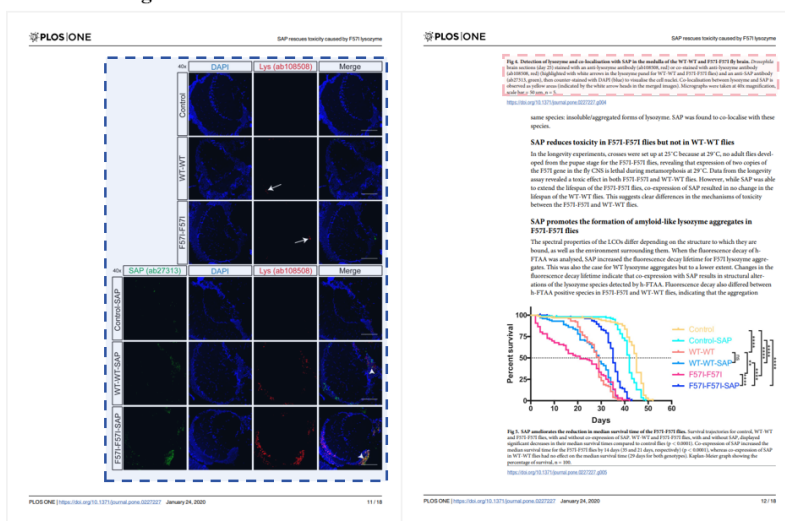
Connection Point					
Raw Image	MinerU.Chem	MolScribe	MolVision	AlphaExtractor	MolParser 1.5
Atom-Bond Based Algorithm			End-to-End Algorithm		

Charged					
Raw Image	MinerU.Chem	MolScribe	MolVision	AlphaExtractor	MolParser 1.5
Atom-Bond Based Algorithm			End-to-End Algorithm		

Raw Image	Noise				
	MinerU.Chem	MolScribe	MolVision	AlphaExtractor	MolParser 1.5
	Error				
	Error				
	Error				

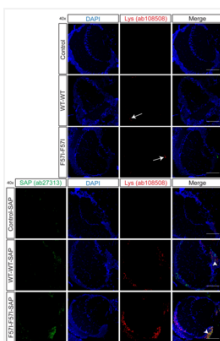
B.2 Qualitative Examples of Cross-Page Layout Grouping

Raw PDF Pages:



Cross-Pages Groups:

Image:



Caption:

Fig 4. Detection of lysozyme and co-localisation with SAP in the medulla of the WT-WT and F571-F571 fly brain. *Drosophila* brain sections (day 25) stained with an anti-lysozyme antibody (ab108508, red) or co-stained with anti-lysozyme antibody (ab108508, red) (highlighted with white arrows in the lysozyme panel for WT-WT and F571-F571 flies) and an anti-SAP antibody (ab27313, green), then counter-stained with DAPI (blue) to visualise the cell nuclei. Co-localisation between lysozyme and SAP is observed as yellow areas (indicated by the white arrow heads in the merged images). Micrographs were taken at 40x magnification, scale bar = 50 μ m, n = 5.

B.3 Layout Detection Comparison

Original Document

Uni-Parser

OPEN ACCESS
CellPress

Figure 2. mdt Promotes AJ Morphogenesis Independently from Baz.
A-C) *mdt*¹⁴⁶ mutant, lacking GFP (blue), Am (red), Baz (green), Cb, and merge (S). The scale bar represents 2 μm.
D) Mean length of Am cortical domain in wild-type and *mdt*¹⁴⁶ mutants.
E) Mean basal intensity of Am in wild-type and *mdt*¹⁴⁶ in 80 and 60 s. n = 200 in four wild-type retinae and n = 400 in four *mdt*¹⁴⁶ retinae.
F) Mean length of Baz cortical domain in wild-type and *mdt*¹⁴⁶ mutants.
G) Mean basal intensity of Baz in wild-type and *mdt*¹⁴⁶ in both 80 and 60 s. n = 90 (wild-type) and n = 100 (*mdt*¹⁴⁶), with measurements taken from the independent *mdt*¹⁴⁶ mosaic retina. In 80-s columns represent mean and error bars represent the SEM of each domain. Statistical significance was determined using an unpaired two-tailed Student's t test.
H and I) Electron microscopy (E) on a wild-type ommatidium and (I) on the poorly developed apical membranes of an *mdt*¹⁴⁶ adult ommatidium. Ectopic AJ domains are boxed and sub-apical membranes in green. The scale bar represents 2 μm.
J-K) *mdt*¹⁴⁶ *mdt*¹⁴⁶ mutant lacking GFP (blue), Am (green), L1, aPKC (red), Mb, and merge (N). Asterisks highlight mutant cells. A blue mark is a wild-type cell. The scale bar represents 4 μm.
L) FRAP on E-cadherin-GFP in wild-type or *mdt*¹⁴⁶. Mean normalized fluorescence intensity in wild-type (n = 18 from two individuals) and *mdt*¹⁴⁶ (n = 15 from three individuals) is shown; error bars represent SEM. Fluorescence recovery curves of E-cadherin-GFP after photo-bleaching in wild-type (black) and *mdt*¹⁴⁶ (red) are shown.
M) Mobile fraction of E-cadherin-GFP in a wild-type (black) or *mdt*¹⁴⁶ (red) background. The value was calculated with an unpaired two-tailed Student's t test with Welch's correction.

morphogenesis, we measure a significant decrease in the length and mean basal intensity of Am and Baz at the developing ZA of *mdt*¹⁴⁶ mutant photoreceptors (Figures 2A-2F). In addition, *mdt* is required for overall apical membrane differentiation, albeit only in a fraction of the mutant cells (Figures 2J and 2L). We found that, in 40% of the *mdt*¹⁴⁶ mutant ommatidia (n = 2,662 from nine retinae), no ZA assemblies along the photoreceptors proximal axis, and instead, poorly differentiated apical membranes are found between the floor of the retina and the lamina part of the brain (Figures 2J and 2L). Whereas these membranes contain aPKC, Cb, Baz, and Am, apico-basal polarity is severely compromised (Figures 2J-2D). These data indicate that Mdt promotes AJ morphogenesis and to some extent apical membrane morphogenesis. Importantly, the *mdt* phenotype can be fully rescued when expressing a wild-type version of this kinase (Figure 2M). In contrast, re-introducing a version of Mdt that can no longer bind to Cdc42 or lacks kinase activity (Schmueder and Rastbe, 2003) fails to rescue the *mdt* phenotype (Figure 2M). Therefore, Mdt functions through its kinase activity, which, as expected for this family of kinases, is regulated via binding to Cdc42 (Hir et al., 2015).

Mdt Does Not Phosphorylate Par6 in Drosophila
In order to gain mechanistic insight into how Mdt might regulate apical membrane morphogenesis, we examined the relationship

between Mdt and Par6. Human Pak4 (HPak4) can phosphorylate Par6 at serine 143, which is found in Drosophila Par6 at position 146 (Lin et al., 2016). However, the 1-2 residue in Par6 that is required for overall apical membrane differentiation, albeit only in a fraction of the mutant cells (Figures 2J and 2L). We found that, in 40% of the *mdt*¹⁴⁶ mutant ommatidia (n = 2,662 from nine retinae), no ZA assemblies along the photoreceptors proximal axis, and instead, poorly differentiated apical membranes are found between the floor of the retina and the lamina part of the brain (Figures 2J and 2L). Whereas these membranes contain aPKC, Cb, Baz, and Am, apico-basal polarity is severely compromised (Figures 2J-2D). These data indicate that Mdt promotes AJ morphogenesis and to some extent apical membrane morphogenesis. Importantly, the *mdt* phenotype can be fully rescued when expressing a wild-type version of this kinase (Figure 2M). In contrast, re-introducing a version of Mdt that can no longer bind to Cdc42 or lacks kinase activity (Schmueder and Rastbe, 2003) fails to rescue the *mdt* phenotype (Figure 2M). Therefore, Mdt functions through its kinase activity, which, as expected for this family of kinases, is regulated via binding to Cdc42 (Hir et al., 2015).

Mdt Regulates the Stability of E-cadherin at the ZA
Mdt influences the stability of the E-cadherin-catenin complex in non-polarized S2 cells (Merrill et al., 2009). To examine whether this contributes to regulating AJ morphogenesis, we made use of fluorescence recovery after photobleaching (FRAP) to evaluate the mobile fraction and half-time recovery of E-cadherin. When photo-bleaching the base of the wild-type ZA, we find that 33.3% ± 0.6% of E-cadherin-GFP is mobile with an evaluated

Cell Reports 15, 45-53, April 5, 2016 47

OPEN ACCESS
CellPress

Figure 2. mdt Promotes AJ Morphogenesis Independently from Baz.
A-C) *mdt*¹⁴⁶ mutant, lacking GFP (blue), Am (red), Baz (green), Cb, and merge (S). The scale bar represents 2 μm.
D) Mean length of Am cortical domain in wild-type and *mdt*¹⁴⁶ mutants.
E) Mean basal intensity of Am in wild-type and *mdt*¹⁴⁶ in 80 and 60 s. n = 200 in four wild-type retinae and n = 400 in four *mdt*¹⁴⁶ retinae.
F) Mean length of Baz cortical domain in wild-type and *mdt*¹⁴⁶ mutants.
G) Mean basal intensity of Baz in wild-type and *mdt*¹⁴⁶ in both 80 and 60 s. n = 90 (wild-type) and n = 100 (*mdt*¹⁴⁶), with measurements taken from the independent *mdt*¹⁴⁶ mosaic retina. In 80-s columns represent mean and error bars represent the SEM of each domain. Statistical significance was determined using an unpaired two-tailed Student's t test.
H and I) Electron microscopy (E) on a wild-type ommatidium and (I) on the poorly developed apical membranes of an *mdt*¹⁴⁶ adult ommatidium. Ectopic AJ domains are boxed and sub-apical membranes in green. The scale bar represents 2 μm.
J-K) *mdt*¹⁴⁶ *mdt*¹⁴⁶ mutant lacking GFP (blue), Am (green), L1, aPKC (red), Mb, and merge (N). Asterisks highlight mutant cells. A blue mark is a wild-type cell. The scale bar represents 4 μm.
L) FRAP on E-cadherin-GFP in wild-type or *mdt*¹⁴⁶. Mean normalized fluorescence intensity in wild-type (n = 18 from two individuals) and *mdt*¹⁴⁶ (n = 15 from three individuals) is shown; error bars represent SEM. Fluorescence recovery curves of E-cadherin-GFP after photo-bleaching in wild-type (black) and *mdt*¹⁴⁶ (red) are shown.
M) Mobile fraction of E-cadherin-GFP in a wild-type (black) or *mdt*¹⁴⁶ (red) background. The value was calculated with an unpaired two-tailed Student's t test with Welch's correction.

morphogenesis, we measure a significant decrease in the length and mean basal intensity of Am and Baz at the developing ZA of *mdt*¹⁴⁶ mutant photoreceptors (Figures 2A-2F). In addition, *mdt* is required for overall apical membrane differentiation, albeit only in a fraction of the mutant cells (Figures 2J and 2L). We found that, in 40% of the *mdt*¹⁴⁶ mutant ommatidia (n = 2,662 from nine retinae), no ZA assemblies along the photoreceptors proximal axis, and instead, poorly differentiated apical membranes are found between the floor of the retina and the lamina part of the brain (Figures 2J and 2L). Whereas these membranes contain aPKC, Cb, Baz, and Am, apico-basal polarity is severely compromised (Figures 2J-2D). These data indicate that Mdt promotes AJ morphogenesis and to some extent apical membrane morphogenesis. Importantly, the *mdt* phenotype can be fully rescued when expressing a wild-type version of this kinase (Figure 2M). In contrast, re-introducing a version of Mdt that can no longer bind to Cdc42 or lacks kinase activity (Schmueder and Rastbe, 2003) fails to rescue the *mdt* phenotype (Figure 2M). Therefore, Mdt functions through its kinase activity, which, as expected for this family of kinases, is regulated via binding to Cdc42 (Hir et al., 2015).

Mdt Regulates the Stability of E-cadherin at the ZA
Mdt influences the stability of the E-cadherin-catenin complex in non-polarized S2 cells (Merrill et al., 2009). To examine whether this contributes to regulating AJ morphogenesis, we made use of fluorescence recovery after photobleaching (FRAP) to evaluate the mobile fraction and half-time recovery of E-cadherin. When photo-bleaching the base of the wild-type ZA, we find that 33.3% ± 0.6% of E-cadherin-GFP is mobile with an evaluated

Cell Reports 15, 45-53, April 5, 2016 47

PP-Structure V3

MinerU2.5

OPEN ACCESS
CellPress

Figure 2. mdt Promotes AJ Morphogenesis Independently from Baz.
A-C) *mdt*¹⁴⁶ mutant, lacking GFP (blue), Am (red), Baz (green), Cb, and merge (S). The scale bar represents 2 μm.
D) Mean length of Am cortical domain in wild-type and *mdt*¹⁴⁶ mutants.
E) Mean basal intensity of Am in wild-type and *mdt*¹⁴⁶ in 80 and 60 s. n = 200 in four wild-type retinae and n = 400 in four *mdt*¹⁴⁶ retinae.
F) Mean length of Baz cortical domain in wild-type and *mdt*¹⁴⁶ mutants.
G) Mean basal intensity of Baz in wild-type and *mdt*¹⁴⁶ in both 80 and 60 s. n = 90 (wild-type) and n = 100 (*mdt*¹⁴⁶), with measurements taken from the independent *mdt*¹⁴⁶ mosaic retina. In 80-s columns represent mean and error bars represent the SEM of each domain. Statistical significance was determined using an unpaired two-tailed Student's t test.
H and I) Electron microscopy (E) on a wild-type ommatidium and (I) on the poorly developed apical membranes of an *mdt*¹⁴⁶ adult ommatidium. Ectopic AJ domains are boxed and sub-apical membranes in green. The scale bar represents 2 μm.
J-K) *mdt*¹⁴⁶ *mdt*¹⁴⁶ mutant lacking GFP (blue), Am (green), L1, aPKC (red), Mb, and merge (N). Asterisks highlight mutant cells. A blue mark is a wild-type cell. The scale bar represents 4 μm.
L) FRAP on E-cadherin-GFP in wild-type or *mdt*¹⁴⁶. Mean normalized fluorescence intensity in wild-type (n = 18 from two individuals) and *mdt*¹⁴⁶ (n = 15 from three individuals) is shown; error bars represent SEM. Fluorescence recovery curves of E-cadherin-GFP after photo-bleaching in wild-type (black) and *mdt*¹⁴⁶ (red) are shown.
M) Mobile fraction of E-cadherin-GFP in a wild-type (black) or *mdt*¹⁴⁶ (red) background. The value was calculated with an unpaired two-tailed Student's t test with Welch's correction.

morphogenesis, we measure a significant decrease in the length and mean basal intensity of Am and Baz at the developing ZA of *mdt*¹⁴⁶ mutant photoreceptors (Figures 2A-2F). In addition, *mdt* is required for overall apical membrane differentiation, albeit only in a fraction of the mutant cells (Figures 2J and 2L). We found that, in 40% of the *mdt*¹⁴⁶ mutant ommatidia (n = 2,662 from nine retinae), no ZA assemblies along the photoreceptors proximal axis, and instead, poorly differentiated apical membranes are found between the floor of the retina and the lamina part of the brain (Figures 2J and 2L). Whereas these membranes contain aPKC, Cb, Baz, and Am, apico-basal polarity is severely compromised (Figures 2J-2D). These data indicate that Mdt promotes AJ morphogenesis and to some extent apical membrane morphogenesis. Importantly, the *mdt* phenotype can be fully rescued when expressing a wild-type version of this kinase (Figure 2M). In contrast, re-introducing a version of Mdt that can no longer bind to Cdc42 or lacks kinase activity (Schmueder and Rastbe, 2003) fails to rescue the *mdt* phenotype (Figure 2M). Therefore, Mdt functions through its kinase activity, which, as expected for this family of kinases, is regulated via binding to Cdc42 (Hir et al., 2015).

Mdt Regulates the Stability of E-cadherin at the ZA
Mdt influences the stability of the E-cadherin-catenin complex in non-polarized S2 cells (Merrill et al., 2009). To examine whether this contributes to regulating AJ morphogenesis, we made use of fluorescence recovery after photobleaching (FRAP) to evaluate the mobile fraction and half-time recovery of E-cadherin. When photo-bleaching the base of the wild-type ZA, we find that 33.3% ± 0.6% of E-cadherin-GFP is mobile with an evaluated

Cell Reports 15, 45-53, April 5, 2016 47

OPEN ACCESS
CellPress

Figure 2. mdt Promotes AJ Morphogenesis Independently from Baz.
A-C) *mdt*¹⁴⁶ mutant, lacking GFP (blue), Am (red), Baz (green), Cb, and merge (S). The scale bar represents 2 μm.
D) Mean length of Am cortical domain in wild-type and *mdt*¹⁴⁶ mutants.
E) Mean basal intensity of Am in wild-type and *mdt*¹⁴⁶ in 80 and 60 s. n = 200 in four wild-type retinae and n = 400 in four *mdt*¹⁴⁶ retinae.
F) Mean length of Baz cortical domain in wild-type and *mdt*¹⁴⁶ mutants.
G) Mean basal intensity of Baz in wild-type and *mdt*¹⁴⁶ in both 80 and 60 s. n = 90 (wild-type) and n = 100 (*mdt*¹⁴⁶), with measurements taken from the independent *mdt*¹⁴⁶ mosaic retina. In 80-s columns represent mean and error bars represent the SEM of each domain. Statistical significance was determined using an unpaired two-tailed Student's t test.
H and I) Electron microscopy (E) on a wild-type ommatidium and (I) on the poorly developed apical membranes of an *mdt*¹⁴⁶ adult ommatidium. Ectopic AJ domains are boxed and sub-apical membranes in green. The scale bar represents 2 μm.
J-K) *mdt*¹⁴⁶ *mdt*¹⁴⁶ mutant lacking GFP (blue), Am (green), L1, aPKC (red), Mb, and merge (N). Asterisks highlight mutant cells. A blue mark is a wild-type cell. The scale bar represents 4 μm.
L) FRAP on E-cadherin-GFP in wild-type or *mdt*¹⁴⁶. Mean normalized fluorescence intensity in wild-type (n = 18 from two individuals) and *mdt*¹⁴⁶ (n = 15 from three individuals) is shown; error bars represent SEM. Fluorescence recovery curves of E-cadherin-GFP after photo-bleaching in wild-type (black) and *mdt*¹⁴⁶ (red) are shown.
M) Mobile fraction of E-cadherin-GFP in a wild-type (black) or *mdt*¹⁴⁶ (red) background. The value was calculated with an unpaired two-tailed Student's t test with Welch's correction.

morphogenesis, we measure a significant decrease in the length and mean basal intensity of Am and Baz at the developing ZA of *mdt*¹⁴⁶ mutant photoreceptors (Figures 2A-2F). In addition, *mdt* is required for overall apical membrane differentiation, albeit only in a fraction of the mutant cells (Figures 2J and 2L). We found that, in 40% of the *mdt*¹⁴⁶ mutant ommatidia (n = 2,662 from nine retinae), no ZA assemblies along the photoreceptors proximal axis, and instead, poorly differentiated apical membranes are found between the floor of the retina and the lamina part of the brain (Figures 2J and 2L). Whereas these membranes contain aPKC, Cb, Baz, and Am, apico-basal polarity is severely compromised (Figures 2J-2D). These data indicate that Mdt promotes AJ morphogenesis and to some extent apical membrane morphogenesis. Importantly, the *mdt* phenotype can be fully rescued when expressing a wild-type version of this kinase (Figure 2M). In contrast, re-introducing a version of Mdt that can no longer bind to Cdc42 or lacks kinase activity (Schmueder and Rastbe, 2003) fails to rescue the *mdt* phenotype (Figure 2M). Therefore, Mdt functions through its kinase activity, which, as expected for this family of kinases, is regulated via binding to Cdc42 (Hir et al., 2015).

Mdt Regulates the Stability of E-cadherin at the ZA
Mdt influences the stability of the E-cadherin-catenin complex in non-polarized S2 cells (Merrill et al., 2009). To examine whether this contributes to regulating AJ morphogenesis, we made use of fluorescence recovery after photobleaching (FRAP) to evaluate the mobile fraction and half-time recovery of E-cadherin. When photo-bleaching the base of the wild-type ZA, we find that 33.3% ± 0.6% of E-cadherin-GFP is mobile with an evaluated

Cell Reports 15, 45-53, April 5, 2016 47

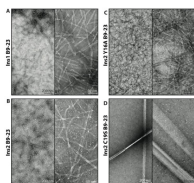


Figure 1. TEM images of the four B9-23 peptides in water obtained after one-week incubation at 37°C. (A) Ins1 B9-23, (B) Ins2 B9-23, (C) Ins3 B9-23 T16A, and (D) Ins2 B9-23 C19S. The peptide concentration is 100 μM.

All four insulin B9-23 peptides were analyzed immediately after mixing and after two days of aggregation in both positive and negative modes for the IMS-MS experiments. Since all four peptides are

negatively charged at physiological pH, the subsequent discussion in this work will be on the data acquired from the negative IMS polarity, but we will use the positive polarity data set as complementary. Figure 2A-B show the mass spectra of Ins1 B9-23 and Ins2 B9-23 in negative mode, each containing several mass spectral peaks corresponding to multiple charge states and oligomeric sizes under the same experimental conditions. The peaks are annotated by nominal m/z , where n is the oligomer size and z is the charge. The insets of the two mass spectra for the two peptides show that oligomers have up to a heptamer ($n = 7$) for Ins1 B9-23 and dodecamer ($n = 12$) for Ins2 B9-23. More oligomers can be observed in the higher mass region of the mass spectra for Ins2 B9-23 compared to Ins1 B9-23. The most dominant peak in the mass spectra is the $n/z = 1/2$, which contains mostly monomers. The experimental CCS for the $n/z = 1/2$ species is presented in Table S3 (along the CCS values for the same species of the other B9-23 peptides). The highlighted peak in the nominal $n/z = 1/1$ species, of which the 2D plots of diff time vs. m/z are shown in Figure 2C-D, respectively. This n/z peak, although less intense than $n/z = 1/2$, contains an abundance of isotopic oligomeric species. It is also the highest intensity peak of the oligomers. The 2D plot of m/z vs. diff time shows the separations of ions based on their m/z values and their arrival times. Therefore, various oligomers with the same m/z but different charge states can have distinct clusters in the 2D plot.

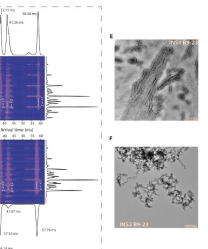


Figure 2. Representative mass spectra of (A) Ins1 B9-23 and (B) Ins2 B9-23. The insets in each region show zoomed-in regions where multiple oligomers are observed. The 2D plots for $n/z = 1/1$ are shown for both (C) Ins1 B9-23 and (D) Ins2 B9-23. TEM images of the peptides in 20 mM ammonium acetate are shown in (E) Ins1 B9-23 and (F) Ins2 B9-23. Filaments are observed in the image of Ins1 B9-23, whereas amorphous aggregates are observed in the image of Ins2 B9-23. The scale bar for the TEM images is 500 nm.

https://doi.org/10.26434/chemrxiv-2024-10-08-0000; https://arxiv.org/abs/2024.10-08-0000 Content not peer-reviewed by ChemRxiv. License: CC BY-NC-ND 4.0

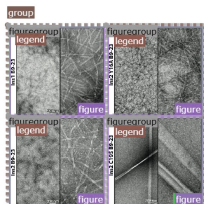


Figure 1. TEM images of the four B9-23 peptides in water obtained after one-week incubation at 37°C. (A) Ins1 B9-23, (B) Ins2 B9-23, (C) Ins3 B9-23 T16A, and (D) Ins2 B9-23 C19S. The peptide concentration is 100 μM.

All four insulin B9-23 peptides were analyzed immediately after mixing and after two days of aggregation in both positive and negative modes for the IMS-MS experiments. Since all four peptides are

negatively charged at physiological pH, the subsequent discussion in this work will be on the data acquired from the negative IMS polarity, but we will use the positive polarity data set as complementary. Figure 2A-B show the mass spectra of Ins1 B9-23 and Ins2 B9-23 in negative mode, each containing several mass spectral peaks corresponding to multiple charge states and oligomeric sizes under the same experimental conditions. The peaks are annotated by nominal m/z , where n is the oligomer size and z is the charge. The insets of the two mass spectra for the two peptides show that oligomers have up to a heptamer ($n = 7$) for Ins1 B9-23 and dodecamer ($n = 12$) for Ins2 B9-23. More oligomers can be observed in the higher mass region of the mass spectra for Ins2 B9-23 compared to Ins1 B9-23. The most dominant peak in the mass spectra is the $n/z = 1/2$, which contains mostly monomers. The experimental CCS for the $n/z = 1/2$ species is presented in Table S3 (along the CCS values for the same species of the other B9-23 peptides). The highlighted peak in the nominal $n/z = 1/1$ species, of which the 2D plots of diff time vs. m/z are shown in Figure 2C-D, respectively. This n/z peak, although less intense than $n/z = 1/2$, contains an abundance of isotopic oligomeric species. It is also the highest intensity peak of the oligomers. The 2D plot of m/z vs. diff time shows the separations of ions based on their m/z values and their arrival times. Therefore, various oligomers with the same m/z but different charge states can have distinct clusters in the 2D plot.

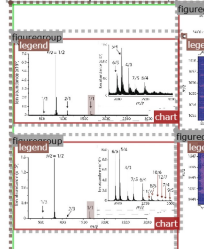


Figure 2. Representative mass spectra of (A) Ins1 B9-23 and (B) Ins2 B9-23. The insets in each region show zoomed-in regions where multiple oligomers are observed. The 2D plots for $n/z = 1/1$ are shown for both (C) Ins1 B9-23 and (D) Ins2 B9-23. TEM images of the peptides in 20 mM ammonium acetate are shown in (E) Ins1 B9-23 and (F) Ins2 B9-23. Filaments are observed in the image of Ins1 B9-23, whereas amorphous aggregates are observed in the image of Ins2 B9-23. The scale bar for the TEM images is 500 nm.

https://doi.org/10.26434/chemrxiv-2024-10-08-0000; https://arxiv.org/abs/2024.10-08-0000 Content not peer-reviewed by ChemRxiv. License: CC BY-NC-ND 4.0

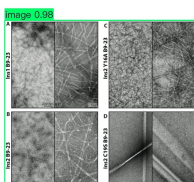


Figure 1. TEM images of the four B9-23 peptides in water obtained after one-week incubation at 37°C. (A) Ins1 B9-23, (B) Ins2 B9-23, (C) Ins3 B9-23 T16A, and (D) Ins2 B9-23 C19S. The peptide concentration is 100 μM.

All four insulin B9-23 peptides were analyzed immediately after mixing and after two days of aggregation in both positive and negative modes for the IMS-MS experiments. Since all four peptides are

negatively charged at physiological pH, the subsequent discussion in this work will be on the data acquired from the negative IMS polarity, but we will use the positive polarity data set as complementary. Figure 2A-B show the mass spectra of Ins1 B9-23 and Ins2 B9-23 in negative mode, each containing several mass spectral peaks corresponding to multiple charge states and oligomeric sizes under the same experimental conditions. The peaks are annotated by nominal m/z , where n is the oligomer size and z is the charge. The insets of the two mass spectra for the two peptides show that oligomers have up to a heptamer ($n = 7$) for Ins1 B9-23 and dodecamer ($n = 12$) for Ins2 B9-23. More oligomers can be observed in the higher mass region of the mass spectra for Ins2 B9-23 compared to Ins1 B9-23. The most dominant peak in the mass spectra is the $n/z = 1/2$, which contains mostly monomers. The experimental CCS for the $n/z = 1/2$ species is presented in Table S3 (along the CCS values for the same species of the other B9-23 peptides). The highlighted peak in the nominal $n/z = 1/1$ species, of which the 2D plots of diff time vs. m/z are shown in Figure 2C-D, respectively. This n/z peak, although less intense than $n/z = 1/2$, contains an abundance of isotopic oligomeric species. It is also the highest intensity peak of the oligomers. The 2D plot of m/z vs. diff time shows the separations of ions based on their m/z values and their arrival times. Therefore, various oligomers with the same m/z but different charge states can have distinct clusters in the 2D plot.

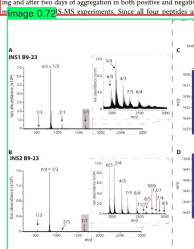


Figure 2. Representative mass spectra of (A) Ins1 B9-23 and (B) Ins2 B9-23. The insets in each region show zoomed-in regions where multiple oligomers are observed. The 2D plots for $n/z = 1/1$ are shown for both (C) Ins1 B9-23 and (D) Ins2 B9-23. TEM images of the peptides in 20 mM ammonium acetate are shown in (E) Ins1 B9-23 and (F) Ins2 B9-23. Filaments are observed in the image of Ins1 B9-23, whereas amorphous aggregates are observed in the image of Ins2 B9-23. The scale bar for the TEM images is 500 nm.

https://doi.org/10.26434/chemrxiv-2024-10-08-0000; https://arxiv.org/abs/2024.10-08-0000 Content not peer-reviewed by ChemRxiv. License: CC BY-NC-ND 4.0

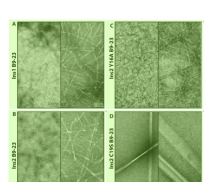


Figure 1. TEM images of the four B9-23 peptides in water obtained after one-week incubation at 37°C. (A) Ins1 B9-23, (B) Ins2 B9-23, (C) Ins3 B9-23 T16A, and (D) Ins2 B9-23 C19S. The peptide concentration is 100 μM.

All four insulin B9-23 peptides were analyzed immediately after mixing and after two days of aggregation in both positive and negative modes for the IMS-MS experiments. Since all four peptides are

negatively charged at physiological pH, the subsequent discussion in this work will be on the data acquired from the negative IMS polarity, but we will use the positive polarity data set as complementary. Figure 2A-B show the mass spectra of Ins1 B9-23 and Ins2 B9-23 in negative mode, each containing several mass spectral peaks corresponding to multiple charge states and oligomeric sizes under the same experimental conditions. The peaks are annotated by nominal m/z , where n is the oligomer size and z is the charge. The insets of the two mass spectra for the two peptides show that oligomers have up to a heptamer ($n = 7$) for Ins1 B9-23 and dodecamer ($n = 12$) for Ins2 B9-23. More oligomers can be observed in the higher mass region of the mass spectra for Ins2 B9-23 compared to Ins1 B9-23. The most dominant peak in the mass spectra is the $n/z = 1/2$, which contains mostly monomers. The experimental CCS for the $n/z = 1/2$ species is presented in Table S3 (along the CCS values for the same species of the other B9-23 peptides). The highlighted peak in the nominal $n/z = 1/1$ species, of which the 2D plots of diff time vs. m/z are shown in Figure 2C-D, respectively. This n/z peak, although less intense than $n/z = 1/2$, contains an abundance of isotopic oligomeric species. It is also the highest intensity peak of the oligomers. The 2D plot of m/z vs. diff time shows the separations of ions based on their m/z values and their arrival times. Therefore, various oligomers with the same m/z but different charge states can have distinct clusters in the 2D plot.

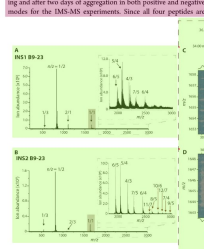
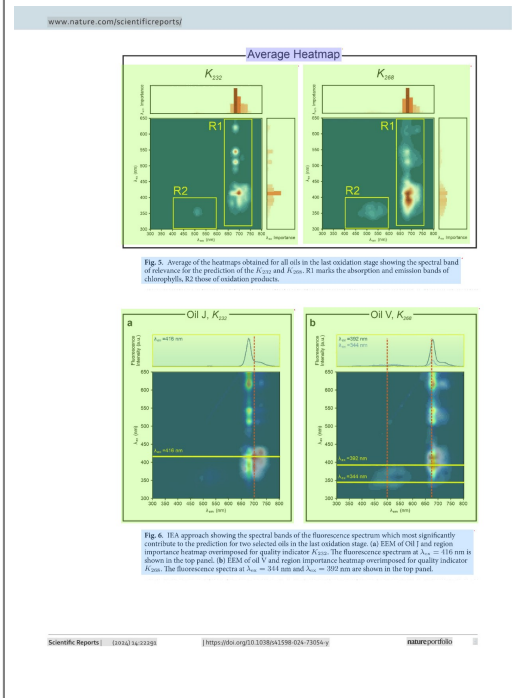
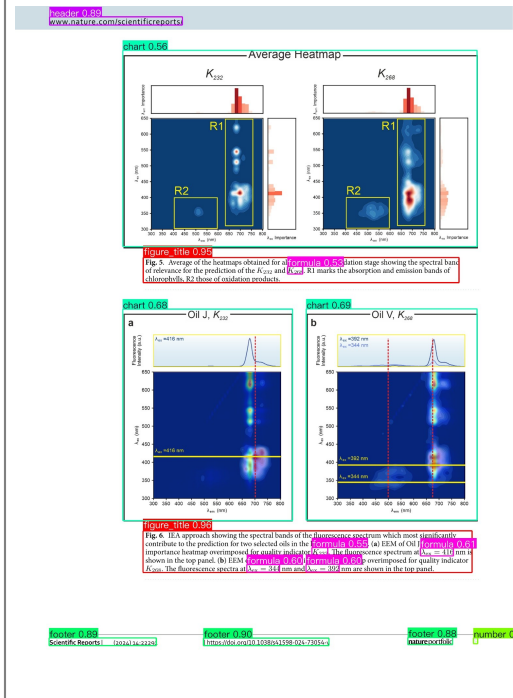
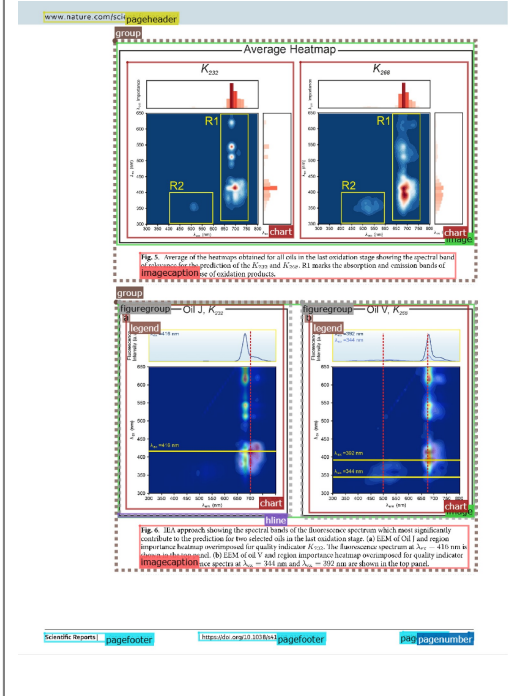
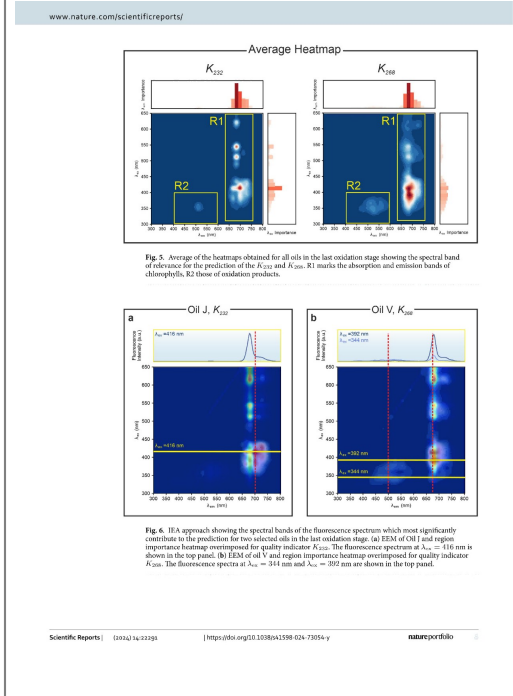
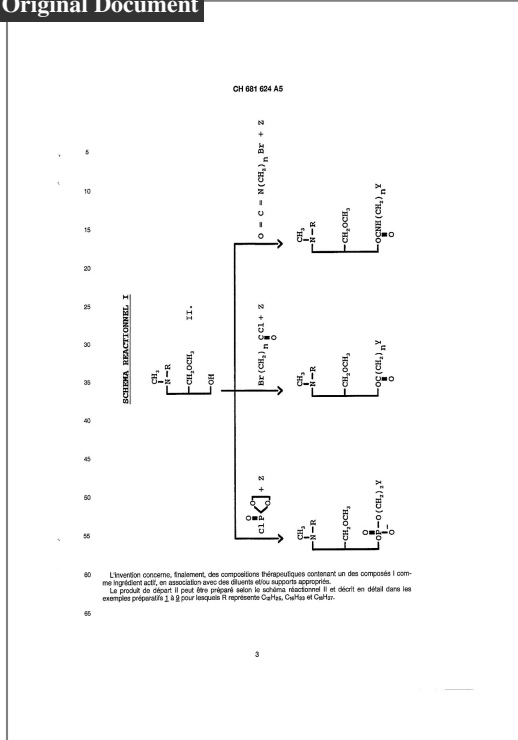


Figure 2. Representative mass spectra of (A) Ins1 B9-23 and (B) Ins2 B9-23. The insets in each region show zoomed-in regions where multiple oligomers are observed. The 2D plots for $n/z = 1/1$ are shown for both (C) Ins1 B9-23 and (D) Ins2 B9-23. TEM images of the peptides in 20 mM ammonium acetate are shown in (E) Ins1 B9-23 and (F) Ins2 B9-23. Filaments are observed in the image of Ins1 B9-23, whereas amorphous aggregates are observed in the image of Ins2 B9-23. The scale bar for the TEM images is 500 nm.

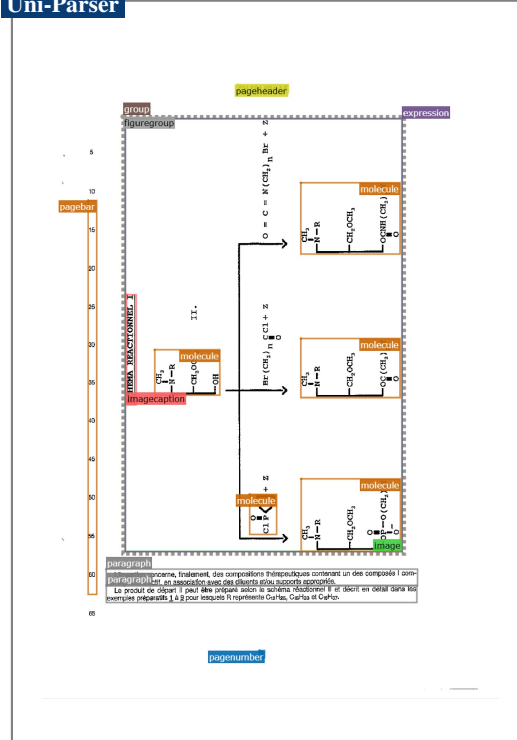
https://doi.org/10.26434/chemrxiv-2024-10-08-0000; https://arxiv.org/abs/2024.10-08-0000 Content not peer-reviewed by ChemRxiv. License: CC BY-NC-ND 4.0



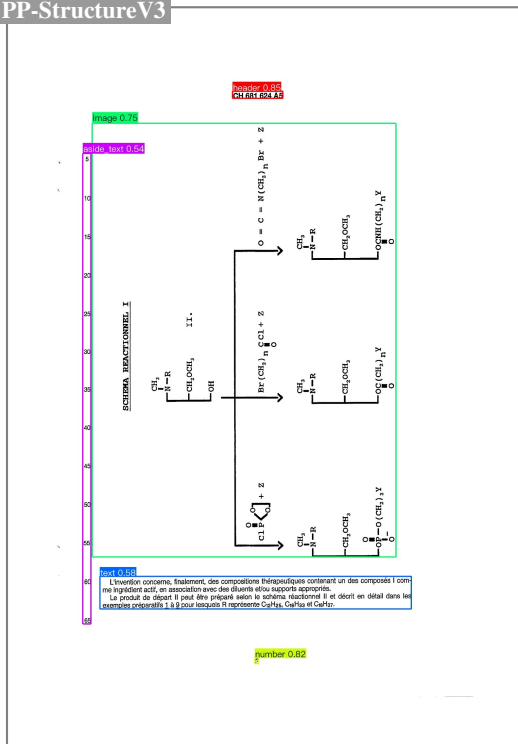
Original Document



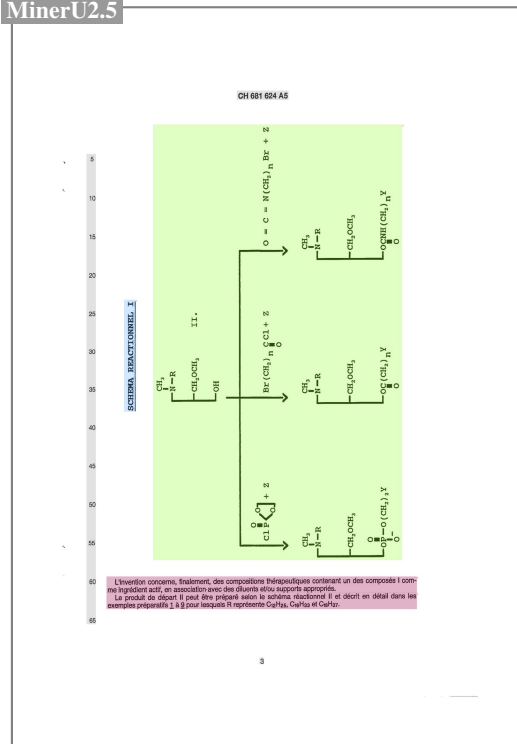
Uni-Parser



PP-StructureV3



MinerU2.5



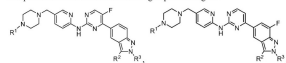
Original Document

WO 2016/01494 PCT/US2015/04195

(b)

wherein R¹ is preferably hydrogen or halogen; and when R¹ is a halogen, it is preferably chlorine or fluorine, more preferably fluorine.

In certain preferred embodiments of this aspect, the present invention provides a compound of formula selected from the group consisting of:



(c)

(d)

and

(e)

or a pharmaceutically acceptable salt, solvate, or prodrug thereof, wherein R¹, R², and R³ are each defined in any of the embodiments described here.

In certain preferred embodiments of this aspect, the present invention provides the compounds listed in Table 1 (i) (a), and pharmaceutically acceptable salts, solvates, and prodrugs thereof.

In another aspect, the present invention provides a pharmaceutical composition comprising a compound of formula (I), (II), (B), (C), (D), or (E) according to any embodiments described here, or a pharmaceutically acceptable salt, solvate, or prodrug thereof, and one or more pharmaceutically acceptable adjuvants, diluents, and/or carriers.

In another aspect, the present invention provides a method of treating a disease, disorder, or condition mediated through activity of at least one cyclin-dependent kinase (CDK), comprising administering to a subject in need thereof a therapeutically effective amount of the compound of formula (I), (II), (B), (C), (D), or (E) according to any of the

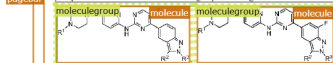
Uni-Parser

pageheader pageheader

paragraph (b)

wherein R¹ is preferably hydrogen or halogen; and when R¹ is a halogen, it is preferably chlorine or fluorine, more preferably fluorine.

In certain preferred embodiments of this aspect, the present invention provides a compound of formula selected from the group consisting of:



(c)

(d)

and

(e)

or a pharmaceutically acceptable salt, solvate, or prodrug thereof, wherein R¹, R², and R³ are each defined in any of the embodiments described here.

In certain preferred embodiments of this aspect, the present invention provides the compounds listed in Table 1 (i) (a), and pharmaceutically acceptable salts, solvates, and prodrugs thereof.

In another aspect, the present invention provides a pharmaceutical composition comprising a compound of formula (I), (II), (B), (C), (D), or (E) according to any embodiments described here, or a pharmaceutically acceptable salt, solvate, or prodrug thereof, and one or more pharmaceutically acceptable adjuvants, diluents, and/or carriers.

In another aspect, the present invention provides a method of treating a disease, disorder, or condition mediated through activity of at least one cyclin-dependent kinase (CDK), comprising administering to a subject in need thereof a therapeutically effective amount of the compound of formula (I), (II), (B), (C), (D), or (E) according to any of the

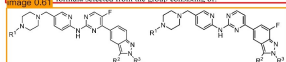
PP-StructureV3

Parser 0.31 Parser 0.32

(b)

wherein R¹ is preferably hydrogen or halogen; and when R¹ is a halogen, it is preferably chlorine or fluorine, more preferably fluorine.

In certain preferred embodiments of this aspect, the present invention provides a compound of formula selected from the group consisting of:



(c)

(d)

and

(e)

or a pharmaceutically acceptable salt, solvate, or prodrug thereof, wherein R¹, R², and R³ are each defined in any of the embodiments described here.

In certain preferred embodiments of this aspect, the present invention provides the compounds listed in Table 1 (i) (a), and pharmaceutically acceptable salts, solvates, and prodrugs thereof.

In another aspect, the present invention provides a pharmaceutical composition comprising a compound of formula (I), (II), (B), (C), (D), or (E) according to any embodiments described here, or a pharmaceutically acceptable salt, solvate, or prodrug thereof, and one or more pharmaceutically acceptable adjuvants, diluents, and/or carriers.

In another aspect, the present invention provides a method of treating a disease, disorder, or condition mediated through activity of at least one cyclin-dependent kinase (CDK), comprising administering to a subject in need thereof a therapeutically effective amount of the compound of formula (I), (II), (B), (C), (D), or (E) according to any of the

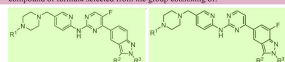
MinerU2.5

WO 2016/01494 PCT/US2015/04195

(b)

wherein R¹ is preferably hydrogen or halogen; and when R¹ is a halogen, it is preferably chlorine or fluorine, more preferably fluorine.

In certain preferred embodiments of this aspect, the present invention provides a compound of formula selected from the group consisting of:



(c)

(d)

and

(e)

or a pharmaceutically acceptable salt, solvate, or prodrug thereof, wherein R¹, R², and R³ are each defined in any of the embodiments described here.

In certain preferred embodiments of this aspect, the present invention provides the compounds listed in Table 1 (i) (a), and pharmaceutically acceptable salts, solvates, and prodrugs thereof.

In another aspect, the present invention provides a pharmaceutical composition comprising a compound of formula (I), (II), (B), (C), (D), or (E) according to any embodiments described here, or a pharmaceutically acceptable salt, solvate, or prodrug thereof, and one or more pharmaceutically acceptable adjuvants, diluents, and/or carriers.

In another aspect, the present invention provides a method of treating a disease, disorder, or condition mediated through activity of at least one cyclin-dependent kinase (CDK), comprising administering to a subject in need thereof a therapeutically effective amount of the compound of formula (I), (II), (B), (C), (D), or (E) according to any of the

B.4 Qualitative Examples of Reading Order

Original Document

S. JAIN, J. ALONSO, M. GRAU, and J.P. HOME

PHYS. REV. X 10, 031027 (2020)

add, because the lower-frequency mode of the pair is a magnetron mode and, thus, has a negative frequency. If only these two modes are included in the gate, it could be performed in a time of $t_g = 2\pi/\Delta\omega_{\pm}$ by using a Rabi frequency $\Omega = \Delta\omega_{\pm}/\sqrt{2}$. In practice, the contributions of the COM modes subtract from this effect, and the additional bulk modes also contribute. For a Lamb-Dicke parameter of $q = 0.17$ for the stretch modes, simulations involving all modes show that a Rabi frequency of $E_{01}/\hbar = 2\pi \times 300$ MHz could be used to perform a gate which would produce a Bell state with a fidelity of $F = 0.9998$ in 16 μs . The large zero-point motion means that a Raman beam pair with a small difference wave vector is required to operate within the Lamb-Dicke regime, which is desirable for insensitivity of gate fidelity to the initial ion temperature [45]. For beryllium, this beam pair would require an angle of $\theta_{\pm} = \pi/36$ for the beryllium wavelength of 313 nm.

Alternatively, a magnetic field gradient of approximately 19 T/m (lower than that realized in recent experiments [54]) would provide a gate with the same speed. Note that the motional mode parameters used in this analysis are chosen to satisfy a close-to-integer ratio between Δ_{\pm} and Δ_{\pm} , such that both the local stretch and COM modes are disentangled from the internal states at the end of the gate [45].

These results indicate that local changes to the potential, combined with individual optical or microwave addressing of the ions, could be used to realize quantum computing in the proposed architecture. The enhanced zero-point motion used here is particularly appealing in the context of

magnetic field gradient gates, which struggle to achieve high gate speeds in Paul trap settings due to the challenge of producing high field gradients [54–57]. In the presence of high Rabi frequencies, faster gate speeds should be possible using multiple techniques following methods demonstrated in Paul traps [58,59]. For error correction, the need for regular detection of ancilla ions poses challenges with regards to measurement cross talk, which might require the use of selective electron shelving [40]. For parallelizing error-correction codes, it is necessary to select multiple pairs of ions at different points in the lattice and perform gates on each of these simultaneously. Here, the $1/d^2$ nature of the Coulomb mode coupling is advantageous.

X. IMPLEMENTATION EXAMPLE

As an example of a possible implementation of a two-dimensional Penning trap array suitable for quantum simulation, we consider a honeycomb lattice of 62 sites. The surface-electrode pattern required for such a layout with nearest-neighbor spacing of 30 μm is shown in Fig. 10. Applying a voltage of 13.5 V to the electrodes results in an axial trap frequency of $\omega_z = 2\pi \times 2.1$ MHz for beryllium ions. In a global magnetic field angled at $\theta = 20^\circ$ from the plane normal with a magnitude of $B_0 = 2.5$ T, we get a reduced cyclotron frequency of $\omega_{\pm} = 2\pi \times 3.73$ MHz and a magnetron frequency of $\omega_{\mp} = 2\pi \times 0.54$ MHz. In this setup, effective laser cooling requires an axialization field, which is generated by applying a drive to the r electrodes at a frequency of $\omega_r = \omega_z = 2\pi \times 4.27$ MHz and an amplitude of 4 V.

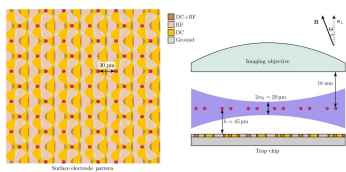


FIG. 10. Top and side view of an example trap architecture for a honeycomb array of 62 beryllium ions, with a nearest-neighbor distance $d = 30 \mu\text{m}$. Ions are trapped at a distance of $h = 45 \mu\text{m}$ above the surface of the electrodes and are globally addressed, cooled, and detected by laser light parallel to the surface. The electrodes labeled r generate the static electric potential, which, in conjunction with the global magnetic field, provides three-dimensional confinement at the sites marked in red. Tilting the magnetic field and the confining axis of the electric potential with respect to the normal of the electrode plane allows for laser cooling of all modes of motion with laser parallel to the surface. The electrodes labeled z provide the weak oscillating axialization field for laser cooling the radial modes of motion. Imaging is carried out with an objective placed at a working distance of 18 mm from the ions.

031027-12

Uni-Parser

S. JAIN, J. ALONSO, M. GRAU, and J.P. HOME

PHYS. REV. X 10, 031027 (2020)

add, because the lower-frequency mode of the pair is a magnetron mode and, thus, has a negative frequency. If only these two modes are included in the gate, it could be performed in a time of $t_g = 2\pi/\Delta\omega_{\pm}$ by using a Rabi frequency $\Omega = \Delta\omega_{\pm}/\sqrt{2}$. In practice, the contributions of the COM modes subtract from this effect, and the additional bulk modes also contribute. For a Lamb-Dicke parameter of $q = 0.17$ for the stretch modes, simulations involving all modes show that a Rabi frequency of $E_{01}/\hbar = 2\pi \times 300$ MHz could be used to perform a gate which would produce a Bell state with a fidelity of $F = 0.9998$ in 16 μs . The large zero-point motion means that a Raman beam pair with a small difference wave vector is required to operate within the Lamb-Dicke regime, which is desirable for insensitivity of gate fidelity to the initial ion temperature [45]. For beryllium, this beam pair would require an angle of $\theta_{\pm} = \pi/36$ for the beryllium wavelength of 313 nm.

Alternatively, a magnetic field gradient of approximately 19 T/m (lower than that realized in recent experiments [54]) would provide a gate with the same speed. Note that the motional mode parameters used in this analysis are chosen to satisfy a close-to-integer ratio between Δ_{\pm} and Δ_{\pm} , such that both the local stretch and COM modes are disentangled from the internal states at the end of the gate [45].

These results indicate that local changes to the potential, combined with individual optical or microwave addressing of the ions, could be used to realize quantum computing in the proposed architecture. The enhanced zero-point motion used here is particularly appealing in the context of

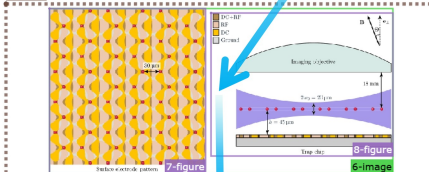


FIG. 10. Top and side view of an example trap architecture for a honeycomb array of 62 beryllium ions, with a nearest-neighbor distance $d = 30 \mu\text{m}$. Ions are trapped at a distance of $h = 45 \mu\text{m}$ above the surface of the electrodes and are globally addressed, cooled, and detected by laser light parallel to the surface. The electrodes labeled r generate the static electric potential, which, in conjunction with the global magnetic field, provides three-dimensional confinement at the sites marked in red. Tilting the magnetic field and the confining axis of the electric potential with respect to the normal of the electrode plane allows for laser cooling of all modes of motion with laser parallel to the surface. The electrodes labeled z provide the weak oscillating axialization field for laser cooling the radial modes of motion. Imaging is carried out with an objective placed at a working distance of 18 mm from the ions.

13-pagenumber

Original Document

SCALABLE ARRAYS OF MICRO-PENNING TRAPS FOR ...

PHYS. REV. X 10, 031027 (2020)

The electrostatic potential acting on the ion j due to the Coulomb interaction with other ions is

$$V_{\text{Coul}} = \sum_{i \neq j} \frac{1}{4\pi\epsilon_0} \frac{q_i q_j}{|\mathbf{R}_i - \mathbf{R}_j|} \quad (\text{B1})$$

where m_j is the mass of the j th ion.

The normal-mode analysis begins by finding the equilibrium configuration of sites $\{\mathbf{R}_i\}$, which is determined by the minimum of the total potential energy. By expanding the system Lagrangian about the equilibrium position of each ion in a Taylor series to second order, we get a Lagrangian in terms of the generalized position vectors $\mathbf{r}_i = \mathbf{R}_i - \mathbf{R}_i^0$, which specify the displacement of each ion from its equilibrium point. The second-order term in the expansion effectively determines the normal-mode dynamics of the system near the stable spatial configuration and is given by

$$L = \sum_j \left[\frac{1}{2} m_j \dot{\mathbf{r}}_j^2 + \frac{1}{2} (\mathbf{B} \times \mathbf{r}_j) \cdot \dot{\mathbf{r}}_j + \sum_{i,j} \frac{1}{2} \mathbf{r}_i^T \mathbf{K}_{ij} \mathbf{r}_j \right] \quad (\text{B2})$$

We proceed by putting together all the generalized position coordinates into a single $3N$ -dimensional vector $\mathbf{q} = [x_1, \dots, x_N, y_1, \dots, y_N, z_1, \dots, z_N]^T$ and introducing the $3N \times 3N$ block matrices M , W , V , and K constructed in terms of $N \times N$ submatrices as

$$M = \begin{pmatrix} M^x & 0 & 0 \\ 0 & M^y & 0 \\ 0 & 0 & M^z \end{pmatrix}, \quad W = eB_0 \begin{pmatrix} 0 & \cos\theta & 0 \\ -\cos\theta & 0 & 0 \\ 0 & 0 & 0 \end{pmatrix}, \quad V = \begin{pmatrix} V^x & 0 & 0 \\ 0 & V^y & 0 \\ 0 & 0 & V^z \end{pmatrix}, \quad K = \begin{pmatrix} K^x & 0 & 0 \\ 0 & K^y & 0 \\ 0 & 0 & K^z \end{pmatrix} \quad (\text{B4})$$

Here, \mathbf{I}_N and \mathbf{O}_N represent the $N \times N$ identity and zero matrices, respectively, and the components of other submatrices are defined as

$$M^{\alpha} = m_j \delta_{ij}, \quad V^{\alpha} = 2\pi^2 q_i^{\alpha} q_j^{\alpha} / \epsilon_0, \quad K^{\alpha} = \begin{pmatrix} -k_x & 0 & 0 \\ 0 & -k_y & 0 \\ 0 & 0 & -k_z \end{pmatrix}, \quad j, k = 1, \dots, N \quad (\text{B5})$$

where indices i and j run from 1 to N while again the indices α and β refer to the components x , y , and z . The above definitions together with $\Phi = V + K$ allow us to write the effective phonon Lagrangian compactly as

$$L = \sum_j \left[\frac{1}{2} M_j \dot{\mathbf{q}}_j^2 - \frac{1}{2} \mathbf{q}_j^T \Phi \mathbf{q}_j - \frac{1}{2} \sum_{i,j} \mathbf{q}_i^T \mathbf{K}_{ij} \mathbf{q}_j \right] \quad (\text{B6})$$

It should be clear that M is a real diagonal matrix, while W is a real antisymmetric matrix. The matrix V is traceless as a direct consequence of Laplace's equation, while the matrix K is traceless, because the Coulomb forces being internal forces in the system of ions pairwise cancel each other and the total sum equates to zero. V and K are also both real and symmetric. As a result, $\Phi = V + K$ is a real symmetric

matrix, respectively, and the components of other submatrices are defined

$$M^{\alpha} = m_j \delta_{ij}, \quad V^{\alpha} = 2\pi^2 q_i^{\alpha} q_j^{\alpha} / \epsilon_0, \quad K^{\alpha} = \begin{pmatrix} -k_x & 0 & 0 \\ 0 & -k_y & 0 \\ 0 & 0 & -k_z \end{pmatrix}, \quad j, k = 1, \dots, N \quad (\text{B7a})$$

where indices i and j run from 1 to N while again the indices α and β refer to the components x , y , and z . The above definitions together with $\Phi = V + K$ allow us to write the effective phonon Lagrangian compactly as

$$L = \sum_j \left[\frac{1}{2} M_j \dot{\mathbf{q}}_j^2 - \frac{1}{2} \mathbf{q}_j^T \Phi \mathbf{q}_j - \frac{1}{2} \sum_{i,j} \mathbf{q}_i^T \mathbf{K}_{ij} \mathbf{q}_j \right] \quad (\text{B7b})$$

031027-15

Uni-Parser

SCALABLE ARRAYS OF MICRO-PENNING TRAPS FOR ...

PHYS. REV. X 10, 031027 (2020)

The electrostatic potential acting on the ion j due to the Coulomb interaction with other ions is

$$V_{\text{Coul}} = \sum_{i \neq j} \frac{1}{4\pi\epsilon_0} \frac{q_i q_j}{|\mathbf{R}_i - \mathbf{R}_j|} \quad (\text{B1})$$

where m_j is the mass of the j th ion.

The normal-mode analysis begins by finding the equilibrium configuration of sites $\{\mathbf{R}_i\}$, which is determined by the minimum of the total potential energy. By expanding the system Lagrangian about the equilibrium position of each ion in a Taylor series to second order, we get a Lagrangian in terms of the generalized position vectors $\mathbf{r}_i = \mathbf{R}_i - \mathbf{R}_i^0$, which specify the displacement of each ion from its equilibrium point. The second-order term in the expansion effectively determines the normal-mode dynamics of the system near the stable spatial configuration and is given by

$$L = \sum_j \left[\frac{1}{2} m_j \dot{\mathbf{r}}_j^2 + \frac{1}{2} (\mathbf{B} \times \mathbf{r}_j) \cdot \dot{\mathbf{r}}_j + \sum_{i,j} \frac{1}{2} \mathbf{r}_i^T \mathbf{K}_{ij} \mathbf{r}_j \right] \quad (\text{B2})$$

We proceed by putting together all the generalized position coordinates into a single $3N$ -dimensional vector $\mathbf{q} = [x_1, \dots, x_N, y_1, \dots, y_N, z_1, \dots, z_N]^T$ and introducing the $3N \times 3N$ block matrices M , W , V , and K constructed in terms of $N \times N$ submatrices as

$$M = \begin{pmatrix} M^x & 0 & 0 \\ 0 & M^y & 0 \\ 0 & 0 & M^z \end{pmatrix}, \quad W = eB_0 \begin{pmatrix} 0 & \cos\theta & 0 \\ -\cos\theta & 0 & 0 \\ 0 & 0 & 0 \end{pmatrix}, \quad V = \begin{pmatrix} V^x & 0 & 0 \\ 0 & V^y & 0 \\ 0 & 0 & V^z \end{pmatrix}, \quad K = \begin{pmatrix} K^x & 0 & 0 \\ 0 & K^y & 0 \\ 0 & 0 & K^z \end{pmatrix} \quad (\text{B4})$$

Here, \mathbf{I}_N and \mathbf{O}_N represent the $N \times N$ identity and zero matrices, respectively, and the components of other submatrices are defined as

$$M^{\alpha} = m_j \delta_{ij}, \quad V^{\alpha} = 2\pi^2 q_i^{\alpha} q_j^{\alpha} / \epsilon_0, \quad K^{\alpha} = \begin{pmatrix} -k_x & 0 & 0 \\ 0 & -k_y & 0 \\ 0 & 0 & -k_z \end{pmatrix}, \quad j, k = 1, \dots, N \quad (\text{B5})$$

where indices i and j run from 1 to N while again the indices α and β refer to the components x , y , and z . The above definitions together with $\Phi = V + K$ allow us to write the effective phonon Lagrangian compactly as

$$L = \sum_j \left[\frac{1}{2} M_j \dot{\mathbf{q}}_j^2 - \frac{1}{2} \mathbf{q}_j^T \Phi \mathbf{q}_j - \frac{1}{2} \sum_{i,j} \mathbf{q}_i^T \mathbf{K}_{ij} \mathbf{q}_j \right] \quad (\text{B6})$$

It should be clear that M is a real diagonal matrix, while W is a real antisymmetric matrix. The matrix V is traceless as a direct consequence of Laplace's equation, while the matrix K is traceless, because the Coulomb forces being internal forces in the system of ions pairwise cancel each other and the total sum equates to zero. V and K are also both real and symmetric. As a result, $\Phi = V + K$ is a real symmetric

matrix, respectively, and the components of other submatrices are defined

$$M^{\alpha} = m_j \delta_{ij}, \quad V^{\alpha} = 2\pi^2 q_i^{\alpha} q_j^{\alpha} / \epsilon_0, \quad K^{\alpha} = \begin{pmatrix} -k_x & 0 & 0 \\ 0 & -k_y & 0 \\ 0 & 0 & -k_z \end{pmatrix}, \quad j, k = 1, \dots, N \quad (\text{B7a})$$

where indices i and j run from 1 to N while again the indices α and β refer to the components x , y , and z . The above definitions together with $\Phi = V + K$ allow us to write the effective phonon Lagrangian compactly as

$$L = \sum_j \left[\frac{1}{2} M_j \dot{\mathbf{q}}_j^2 - \frac{1}{2} \mathbf{q}_j^T \Phi \mathbf{q}_j - \frac{1}{2} \sum_{i,j} \mathbf{q}_i^T \mathbf{K}_{ij} \mathbf{q}_j \right] \quad (\text{B7b})$$

45-pagefooter

Original Document

and the full geometry is properly interpreted as a gluing of Lorentzian $\mathbb{S}^2_{\text{Lor}}$ and Euclidean $\mathbb{S}^2_{\text{Euc}}$, joined smoothly at the hypersurface $r = r_0 = 0$ [3].

In this setup, the pseudotopology associated with a subregion A on the boundary \mathbb{S}^2 [5], can be computed holographically by extending the Ryu-Takayanagi (RT) prescription to \mathbb{S}^2 -space—see Eq. (8) below—which leads to a complex-valued codimension-two area functional in the bulk. Moreover, in [3], it was shown that for a ball-shaped entangling region $A = \mathbb{B}^{d-1}$ with entangling surface $\partial A = \mathbb{S}^{d-2}$, defined on the $\theta = 0$ slice, the universal part of holographic pseudotopology, i.e.,

$$S(\mathbb{B}^{d-1}) \supset \begin{cases} (-1)^{\frac{d-1}{2}} S_{\text{Euc}}(\mathbb{B}^{d-1}) & \text{if odd } d, \\ (-1)^{\frac{d-1}{2}} S_{\text{Lor}}(\mathbb{B}^{d-1}) \log \frac{d-1}{2} & \text{if even } d, \end{cases} \quad (4)$$

where T_0 is a characteristic length of the subregion and δ is an arbitrary regulator, contains information regarding the complex-valued central charge of the dual Euclidean CFT. Notice that in even dimensions there is a universal contribution at finite order, which is not contaminated by a physical renormalization of δ . This term relates to timelike entanglement entropy by analytic continuation of T_0 .

Moving away from the ball-shaped region, we consider a slightly deformed ball $A = \mathbb{B}^{d-1}_\epsilon$ of unit radius, where $\epsilon \ll 1$ is a small deformation parameter. The shape de-

$$S_{\text{Euc}}^{\text{deformed}} = C_V \frac{\pi^{d/2} (d-1)}{2^{d-1} \Gamma(d/2)} \sum_{\ell=0}^{\infty} c_{\ell}^{\text{Euc}} (-1)^\ell \times \begin{cases} \pi/2 & \text{if odd } d, \\ 1 & \text{if even } d, \end{cases} \quad (7)$$

where $C_V = \prod_{k=1}^{\infty} (2k-1)!$ is the Pochhammer symbol. The coefficient C_V —see Eq. (18) below—characterizes the two-point stress tensor correlator [11], $\langle T_{\mu\nu}(x) T_{\mu\nu}(0) \rangle = C_V x^{2d} / \Gamma(d)$, with $\langle T_{\mu\nu} \rangle = \delta_{\mu\nu} - 2x_\mu x_\nu / r^2$ [3]. As opposed to unitary CFTs, where $C_V > 0$, this may vanish, become negative, or even take complex values in nonunitary theories—see, e.g., [3, 33–35].

Our main result, Eq. (7)—together with Eq. (18) and Eq. (21) below, extends Meier's formula for entanglement entropy [17, 38] to a universality class of non-unitary CFTs with gravity duals, showing that the pseudotopology of a perturbatively deformed spherical entangling surface still satisfies the same structural relation as in the unitary AdS-CFT case.

Holographic pseudotopology for perturbed spheres. For holographic Euclidean CFTs dual to Einstein-dS defined at timelike future infinity, the pseudotopology is given by

$$S(\mathbb{B}^{d-1}) = T_0 \frac{\pi}{2} + \sum_{\ell=0}^{\infty} c_{\ell}^{\text{Euc}} Y_{\ell,0}, \quad (5)$$

where $Y_{\ell,0} = Y_{\ell,0}(\Omega_{d-2})$ are the $(d-2)$ -spherical harmonics with quantum numbers $\ell = 0, 1, \dots, \ell_{\text{max}}$, satisfying $\Delta Y_{\ell,0} = -\ell(\ell+2-d)Y_{\ell,0}$ with Δ denoting the Laplace-Beltrami operator on \mathbb{S}^{d-2} , and Ω_{d-2} the amplitude of the deformation. In general, the Euclidean time coordinate ranges as $t \in [0, \pi]$. A fixed value of t_0 specifies a ball-shaped entangling subregion of radius $r = \tan(t_0/2)$ via stereographic projection. In particular, the value $t_0 = T_0 = \pi/2$ corresponds to the unit-radius case of interest. Figure 1 illustrates the deformation profile (5).

Using this setup in this letter, we conclude that, for a broad class of non-unitary CFTs—namely, those admitting a dual description in terms of some gravitational theory—the universal part of the pseudotopology admits the equation

$$S_{\text{Euc}}(\mathbb{B}^{d-1}) = S_{\text{Euc}}^{\text{deformed}} + S_{\text{Lor}}^{\text{deformed}} = \begin{cases} 2\pi\alpha' & \text{if odd } d, \\ \frac{1}{2} \log \frac{d-1}{2} & \text{if even } d, \end{cases} \quad (6)$$

where $\alpha' = (-1)^{\frac{d-1}{2}} \pi^{d/2} \ell_{\text{Pl}}^{d-1} / 8\pi G_N(2G_N)$ is the renormalized central charge of the non-unitary CFT [11] with the leading correction, at quadratic order in ϵ , computed

$$S(A) = \frac{\text{Area}(\Sigma_A)}{4G_N} \quad (8)$$

where the codimension-two surface Σ_A is extremal in the dS bulk. The pseudotopology area functional in dS space contains both timelike and spacelike sections, i.e., $\Sigma_A = \Sigma_A^{\text{timelike}} \cup \Sigma_A^{\text{spacelike}}$, and consequently $S(A) = S^{\text{timelike}}(A) + S^{\text{spacelike}}(A)$. The timelike part, S^{timelike} , is embedded in the Lorentzian section of the bulk $\mathbb{S}^2_{\text{Lor}}$ geometry (2). On the other hand, the spacelike part $S^{\text{spacelike}}$ is embedded in the Euclidean section of the bulk $\mathbb{S}^2_{\text{Euc}}$, given in Eq. (3).

The extremal surface Σ_A is determined by requiring the trace of the extrinsic curvature along each normal direction n^i to vanish separately. Explicitly, $K^i = h^{\mu\nu} K_{\mu\nu}^i = h^{\mu\nu} \partial_\mu \nabla_\nu n^i$, where $h_{\mu\nu}$ is the induced metric, ∂_μ its projector, and ∇_ν the independent spacelike and timelike normals to the codimension-two surface Σ_A . Using the embedding function $n_i = t_0(\tau, \Omega_{d-2})$ for the

Uni-Parser

0-paragraph and the full geometry is properly interpreted as a gluing of Lorentzian $\mathbb{S}^2_{\text{Lor}}$ and Euclidean $\mathbb{S}^2_{\text{Euc}}$, joined smoothly at the hypersurface $r = r_0 = 0$ [3].

12-paragraph In this setup, the pseudotopology associated with a subregion A on the boundary \mathbb{S}^2 [5], can be computed holographically by extending the Ryu-Takayanagi (RT) prescription to \mathbb{S}^2 -space—see Eq. (8) below—which leads to a complex-valued codimension-two area functional in the bulk. Moreover, in [3], it was shown that for a ball-shaped entangling region $A = \mathbb{B}^{d-1}$ with entangling surface $\partial A = \mathbb{S}^{d-2}$, defined on the $\theta = 0$ slice, the universal part of holographic pseudotopology, i.e.,

2-paragraph $S(\mathbb{B}^{d-1}) \supset \begin{cases} (-1)^{\frac{d-1}{2}} S_{\text{Euc}}(\mathbb{B}^{d-1}) & \text{if odd } d, \\ (-1)^{\frac{d-1}{2}} S_{\text{Lor}}(\mathbb{B}^{d-1}) \log \frac{d-1}{2} & \text{if even } d, \end{cases}$

4-paragraph where T_0 is a characteristic length of the subregion and δ is an arbitrary regulator, contains information regarding the complex-valued central charge of the dual Euclidean CFT. Notice that in even dimensions there is a universal contribution at finite order, which is not contaminated by a physical renormalization of δ . This term relates to timelike entanglement entropy by analytic continuation of T_0 .

6-paragraph Moving away from the ball-shaped region, we consider a slightly deformed ball $A = \mathbb{B}^{d-1}_\epsilon$ of unit radius, where $\epsilon \ll 1$ is a small deformation parameter. The shape de-

8-paragraph $S_{\text{Euc}}^{\text{deformed}} = C_V \frac{\pi^{d/2} (d-1)}{2^{d-1} \Gamma(d/2)} \sum_{\ell=0}^{\infty} c_{\ell}^{\text{Euc}} (-1)^\ell \times \begin{cases} \pi/2 & \text{if odd } d, \\ 1 & \text{if even } d, \end{cases}$

10-equation where $C_V = \prod_{k=1}^{\infty} (2k-1)!$ is the Pochhammer symbol. The coefficient C_V —see Eq. (18) below—characterizes the two-point stress tensor correlator [11], $\langle T_{\mu\nu}(x) T_{\mu\nu}(0) \rangle = C_V x^{2d} / \Gamma(d)$, with $\langle T_{\mu\nu} \rangle = \delta_{\mu\nu} - 2x_\mu x_\nu / r^2$ [3]. As opposed to unitary CFTs, where $C_V > 0$, this may vanish, become negative, or even take complex values in nonunitary theories—see, e.g., [3, 33–35].

12-paragraph Our main result, Eq. (7)—together with Eq. (18) and Eq. (21) below, extends Meier's formula for entanglement entropy [17, 38] to a universality class of non-unitary CFTs with gravity duals, showing that the pseudotopology of a perturbatively deformed spherical entangling surface still satisfies the same structural relation as in the unitary AdS-CFT case.

14-equation **Holographic pseudotopology for perturbed spheres.** For holographic Euclidean CFTs dual to Einstein-dS defined at timelike future infinity, the pseudotopology is given by

16-equation $S(\mathbb{B}^{d-1}) = T_0 \frac{\pi}{2} + \sum_{\ell=0}^{\infty} c_{\ell}^{\text{Euc}} Y_{\ell,0}$

18-equation where $Y_{\ell,0} = Y_{\ell,0}(\Omega_{d-2})$ are the $(d-2)$ -spherical harmonics with quantum numbers $\ell = 0, 1, \dots, \ell_{\text{max}}$, satisfying $\Delta Y_{\ell,0} = -\ell(\ell+2-d)Y_{\ell,0}$ with Δ denoting the Laplace-Beltrami operator on \mathbb{S}^{d-2} , and Ω_{d-2} the amplitude of the deformation. In general, the Euclidean time coordinate ranges as $t \in [0, \pi]$. A fixed value of t_0 specifies a ball-shaped entangling subregion of radius $r = \tan(t_0/2)$ via stereographic projection. In particular, the value $t_0 = T_0 = \pi/2$ corresponds to the unit-radius case of interest. Figure 1 illustrates the deformation profile (5).

20-equation Using this setup in this letter, we conclude that, for a broad class of non-unitary CFTs—namely, those admitting a dual description in terms of some gravitational theory—the universal part of the pseudotopology admits the equation

22-equation $S_{\text{Euc}}(\mathbb{B}^{d-1}) = S_{\text{Euc}}^{\text{deformed}} + S_{\text{Lor}}^{\text{deformed}} = \begin{cases} 2\pi\alpha' & \text{if odd } d, \\ \frac{1}{2} \log \frac{d-1}{2} & \text{if even } d, \end{cases}$

24-equation where $\alpha' = (-1)^{\frac{d-1}{2}} \pi^{d/2} \ell_{\text{Pl}}^{d-1} / 8\pi G_N(2G_N)$ is the renormalized central charge of the non-unitary CFT [11] with the leading correction, at quadratic order in ϵ , computed

26-equation $S(A) = \frac{\text{Area}(\Sigma_A)}{4G_N}$

28-equation where the codimension-two surface Σ_A is extremal in the dS bulk. The pseudotopology area functional in dS space contains both timelike and spacelike sections, i.e., $\Sigma_A = \Sigma_A^{\text{timelike}} \cup \Sigma_A^{\text{spacelike}}$, and consequently $S(A) = S^{\text{timelike}}(A) + S^{\text{spacelike}}(A)$. The timelike part, S^{timelike} , is embedded in the Lorentzian section of the bulk $\mathbb{S}^2_{\text{Lor}}$ geometry (2). On the other hand, the spacelike part $S^{\text{spacelike}}$ is embedded in the Euclidean section of the bulk $\mathbb{S}^2_{\text{Euc}}$, given in Eq. (3).

30-equation The extremal surface Σ_A is determined by requiring the trace of the extrinsic curvature along each normal direction n^i to vanish separately. Explicitly, $K^i = h^{\mu\nu} K_{\mu\nu}^i = h^{\mu\nu} \partial_\mu \nabla_\nu n^i$, where $h_{\mu\nu}$ is the induced metric, ∂_μ its projector, and ∇_ν the independent spacelike and timelike normals to the codimension-two surface Σ_A . Using the embedding function $n_i = t_0(\tau, \Omega_{d-2})$ for the

Original Document



Figure 2. (Left) Front view of the RT surface for small perturbations around the ball-shaped entangling region at future infinity. (Right) Top view of the same RT surface. The timelike section is shown in orange, while the spacelike part is highlighted in blue. The black line indicates the junction at $r = r_0 = 0$. The sketch is not conformal; therefore, the upper part does not correspond to future infinity, but to some value of $0 < r < \infty$.

spacelike parts of the RT surface—in contrast with the undeformed case, where the finite piece comes only from the spacelike section, (i) parity-dependent terms with opposite signs. This, upon combining Eqs. (14) and (15) in odd dimensions, and Eqs. (16) and (17) in even dimensions, these terms cancel exactly, yielding the universal contributions given in (6) and (7). In the latter expressions, we identify the coefficient of the two-point stress-tensor trace for CFTs dual to Einstein-dS gravity as

$$C_V = \frac{(-1)^{\frac{d-1}{2}} \Gamma(d+2)}{8\pi^{d/2} \Gamma(d)} \frac{L_{\text{eff}}^2}{G_N}, \quad (18)$$

thus obtaining an analogue expansion in dS as the Meier formula for the entanglement entropy in AdS-CFT [17, 38]. The relationship between the dS and AdS formalisms can also be established through an analytic continuation, defined by $L_{\text{eff}} \rightarrow -iL_{\text{eff}}$, which implies $c_{\ell}^{\text{AdS}} \rightarrow c_{\ell}^{\text{dS}}$. In direct analogy, we see from Eq. (18) that the coefficient C_V transforms in the same way: $C_V^{\text{AdS}} \rightarrow C_V^{\text{dS}}$.

Higher-curvature gravity. To test the universality of Eq. (7), we extend our analysis to non-unitary CFTs dual to higher-curvature gravities. Since the replica trick induces the same orbifold structure in both dS and AdS spacetimes [1], one should expect pseudotopology in dS-CFT. In general gravity theories $\mathcal{L} = \mathcal{L}_{\text{EH}} + \mathcal{L}_{\text{curv}}$, to be captured by the Dong-Camp formula [15, 36] and apply it to the perturbative regime [17]. We write an analogue one of the simplest examples of higher-curvature gravity, in which universality properties can be probed, namely, quadratic gravity. This theory is defined by the sum of the three quadratic contractions of the Riemann tensor on top of the Einstein-Hilbert term, i.e., $\mathcal{L}_{\text{curv}} = R - \lambda_1 \lambda_2 \lambda_3 R^{\mu\nu} R^{\rho\sigma} + \lambda_4 R^{\mu\nu} R^{\rho\sigma}$, where λ_1, λ_2 and λ_3 are dimensional, undetermined coupling constants.

Using the results of [1] for scalars of quadratic order in the undeformed case, where the finite piece comes only from the spacelike section, (i) parity-dependent terms with opposite signs. This, upon combining Eqs. (14) and (15) in odd dimensions, and Eqs. (16) and (17) in even dimensions, these terms cancel exactly, yielding the universal contributions given in (6) and (7). In the latter expressions, we identify the coefficient of the two-point stress-tensor trace for CFTs dual to Einstein-dS gravity as

$$S_{\text{Euc}}(A) = \frac{1}{4G_N} \int_{\Sigma_A} \left[1 + 2\lambda_1 R + \lambda_2 \left(R^2 - \frac{1}{2} R_{\mu\nu} R^{\mu\nu} \right) + 2\lambda_3 (R_{\mu\nu} - R_{\mu\nu}^{\text{EH}}) \right], \quad (19)$$

where $R^i = R^{\mu\nu} n_\mu n_\nu$ is the Ricci tensor projected along the normal directions and $R_{\mu\nu}^i = R^{\mu\nu} n_\mu n_\nu \delta_{\mu\nu}^i$ is the corresponding projection of the Riemann tensor. Of course, setting $\lambda_1 = \lambda_2 = \lambda_3 = 0$ in Eq. (19) retrieves the RT formula in Eq. (8).

To evaluate Eq. (19), we note that dS space is maximally symmetric, with curvature tensor $R_{\mu\nu\rho\sigma} = (R/20) \delta_{\mu\nu} \delta_{\rho\sigma} - (R/10) \delta_{\mu\rho} \delta_{\nu\sigma}$, where R_0 now denotes the effective dS radius. Using this expression together with the Gauss-Codazzi-Mainardi relations [16], we substitute $\partial = \text{div} + 1/2$, $R_{\mu\nu} = 20/2$, and $R_{\mu\nu}^i = 2/2$. Imposing the extremal surface condition $K^i = 0$, we obtain

$$S_{\text{Euc}}(A) = \alpha_0 \frac{\text{Area}(\Sigma_A)}{4G_N} + \frac{\lambda_2}{20G_N} \int_{\Sigma_A} R_{\mu\nu} R^{\mu\nu}, \quad (20)$$

where the coefficient α_0 is given by $\alpha_0 = 1 + 2\lambda_2(d+1)\lambda_3 + \lambda_2 \lambda_3 + 2\lambda_2 \lambda_3/2$.

The first term in Eq. (20) coincides with that of the previous section, up to an overall rescaling of the constant. The second term, on the other hand, is computationally more involved. Nevertheless, its contribution to the universal part of the pseudotopology follows the same structural relation as the area contribution. In particular, the timelike and spacelike sectors exhibit parity-dependent terms that cancel each other. Summing all contributions, we recover the same structure

Uni-Parser

0-group

2-figure Figure 2. (Left) Front view of the RT surface for small perturbations around the ball-shaped entangling region at future infinity. (Right) Top view of the same RT surface. The timelike section is shown in orange, while the spacelike part is highlighted in blue. The black line indicates the junction at $r = r_0 = 0$. The sketch is not conformal; therefore, the upper part does not correspond to future infinity, but to some value of $0 < r < \infty$.

4-paragraph **Holographic pseudotopology for perturbed spheres.** For holographic Euclidean CFTs dual to Einstein-dS defined at timelike future infinity, the pseudotopology is given by

6-equation $S(\mathbb{B}^{d-1}) = T_0 \frac{\pi}{2} + \sum_{\ell=0}^{\infty} c_{\ell}^{\text{Euc}} Y_{\ell,0}$

8-equation where $Y_{\ell,0} = Y_{\ell,0}(\Omega_{d-2})$ are the $(d-2)$ -spherical harmonics with quantum numbers $\ell = 0, 1, \dots, \ell_{\text{max}}$, satisfying $\Delta Y_{\ell,0} = -\ell(\ell+2-d)Y_{\ell,0}$ with Δ denoting the Laplace-Beltrami operator on \mathbb{S}^{d-2} , and Ω_{d-2} the amplitude of the deformation. In general, the Euclidean time coordinate ranges as $t \in [0, \pi]$. A fixed value of t_0 specifies a ball-shaped entangling subregion of radius $r = \tan(t_0/2)$ via stereographic projection. In particular, the value $t_0 = T_0 = \pi/2$ corresponds to the unit-radius case of interest. Figure 1 illustrates the deformation profile (5).

10-equation Using this setup in this letter, we conclude that, for a broad class of non-unitary CFTs—namely, those admitting a dual description in terms of some gravitational theory—the universal part of the pseudotopology admits the equation

12-equation $S_{\text{Euc}}(\mathbb{B}^{d-1}) = S_{\text{Euc}}^{\text{deformed}} + S_{\text{Lor}}^{\text{deformed}} = \begin{cases} 2\pi\alpha' & \text{if odd } d, \\ \frac{1}{2} \log \frac{d-1}{2} & \text{if even } d, \end{cases}$

14-equation where $\alpha' = (-1)^{\frac{d-1}{2}} \pi^{d/2} \ell_{\text{Pl}}^{d-1} / 8\pi G_N(2G_N)$ is the renormalized central charge of the non-unitary CFT [11] with the leading correction, at quadratic order in ϵ , computed

16-equation $S(A) = \frac{\text{Area}(\Sigma_A)}{4G_N}$

18-equation where the codimension-two surface Σ_A is extremal in the dS bulk. The pseudotopology area functional in dS space contains both timelike and spacelike sections, i.e., $\Sigma_A = \Sigma_A^{\text{timelike}} \cup \Sigma_A^{\text{spacelike}}$, and consequently $S(A) = S^{\text{timelike}}(A) + S^{\text{spacelike}}(A)$. The timelike part, S^{timelike} , is embedded in the Lorentzian section of the bulk $\mathbb{S}^2_{\text{Lor}}$ geometry (2). On the other hand, the spacelike part $S^{\text{spacelike}}$ is embedded in the Euclidean section of the bulk $\mathbb{S}^2_{\text{Euc}}$, given in Eq. (3).

20-equation The extremal surface Σ_A is determined by requiring the trace of the extrinsic curvature along each normal direction n^i to vanish separately. Explicitly, $K^i = h^{\mu\nu} K_{\mu\nu}^i = h^{\mu\nu} \partial_\mu \nabla_\nu n^i$, where $h_{\mu\nu}$ is the induced metric, ∂_μ its projector, and ∇_ν the independent spacelike and timelike normals to the codimension-two surface Σ_A . Using the embedding function $n_i = t_0(\tau, \Omega_{d-2})$ for the

22-paragraph **Holographic pseudotopology for perturbed spheres.** For holographic Euclidean CFTs dual to Einstein-dS defined at timelike future infinity, the pseudotopology is given by

24-equation $S(\mathbb{B}^{d-1}) = T_0 \frac{\pi}{2} + \sum_{\ell=0}^{\infty} c_{\ell}^{\text{Euc}} Y_{\ell,0}$

26-equation where $Y_{\ell,0} = Y_{\ell,0}(\Omega_{d-2})$ are the $(d-2)$ -spherical harmonics with quantum numbers $\ell = 0, 1, \dots, \ell_{\text{max}}$, satisfying $\Delta Y_{\ell,0} = -\ell(\ell+2-d)Y_{\ell,0}$ with Δ denoting the Laplace-Beltrami operator on \mathbb{S}^{d-2} , and Ω_{d-2} the amplitude of the deformation. In general, the Euclidean time coordinate ranges as $t \in [0, \pi]$. A fixed value of t_0 specifies a ball-shaped entangling subregion of radius $r = \tan(t_0/2)$ via stereographic projection. In particular, the value $t_0 = T_0 = \pi/2$ corresponds to the unit-radius case of interest. Figure 1 illustrates the deformation profile (5).

28-equation Using this setup in this letter, we conclude that, for a broad class of non-unitary CFTs—namely, those admitting a dual description in terms of some gravitational theory—the universal part of the pseudotopology admits the equation

30-equation $S_{\text{Euc}}(\mathbb{B}^{d-1}) = S_{\text{Euc}}^{\text{deformed}} + S_{\text{Lor}}^{\text{deformed}} = \begin{cases} 2\pi\alpha' & \text{if odd } d, \\ \frac{1}{2} \log \frac{d-1}{2} & \text{if even } d, \end{cases}$

32-equation where $\alpha' = (-1)^{\frac{d-1}{2}} \pi^{d/2} \ell_{\text{Pl}}^{d-1} / 8\pi G_N(2G_N)$ is the renormalized central charge of the non-unitary CFT [11] with the leading correction, at quadratic order in ϵ , computed

34-equation $S(A) = \frac{\text{Area}(\Sigma_A)}{4G_N}$

36-equation where the codimension-two surface Σ_A is extremal in the dS bulk. The pseudotopology area functional in dS space contains both timelike and spacelike sections, i.e., $\Sigma_A = \Sigma_A^{\text{timelike}} \cup \Sigma_A^{\text{spacelike}}$, and consequently $S(A) = S^{\text{timelike}}(A) + S^{\text{spacelike}}(A)$. The timelike part, S^{timelike} , is embedded in the Lorentzian section of the bulk $\mathbb{S}^2_{\text{Lor}}$ geometry (2). On the other hand, the spacelike part $S^{\text{spacelike}}$ is embedded in the Euclidean section of the bulk $\mathbb{S}^2_{\text{Euc}}$, given in Eq. (3).

38-equation The extremal surface Σ_A is determined by requiring the trace of the extrinsic curvature along each normal direction n^i to vanish separately. Explicitly, $K^i = h^{\mu\nu} K_{\mu\nu}^i = h^{\mu\nu} \partial_\mu \nabla_\nu n^i$, where $h_{\mu\nu}$ is the induced metric, ∂_μ its projector, and ∇_ν the independent spacelike and timelike normals to the codimension-two surface Σ_A . Using the embedding function $n_i = t_0(\tau, \Omega_{d-2})$ for the

B.5 Uni-Parser Case Study

Original Document

丁基亚磺酰胺反应得到中间体  再将该中间体与烷基试剂后,进一步与

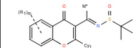
$Y-R^b$ 进行亲核反应得到通式(I)的化合物;或将式(6)的中间体经氟基化,再水解后与 NH_2-R^b 缩合得到通式(I)的化合物等。

[0078] 其中, Cy^1 , R^2 , R^3 , R^4 , R^5 , m 具有通式I中的含义; R^a 表示氢; M 表示烷基, 优选为 C_{1-6} 烷基, 进一步优选为 C_{1-3} 烷基; M' 表示 M 的一个 H 被 X 取代后的亚烷基; M'' 表示 M 去掉一个碳原子后的剩余基团, 当 M 为甲基时, M' 表示 H , X, Y 表示卤素, 优选为氯、溴、碘。

[0079] 2, Y 为 $N(R^b)$ 的通式I化合物的制备:

Uni-Parser

丁基亚磺酰胺反应得到中间体



再将该中间体与烷基试剂后,进一步与 $Y-R^b$ 进行亲核反应得到通式(I)的化合物;或将式(6)的中间体经氟基化,再水解后与 NH_2-R^b 缩合得到通式(I)的化合物等。

[0078] 其中, Cy^1 , R^2 , R^3 , R^4 , R^5 , m 具有通式I中的含义; R^a 表示氢; M 表示烷基, 优选为 C_{1-6} 烷基, 进一步优选为 C_{1-3} 烷基; M' 表示 M 的一个 H 被 X 取代后的亚烷基; M'' 表示 M 去掉一个碳原子后的剩余基团, 当 M 为甲基时, M' 表示 H ; X, Y 表示卤素, 优选为氯、溴、碘。

[0079] 2, Y 为 $N(R^b)$ 的通式I化合物的制备:

PP-StructureV3

(R^1)

丁基亚磺酰胺反应得到中间体

再将该中间体与烷基试剂后,进一步与

$Y-R^b$ 进行亲核反应得到通式(I)的化合物;或将式(6)的中间体经氟基化,再水解后与 NH_2-R^b 缩合得到通式(I)的化合物等。

[0078] 其中, Cy^1 , R^2 , R^3 , R^4 , R^5 , m 具有通式I中的含义; R^a 表示氢; M 表示烷基, 优选为 C_{1-6} 烷基, 进一步优选为 C_{1-3} 烷基; M' 表示 M 的一个 H 被 X 取代后的亚烷基; M'' 表示 M 去掉一个碳原子后的剩余基团, 当 M 为甲基时, M' 表示 H ; X, Y 表示卤素, 优选为氯、溴、碘。

[0079] 2, Y 为 $N(R^b)$ 的通式I化合物的制备:

MinerU2.5

丁基亚磺酰胺反应得到中间体 $(R^1)_m - (O^1)_n - (M^1)_p$ 再将该中间体与烷基试剂后,进一步与

$Y-R^b$ 进行亲核反应得到通式(I)的化合物;或将式(6)的中间体经氟基化,再水解后与 NH_2-R^b 缩合得到通式(I)的化合物等。

[0078] 其中, Cy^1 , R^2 , R^3 , R^4 , R^5 , m 具有通式I中的含义; R^a 表示氢; M 表示烷基, 优选为 C_{1-6} 烷基, 进一步优选为 C_{1-3} 烷基; M' 表示 M 的一个 H 被 X 取代后的亚烷基; M'' 表示 M 去掉一个碳原子后的剩余基团, 当 M 为甲基时, M' 表示 H ; X, Y 表示卤素, 优选为氯、溴、碘。

[0079] 2, Y 为 $N(R^b)$ 的通式I化合物的制备:

Original Document

WO 2016/01494

PCT/US2015/04915

Table 1. Selected examples of the compounds

Example	Structure	Name
1		N-(5-((4-ethylpiperazin-1-yl)methyl)pyridin-2-yl)-5-fluoro-4-(3-isopropyl-2-methyl-2H-indazol-5-yl)pyrimidin-2-amine
2		N-(5-((4-ethylpiperazin-1-yl)methyl)pyridin-2-yl)-5-fluoro-4-(7-fluoro-3-isopropyl-2-methyl-2H-indazol-5-yl)pyrimidin-2-amine
3		N-(5-((4-ethylpiperazin-1-yl)methyl)pyridin-2-yl)-4-(7-fluoro-3-isopropyl-2-methyl-2H-indazol-5-yl)pyrimidin-2-amine
4		4-(3-cyclopentyl-2-methyl-2H-indazol-5-yl)-N-(5-((4-ethylpiperazin-1-yl)methyl)pyridin-2-yl)-5-fluoropyrimidin-2-amine
5		4-(3-cyclopentyl-7-fluoro-2-methyl-2H-indazol-5-yl)-N-(5-((4-ethylpiperazin-1-yl)methyl)pyridin-2-yl)-5-fluoropyrimidin-2-amine

25

Uni-Parser

Table 1. Selected examples of the compounds

Example Structure	Name
1	N-(5-((4-ethylpiperazin-1-yl)methyl)pyridin-2-yl)-5-fluoro-4-(3-isopropyl-2-methyl-2H-indazol-5-yl)pyrimidin-2-amine
2	N-(5-((4-ethylpiperazin-1-yl)methyl)pyridin-2-yl)-5-fluoro-4-(7-fluoro-3-isopropyl-2-methyl-2H-indazol-5-yl)pyrimidin-2-amine
3	N-(5-((4-ethylpiperazin-1-yl)methyl)pyridin-2-yl)-4-(7-fluoro-3-isopropyl-2-methyl-2H-indazol-5-yl)pyrimidin-2-amine
4	4-(3-cyclopentyl-2-methyl-2H-indazol-5-yl)-N-(5-((4-ethylpiperazin-1-yl)methyl)pyridin-2-yl)-5-fluoropyrimidin-2-amine
5	4-(3-cyclopentyl-7-fluoro-2-methyl-2H-indazol-5-yl)-N-(5-((4-ethylpiperazin-1-yl)methyl)pyridin-2-yl)-5-fluoropyrimidin-2-amine

PP-StructureV3

Table 1. Selected examples of the compounds

Example	Structure	Name
1	F N N N N N H H N Me- Me Me	N-(5-((4-ethylpiperazin-1-yl)methyl)pyridin-2-yl)-5-fluoro-4-(3-isopropyl-2-methyl-2H-indazol-5-yl)pyrimidin-2-amine
2	F N N N F E T H H N 1 Me- Me Me	N-(5-((4-ethylpiperazin-1-yl)methyl)pyridin-2-yl)-5-fluoro-4-(7-fluoro-3-isopropyl-2-methyl-2H-indazol-5-yl)pyrimidin-2-amine
3	N N N F E H H N T Me- Me Me	N-(5-((4-ethylpiperazin-1-yl)methyl)pyridin-2-yl)-4-(7-fluoro-3-isopropyl-2-methyl-2H-indazol-5-yl)pyrimidin-2-amine
4	F N N N E H H H N N 1 Me	4-(3-cyclopentyl-2-methyl-2H-indazol-5-yl)-N-(5-((4-ethylpiperazin-1-yl)methyl)pyridin-2-yl)-5-fluoropyrimidin-2-amine
5	F N N N F E T H H 2- \S Me	4-(3-cyclopentyl-7-fluoro-2-methyl-2H-indazol-5-yl)-N-(5-((4-ethylpiperazin-1-yl)methyl)pyridin-2-yl)-5-fluoropyrimidin-2-amine

MinerU2.5

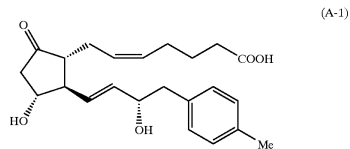
Table 1. Selected examples of the compounds

Example Structure	Name
1	N-(5-((4-ethylpiperazin-1-yl)methyl)pyridin-2-yl)-5-fluoro-4-(3-isopropyl-2-methyl-2H-indazol-5-yl)pyrimidin-2-amine
2	N-(5-((4-ethylpiperazin-1-yl)methyl)pyridin-2-yl)-5-fluoro-4-(7-fluoro-3-isopropyl-2-methyl-2H-indazol-5-yl)pyrimidin-2-amine
3	N-(5-((4-ethylpiperazin-1-yl)methyl)pyridin-2-yl)-4-(7-fluoro-3-isopropyl-2-methyl-2H-indazol-5-yl)pyrimidin-2-amine
4	4-(3-cyclopentyl-2-methyl-2H-indazol-5-yl)-N-(5-((4-ethylpiperazin-1-yl)methyl)pyridin-2-yl)-5-fluoropyrimidin-2-amine
5	4-(3-cyclopentyl-7-fluoro-2-methyl-2H-indazol-5-yl)-N-(5-((4-ethylpiperazin-1-yl)methyl)pyridin-2-yl)-5-fluoropyrimidin-2-amine

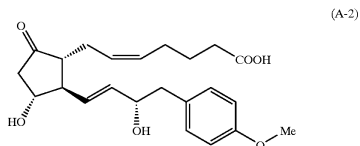
Original Document

3

Example 55:



Example 72:



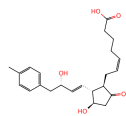
DISCLOSURE OF THE PRESENT INVENTION

The present invention consists in, as described hereafter, the fact that the present inventors have found that PGE compounds in which the ω -chain includes phenyl group substituted by particular substituents bind strongly on EP_4 and bind weakly on the other PG receptors including other subtypes than EP_4 . In other words, the present inventors have found that adoption of particular groups maintained EP_4 activity and the selectivity for EP_4 over other receptors is improved, to complete the invention.

Uni-Parser

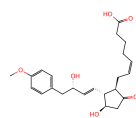
Example 55:

(A-1)



Example 72:

(A-2)

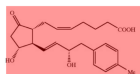


DISCLOSURE OF THE PRESENT INVENTION

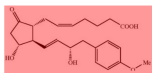
The present invention consists in, as described hereafter, the fact that the present inventors have found that PGE compounds in which the ω -chain includes phenyl group substituted by particular substituents bind strongly on EP_4 and bind weakly on the other PG receptors including other subtypes than EP_4 . In other words, the present inventors have found that adoption of particular groups maintained EP_4 activity and the selectivity for EP_4 over other receptors is improved, to complete the invention.

PP-StructureV3

Example 55:



Example 72:



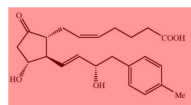
The present invention consists in, as described hereafter, the fact that the present inventors have found that PGE compounds in which the ω -chain includes phenyl group substituted by particular substituents bind strongly on EP_4 and bind weakly on the other PG receptors including other subtypes than EP_4 . In other words, the present inventors have found that adoption of particular groups maintained EP_4 activity and the selectivity for EP_4 over other receptors is improved, to complete the invention.

MinerU2.5

3

Example 55:

(A-1)



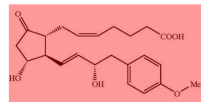
5

10

Example 72:

(A-2)

15



20

DISCLOSURE OF THE PRESENT INVENTION

25

The present invention consists in, as described hereafter, the fact that the present inventors have found that PGE compounds in which the ω -chain includes phenyl group substituted by particular substituents bind strongly on EP_4 and bind weakly on the other PG receptors including other subtypes than EP_4 . In other words, the present inventors have found that adoption of particular groups maintained EP_4 activity and the selectivity for EP_4 over other receptors is improved, to complete the invention.

INTRODUCTION

Methylenomycin A (1) is an unusual antibiotic produced by the model Actinomycete *Streptomyces coelicolor* A3(2) (Figure 1),¹⁻³ with a wide spectrum of antibiotic activity, including against diverse Gram-positive bacteria and Gram-negative *Proteus* spp.⁴ The structurally related metabolites methylenomycin C (2), methylenomycin B (3) and xanthocidin (4) (Figure 1) have been isolated from several *Streptomyces* spp.⁵⁻⁷

Incorporation experiments with isotope-labeled precursors have identified the metabolic origin of the methylenomycins

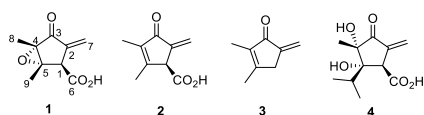
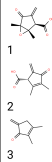


Figure 1. Structures of methylenomycin A (1), methylenomycin C (2), methylenomycin B (3), and xanthocidin (4).

INTRODUCTION

Methylenomycin A (1) is an unusual antibiotic produced by the model Actinomycete *Streptomyces coelicolor* A3(2) (Figure 1)¹⁻³ with a wide spectrum of antibiotic activity, including against diverse Gram-positive bacteria and Gram-negative *Proteus* spp.⁴ The structurally related metabolites methylenomycin C (2), methylenomycin B (3) and xanthocidin (4) (Figure 1) have been isolated from several *Streptomyces* spp.⁵⁻⁷

Incorporation experiments with isotope-labeled precursors have identified the metabolic origin of the methylenomycin



4 Figure 1. Structures of methylenomycin A (1), methylenomycin C (2), methylenomycin B (3), and xanthocidin (4).

INTRODUCTION

Methylenomycin A (1) is an unusual antibiotic produced by the model Actinomycete *Streptomyces coelicolor* A3(2) (Figure 1),¹⁻³ with a wide spectrum of antibiotic activity, including against diverse Gram-positive bacteria and Gram-negative *Proteus* spp.⁴ The structurally related metabolites methylenomycin C (2), methylenomycin B (3) and xanthocidin (4) (Figure 1) have been isolated from several *Streptomyces* spp.⁵⁻⁷

Incorporation experiments with isotope-labeled precursors have identified the metabolic origin of the methylenomycins

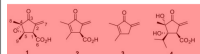


Figure 1. Structures of methylenomycin A (1), methylenomycin C (2), methylenomycin B (3), and xanthocidin (4).

INTRODUCTION

Methylenomycin A (1) is an unusual antibiotic produced by the model Actinomycete *Streptomyces coelicolor* A3(2) (Figure 1),¹⁻³ with a wide spectrum of antibiotic activity, including against diverse Gram-positive bacteria and Gram-negative *Proteus* spp.⁴ The structurally related metabolites methylenomycin C (2), methylenomycin B (3) and xanthocidin (4) (Figure 1) have been isolated from several *Streptomyces* spp.⁵⁻⁷

Incorporation experiments with isotope-labeled precursors have identified the metabolic origin of the methylenomycins



1



2



3



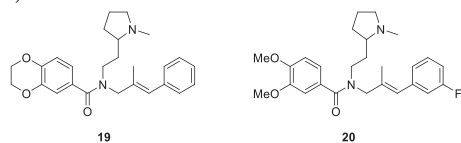
4

Figure 1. Structures of methylenomycin A (1), methylenomycin C (2), methylenomycin B (3), and xanthocidin (4).

ACS Medicinal Chemistry Letters

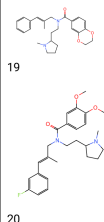
detection of the proximity of the fluorescent ligands to an N-terminal NanoLuciferase-tagged receptor (NLuc-ACKR3) by means of bioluminescence resonance energy transfer (NanoBRET).²⁰ The three fluorescent conjugates produced clear saturable specific binding to the NLuc-ACKR3 receptor that was associated with low levels of nonspecific binding (determined in the presence of unlabeled (R)-1) resulting in pK_d values ranging from 6.8 to 7.9 (Figure 3 and Table 1).

To further evaluate the use of 18a in the NanoBRET-ligand binding assay, affinities of ACKR3 ligands 4, 9, 19, and 20 were determined in competition binding experiments (Table 2).



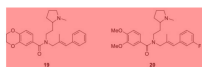
detection of the proximity of the fluorescent ligands to an N-terminal NanoLuciferase-tagged receptor (NLuc-ACKR3) by means of bioluminescence resonance energy transfer (NanoBRET).²⁰ The three fluorescent conjugates produced clear saturable specific binding to the NLuc-ACKR3 receptor that was associated with low levels of nonspecific binding (determined in the presence of unlabeled (R)-1) resulting in pK_d values ranging from 6.8 to 7.9 (Figure 3 and Table 1).

To further evaluate the use of 18a in the NanoBRET-ligand binding assay, affinities of ACKR3 ligands 4, 9, 19, and 20 were determined in competition binding experiments (Table 2).



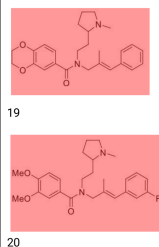
detection of the proximity of the fluorescent ligands to an N-terminal NanoLuciferase-tagged receptor (NLuc-ACKR3) by means of bioluminescence resonance energy transfer (NanoBRET).²⁰ The three fluorescent conjugates produced clear saturable specific binding to the NLuc-ACKR3 receptor that was associated with low levels of nonspecific binding (determined in the presence of unlabeled (R)-1) resulting in pK_d values ranging from 6.8 to 7.9 (Figure 3 and Table 1).

To further evaluate the use of 18a in the NanoBRET-ligand binding assay, affinities of ACKR3 ligands 4, 9, 19, and 20 were determined in competition binding experiments (Table 2).



detection of the proximity of the fluorescent ligands to an N-terminal NanoLuciferase-tagged receptor (NLuc-ACKR3) by means of bioluminescence resonance energy transfer (NanoBRET).²⁰ The three fluorescent conjugates produced clear saturable specific binding to the NLuc-ACKR3 receptor that was associated with low levels of nonspecific binding (determined in the presence of unlabeled (R)-1) resulting in pK_d values ranging from 6.8 to 7.9 (Figure 3 and Table 1).

To further evaluate the use of 18a in the NanoBRET-ligand binding assay, affinities of ACKR3 ligands 4, 9, 19, and 20 were determined in competition binding experiments (Table 2).



欲望失序：社会性别视角下泥塑粉的媒介实践考察

程丽梅
(北京印刷学院, 北京, 102600)

【摘要】在新技术不断迭代的背景下, 粉丝的主体地位不断提升, 出现了不同的粉丝类型。泥塑粉赋予男性艺人女性气质, 将其想象为女性形象, 由此获得追星愉悦。随着社会性别文化的开放与变迁, 争夺话语权中心话语权的激烈讨论, 这种对男艺人的性别倒置想象逐渐出圈, 泥塑粉从角落走向舞台, 争夺话语权中心话语权。泥塑行为看似逆转了传统凝视地位, 实际没有改变单向的权力结构, 反而被商业资本利用裹挟, 无法逃脱传统性别结构禁锢, 固化了性别认知的刻板印象。

【关键词】社会性别理论; 泥塑文化; 凝视理论; 性别认知

一、绪论

(一) 研究背景

随着新媒体技术的不断迭代升级, 粉丝的主体地位不断提升, 可以通过打投等方式参与式造星, 拥有更大的话语权。粉丝与明星、资本之间的权力关系也进一步被重构, 粉丝群体并不是一味被动接受的扁平客体, 他们的喜好和意见反过来主动影响了上游的明星和制作公司的演艺活动, 而且粉丝内部也不是同质孤立的个体, 根据圈层规则和喜爱方式也细分为不同类型。近年来走入大众视野的“泥塑”现象正是这样一种由泥塑粉构成的独特“文化景观”。

“泥塑粉”是“逆苏粉”的谐音, 与谐音“整肃”的“正苏粉”相对, 广义上是指忽略或者模糊艺人的生理性别, 将其想象为与实际相反的生理性别的二次塑造行为。狭义则指的是赋予男性艺人女性气质, 将其想象为女性形象, 由此获得追星愉悦的粉丝群体。这部分粉丝热衷于将男明星女化, 称呼男明星为“老婆”、“女儿”、“妹妹”等, 积极参与“泥塑”文本创作, 与粉丝群体内的“整肃党”经常产生冲突, 被要求“圈地自萌”。随着社会性别文化的开放与变迁, 大众对性别议题的激烈讨论, 这种对男艺人的性别倒置想象逐渐出圈, 泥塑粉从角落走向舞台, 争夺话语权中心话语权。由于这种性别倒置想象与主流性别话语体系矛盾激烈, 大众对泥塑粉的认知也不可避免地存在隔阂与误解。

(二) 研究目的和意义

本文的研究目的是考察泥塑粉媒介实践活动, 从社会性别视角出发探讨泥塑行为作为性别政治实践积极与否, 从而使对泥塑群体的认知和了解更加丰富。作为新潮的青年亚文化现象, 目前学界对于泥塑粉的研究较少, 本研究的意义一是丰富了社群研究的类型, 第二, 这种粉丝与男艺人之间单次、双重的性别倒置, 在性别研究领域也颇具新意。同时本研究的应用意义是为健康积极引导饭圈粉丝生态, 科学管理提供参考。

(三) 研究方法思路

本文主要使用了文本分析法、参与式观察法等研究方法。首先, 笔者选择微博 ID “@内娱泥塑bot”和“@韩圈泥塑bot”中2021年部分博文作为分析材料, 共计111条, 5649字。通过搜索“妈咪”、“泥塑”等关键词的微博广场, 观察泥塑粉发布的动态。

欲望失序：社会性别视角下泥塑粉的媒介实践考察

程丽梅
(北京印刷学院, 北京, 102600)

【摘要】在新技术不断迭代的背景下, 粉丝的主体地位不断提升, 出现了不同的粉丝类型。泥塑粉赋予男性艺人女性气质, 将其想象为女性形象, 由此获得追星愉悦。随着社会性别文化的开放与变迁, 大众对性别议题的激烈讨论, 这种对男艺人的性别倒置想象逐渐出圈, 泥塑粉从角落走向舞台, 争夺话语权中心话语权。泥塑行为看似逆转了传统凝视地位, 实际没有改变单向的权力结构, 反而被商业资本利用裹挟, 无法逃脱传统性别结构禁锢, 固化了性别认知的刻板印象。

【关键词】社会性别理论; 泥塑文化; 凝视理论; 性别认知

绪论

(一) 研究背景

随着新媒体技术的不断迭代升级, 粉丝的主体地位不断提升, 可以通过打投等方式参与式造星, 拥有更大的话语权。粉丝与明星、资本之间的权力关系也进一步被重构, 粉丝群体并不是一味被动接受的扁平客体, 他们的喜好和意见反过来主动影响了上游的明星和制作公司的演艺活动, 而且粉丝内部也不是同质孤立的个体, 根据圈层规则和喜爱方式也细分为不同类型。近年来走入大众视野的“泥塑”现象正是这样一种由泥塑粉构成的独特“文化景观”。

“泥塑粉”是“逆苏粉”的谐音, 与谐音“整肃”的“正苏粉”相对, 广义上是指忽略或者模糊艺人的生理性别, 将其想象为与实际相反的生理性别的二次塑造行为。狭义则指的是赋予男性艺人女性气质, 将其想象为女性形象, 由此获得追星愉悦的粉丝群体。这部分粉丝热衷于将男明星女化, 称呼男明星为“老婆”、“女儿”、“妹妹”等, 积极参与“泥塑”文本创作, 与粉丝群体内的“整肃党”经常产生冲突, 被要求“圈地自萌”。随着社会性别文化的开放与变迁, 大众对性别议题的激烈讨论, 这种对男艺人的性别倒置想象逐渐出圈, 泥塑粉从角落走向舞台, 争夺话语权中心话语权。由于这种性别倒置想象与主流性别话语体系矛盾激烈, 大众对泥塑粉的认知也不可避免地存在隔阂与误解。

(二) 研究目的和意义

本文的研究目的是考察泥塑粉媒介实践活动, 从社会性别视角出发探讨泥塑行为作为性别政治实践积极与否, 从而使对泥塑群体的认知和了解更加丰富。作为新潮的青年亚文化现象, 目前学界对于泥塑粉的研究较少, 本研究的意义一是丰富了社群研究的类型, 第二, 这种粉丝与男艺人之间单次、双重的性别倒置, 在性别研究领域也颇具新意。同时本研究的应用意义是为健康积极引导饭圈粉丝生态, 科学管理提供参考。

(三) 研究方法思路

本文主要使用了文本分析法、参与式观察法等研究方法。首先, 笔者选择微博 ID “@内娱泥塑bot”和“@韩圈泥塑bot”中2021年部分博文作为分析材料, 共计111条, 5649字。通过搜索“妈咪”、“泥塑”等关键词的微博广场, 观察泥塑粉发布的动态。

欲望失序：社会性别视角下泥塑粉的媒介实践考察

程丽梅
(北京印刷学院, 北京, 102600)

【摘要】在新技术不断迭代的背景下, 粉丝的主体地位不断提升, 出现了不同的粉丝类型。泥塑粉赋予男性艺人女性气质, 将其想象为女性形象, 由此获得追星愉悦。随着社会性别文化的开放与变迁, 大众对性别议题的激烈讨论, 这种对男艺人的性别倒置想象逐渐出圈, 泥塑粉从角落走向舞台, 争夺话语权中心话语权。泥塑行为看似逆转了传统凝视地位, 实际没有改变单向的权力结构, 反而被商业资本利用裹挟, 无法逃脱传统性别结构禁锢, 固化了性别认知的刻板印象。

【关键词】社会性别理论; 泥塑文化; 凝视理论; 性别认知

一、绪论

(一) 研究背景

随着新媒体技术的不断迭代升级, 粉丝的主体地位不断提升, 可以通过打投等方式参与式造星, 拥有更大的话语权。粉丝与明星、资本之间的权力关系也进一步被重构, 粉丝群体并不是一味被动接受的扁平客体, 他们的喜好和意见反过来主动影响了上游的明星和制作公司的演艺活动, 而且粉丝内部也不是同质孤立的个体, 根据圈层规则和喜爱方式也细分为不同类型。近年来走入大众视野的“泥塑”现象正是这样一种由泥塑粉构成的独特“文化景观”。

“泥塑粉”是“逆苏粉”的谐音, 与谐音“整肃”的“正苏粉”相对, 广义上是指忽略或者模糊艺人的生理性别, 将其想象为与实际相反的生理性别的二次塑造行为。狭义则指的是赋予男性艺人女性气质, 将其想象为女性形象, 由此获得追星愉悦的粉丝群体。这部分粉丝热衷于将男明星女化, 称呼男明星为“老婆”、“女儿”、“妹妹”等, 积极参与“泥塑”文本创作, 与粉丝群体内的“整肃党”经常产生冲突, 被要求“圈地自萌”。随着社会性别文化的开放与变迁, 大众对性别议题的激烈讨论, 这种对男艺人的性别倒置想象逐渐出圈, 泥塑粉从角落走向舞台, 争夺话语权中心话语权。由于这种性别倒置想象与主流性别话语体系矛盾激烈, 大众对泥塑粉的认知也不可避免地存在隔阂与误解。

(二) 研究目的和意义

本文的研究目的是考察泥塑粉媒介实践活动, 从社会性别视角出发探讨泥塑行为作为性别政治实践积极与否, 从而使对泥塑群体的认知和了解更加丰富。作为新潮的青年亚文化现象, 目前学界对于泥塑粉的研究较少, 本研究的意义一是丰富了社群研究的类型, 第二, 这种粉丝与男艺人之间单次、双重的性别倒置, 在性别研究领域也颇具新意。同时本研究的应用意义是为健康积极引导饭圈粉丝生态, 科学管理提供参考。

(三) 研究方法思路

本文主要使用了文本分析法、参与式观察法等研究方法。首先, 笔者选择微博 ID “@内娱泥塑bot”和“@韩圈泥塑bot”中2021年部分博文作为分析材料, 共计111条, 5649字。通过搜索“妈咪”、“泥塑”等关键词的微博广场, 观察泥塑粉发布的动态。

欲望失序：社会性别视角下泥塑粉的媒介实践考察

程丽梅
(北京印刷学院, 北京, 102600)

【摘要】在新技术不断迭代的背景下, 粉丝的主体地位不断提升, 出现了不同的粉丝类型。泥塑粉赋予男性艺人女性气质, 将其想象为女性形象, 由此获得追星愉悦。随着社会性别文化的开放与变迁, 大众对性别议题的激烈讨论, 这种对男艺人的性别倒置想象逐渐出圈, 泥塑粉从角落走向舞台, 争夺话语权中心话语权。泥塑行为看似逆转了传统凝视地位, 实际没有改变单向的权力结构, 反而被商业资本利用裹挟, 无法逃脱传统性别结构禁锢, 固化了性别认知的刻板印象。

【关键词】社会性别理论; 泥塑文化; 凝视理论; 性别认知

一、绪论

(一) 研究背景

随着新媒体技术的不断迭代升级, 粉丝的主体地位不断提升, 可以通过打投等方式参与式造星, 拥有更大的话语权。粉丝与明星、资本之间的权力关系也进一步被重构, 粉丝群体并不是一味被动接受的扁平客体, 他们的喜好和意见反过来主动影响了上游的明星和制作公司的演艺活动, 而且粉丝内部也不是同质孤立的个体, 根据圈层规则和喜爱方式也细分为不同类型。近年来走入大众视野的“泥塑”现象正是这样一种由泥塑粉构成的独特“文化景观”。

“泥塑粉”是“逆苏粉”的谐音, 与谐音“整肃”的“正苏粉”相对, 广义上是指忽略或者模糊艺人的生理性别, 将其想象为与实际相反的生理性别的二次塑造行为。狭义则指的是赋予男性艺人女性气质, 将其想象为女性形象, 由此获得追星愉悦的粉丝群体。这部分粉丝热衷于将男明星女化, 称呼男明星为“老婆”、“女儿”、“妹妹”等, 积极参与“泥塑”文本创作, 与粉丝群体内的“整肃党”经常产生冲突, 被要求“圈地自萌”。随着社会性别文化的开放与变迁, 大众对性别议题的激烈讨论, 这种对男艺人的性别倒置想象逐渐出圈, 泥塑粉从角落走向舞台, 争夺话语权中心话语权。由于这种性别倒置想象与主流性别话语体系矛盾激烈, 大众对泥塑粉的认知也不可避免地存在隔阂与误解。

(二) 研究目的和意义

本文的研究目的是考察泥塑粉媒介实践活动, 从社会性别视角出发探讨泥塑行为作为性别政治实践积极与否, 从而使对泥塑群体的认知和了解更加丰富。作为新潮的青年亚文化现象, 目前学界对于泥塑粉的研究较少, 本研究的意义一是丰富了社群研究的类型, 第二, 这种粉丝与男艺人之间单次、双重的性别倒置, 在性别研究领域也颇具新意。同时本研究的应用意义是为健康积极引导饭圈粉丝生态, 科学管理提供参考。

(三) 研究方法思路

本文主要使用了文本分析法、参与式观察法等研究方法。首先, 笔者选择微博 ID “@内娱泥塑bot”和“@韩圈泥塑bot”中2021年部分博文作为分析材料, 共计111条, 5649字。通过搜索“妈咪”、“泥塑”等关键词的微博广场, 观察泥塑粉发布的动态。

A Mexican hat dance: clustering in Ricker-potential particle systems

D. Sabio-Miller*
University of Michigan, Center for the Study of Complex Systems
D. Abrams
Northwestern University, Engineering Sciences and Applied Mathematics

The dynamics and spontaneous organization of coupled particles is a classic problem in modeling and applied mathematics. Here we examine the behavior of particles coupled by the Ricker potential, exhibiting finite local repulsion transitioning to distal attraction, leading to an energy-minimizing "preferred distance". When compressed by a background potential well of varying severity, these particles exhibit intrinsic self-organization into "stacks" with varying sizes and positions. We examine bifurcations of these high-dimensional arrangements, yielding surprising glimpses into a rich dynamical zoo of behavior.

I. INTRODUCTION

Systems of coupled particles are a classic problem in physics and applied mathematics (e.g., [1-4] and many others). Here we investigate particles interacting via short-distance repulsion and long-distance attraction, often referred to as a "Mexican hat" potential (see Fig. 1). This qualitative scenario is seen in intermolecular forces and can be modeled via, e.g., the Lennard-Jones and Morse potentials.

Local repulsion and distal attraction may call to mind the Lennard-Jones and Morse potentials from physics (see section A2). These models for intermolecular potential energy have features rendering them distinct from our Ricker wavelet: infinite repulsion in the case of Lennard-Jones, and a "sharp" non-differentiable peak at the origin for Morse. However, these models may not be applicable in situations where coexistence at the same position is allowed, due to their nonphysical implications at r=0. However, we believe a "smoothing" of the Morse potential's central peak (such as by integration against a "blurring" kernel function) would cause qualitatively similar results to what we observe in our Ricker system, and it is possible other "soft-core" potential systems (e.g., [6-8]) could find our results applicable. The smooth and coexistence-friendly dynamic embodied by our Ricker wavelet may also apply to neuronal phase models under proper conditions (e.g., [9-11]).

II. THE MODIFIED RICKER POTENTIAL

We use a modified form of the Ricker wavelet as the potential function carried or "worn" by each particle,

U(x) = [1 - exp(-k/2 * (x/s)^2)] * exp(-x^2/l^2) (1)

*dsabio@umich.edu

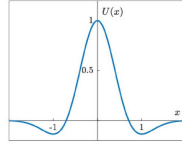


FIG. 1: Ricker wavelet, interaction potential U(x) for a particle described by the Ricker wavelet potential (Eq. (1)) with parameters s = 1 and k = 2.

which is pictured in Fig. 1.

This function has the following properties:

- 1. Central peak at (0, 1)
2. Symmetric troughs (i.e., local minima) at x = ±s
3. Trough depth controlled by k ∈ [0, ∞): as k → 1+, trough depth → ∞, and as k → ∞, trough depth → 0

Due to the central hump and symmetric troughs, this potential provides short-range, finite repulsion coupled with long-range attraction to a "preferred separation" s.

The potential at position x due to a particle at position xi is

U(x, xi) = [1 - exp(-k/2 * ((x-xi)/s)^2)] * exp(-(x-xi)^2/l^2) (2)

We suppose that n particles, indexed 1 through n, have one-dimensional positions xi and influence each other through their modified Ricker potential via the first order dynamical

A Mexican hat dance: clustering in Ricker-potential particle systems

D. Sabio-Miller*
University of Michigan, Center for the Study of Complex Systems
D. Abrams
Northwestern University, Engineering Sciences and Applied Mathematics

The dynamics and spontaneous organization of coupled particles is a classic problem in modeling and applied mathematics. Here we examine the behavior of particles coupled by the Ricker potential, exhibiting finite local repulsion transitioning to distal attraction, leading to an energy-minimizing "preferred distance". When compressed by a background potential well of varying severity, these particles exhibit intrinsic self-organization into "stacks" with varying sizes and positions. We examine bifurcations of these high-dimensional arrangements, yielding surprising glimpses into a rich dynamical zoo of behavior.

I. INTRODUCTION

Systems of coupled particles are a classic problem in physics and applied mathematics (e.g., [1-4] and many others). Here we investigate particles interacting via short-distance repulsion and long-distance attraction, often referred to as a "Mexican hat" potential (see Fig. 1). This qualitative scenario is seen in intermolecular forces and can be modeled via, e.g., the Lennard-Jones and Morse potentials.

Local repulsion and distal attraction may call to mind the Lennard-Jones and Morse potentials from physics (see section A2). These models for intermolecular potential energy have features rendering them distinct from our Ricker wavelet: infinite repulsion in the case of Lennard-Jones, and a "sharp" non-differentiable peak at the origin for Morse. However, these models may not be applicable in situations where coexistence at the same position is allowed, due to their nonphysical implications at r=0. However, we believe a "smoothing" of the Morse potential's central peak (such as by integration against a "blurring" kernel function) would cause qualitatively similar results to what we observe in our Ricker system, and it is possible other "soft-core" potential systems (e.g., [6-8]) could find our results applicable. The smooth and coexistence-friendly dynamic embodied by our Ricker wavelet may also apply to neuronal phase models under proper conditions (e.g., [9-11]).

II. THE MODIFIED RICKER POTENTIAL

We use a modified form of the Ricker wavelet as the potential function carried or "worn" by each particle,

U(x) = [1 - exp(-k/2 * (x/s)^2)] * exp(-x^2/l^2) (1)

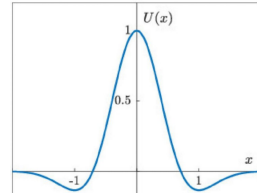


FIG. 1: Ricker wavelet, interaction potential U(x) for a particle described by the Ricker wavelet potential (Eq. (1)) with parameters s = 1 and k = 2, which is pictured in Fig. 1.

This function has the following properties:

- 1. Central peak at (0, 1)
2. Symmetric troughs (i.e., local minima) at x = ±s
3. Trough depth controlled by k ∈ [0, ∞): as k → 1+, trough depth → ∞, and as k → ∞, trough depth → 0

Due to the central hump and symmetric troughs, this potential provides short-range, finite repulsion coupled with long-range attraction to a "preferred separation" s.

The potential at position x due to a particle at position xi is

U(x, xi) = [1 - exp(-k/2 * ((x-xi)/s)^2)] * exp(-(x-xi)^2/l^2) (2)

We suppose that n particles, indexed 1 through n, have one-dimensional positions xi and influence each other through their modified Ricker potential via the first order dynamical

A Mexican hat dance: clustering in Ricker-potential particle systems

D. Sabio-Miller*
University of Michigan, Center for the Study of Complex Systems
D. Abrams
Northwestern University, Engineering Sciences and Applied Mathematics

The dynamics and spontaneous organization of coupled particles is a classic problem in modeling and applied mathematics. Here we examine the behavior of particles coupled by the Ricker potential, exhibiting finite local repulsion transitioning to distal attraction, leading to an energy-minimizing "preferred distance". When compressed by a background potential well of varying severity, these particles exhibit intrinsic self-organization into "stacks" with varying sizes and positions. We examine bifurcations of these high-dimensional arrangements, yielding surprising glimpses into a rich dynamical zoo of behavior.

I. INTRODUCTION

Systems of coupled particles are a classic problem in physics and applied mathematics (e.g., [1-4] and many others). Here we investigate particles interacting via short-distance repulsion and long-distance attraction, often referred to as a "Mexican hat" potential (see Fig. 1). This qualitative scenario is seen in intermolecular forces and can be modeled via, e.g., the Lennard-Jones and Morse potentials.

Local repulsion and distal attraction may call to mind the Lennard-Jones and Morse potentials from physics (see section A2). These models for intermolecular potential energy have features rendering them distinct from our Ricker wavelet: infinite repulsion in the case of Lennard-Jones, and a "sharp" non-differentiable peak at the origin for Morse. However, these models may not be applicable in situations where coexistence at the same position is allowed, due to their nonphysical implications at r=0. However, we believe a "smoothing" of the Morse potential's central peak (such as by integration against a "blurring" kernel function) would cause qualitatively similar results to what we observe in our Ricker system, and it is possible other "soft-core" potential systems (e.g., [6-8]) could find our results applicable. The smooth and coexistence-friendly dynamic embodied by our Ricker wavelet may also apply to neuronal phase models under proper conditions (e.g., [9-11]).

II. THE MODIFIED RICKER POTENTIAL

We use a modified form of the Ricker wavelet as the potential function carried or "worn" by each particle,

U(x) = [1 - exp(-k/2 * (x/s)^2)] * exp(-x^2/l^2) (1)

*dsabio@umich.edu

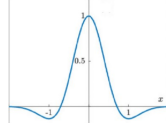


FIG. 1: Ricker wavelet, interaction potential U(x) for a particle described by the Ricker wavelet potential (Eq. (1)) with parameters s = 1 and k = 2, which is pictured in Fig. 1.

This function has the following properties:

- 1. Central peak at (0, 1)
2. Symmetric troughs (i.e., local minima) at x = ±s
3. Trough depth controlled by k ∈ [0, ∞): as k → 1+, trough depth → ∞, and as k → ∞, trough depth → 0

Due to the central hump and symmetric troughs, this potential provides short-range, finite repulsion coupled with long-range attraction to a "preferred separation" s.

The potential at position x due to a particle at position xi is

U(x, xi) = [1 - exp(-k/2 * ((x-xi)/s)^2)] * exp(-(x-xi)^2/l^2) (2)

We suppose that n particles, indexed 1 through n, have one-dimensional positions xi and influence each other through their modified Ricker potential via the first order dynamical

A Mexican hat dance: clustering in Ricker-potential particle systems

D. Sabio-Miller*
University of Michigan, Center for the Study of Complex Systems
D. Abrams
Northwestern University, Engineering Sciences and Applied Mathematics

The dynamics and spontaneous organization of coupled particles is a classic problem in modeling and applied mathematics. Here we examine the behavior of particles coupled by the Ricker potential, exhibiting finite local repulsion transitioning to distal attraction, leading to an energy-minimizing "preferred distance". When compressed by a background potential well of varying severity, these particles exhibit intrinsic self-organization into "stacks" with varying sizes and positions. We examine bifurcations of these high-dimensional arrangements, yielding surprising glimpses into a rich dynamical zoo of behavior.

I. INTRODUCTION

Systems of coupled particles are a classic problem in physics and applied mathematics (e.g., [1-4] and many others). Here we investigate particles interacting via short-distance repulsion and long-distance attraction, often referred to as a "Mexican hat" potential (see Fig. 1). This qualitative scenario is seen in intermolecular forces and can be modeled via, e.g., the Lennard-Jones and Morse potentials.

Local repulsion and distal attraction may call to mind the Lennard-Jones and Morse potentials from physics (see section A2). These models for intermolecular potential energy have features rendering them distinct from our Ricker wavelet: infinite repulsion in the case of Lennard-Jones, and a "sharp" non-differentiable peak at the origin for Morse. However, these models may not be applicable in situations where coexistence at the same position is allowed, due to their nonphysical implications at r=0. However, we believe a "smoothing" of the Morse potential's central peak (such as by integration against a "blurring" kernel function) would cause qualitatively similar results to what we observe in our Ricker system, and it is possible other "soft-core" potential systems (e.g., [6-8]) could find our results applicable. The smooth and coexistence-friendly dynamic embodied by our Ricker wavelet may also apply to neuronal phase models under proper conditions (e.g., [9-11]).

II. THE MODIFIED RICKER POTENTIAL

We use a modified form of the Ricker wavelet as the potential function carried or "worn" by each particle,

U(x) = [1 - exp(-k/2 * (x/s)^2)] * exp(-x^2/l^2) (1)

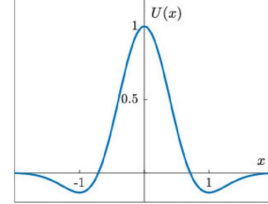


FIG. 1: Ricker wavelet, interaction potential U(x) for a particle described by the Ricker wavelet potential (Eq. (1)) with parameters s = 1 and k = 2, which is pictured in Fig. 1.

This function has the following properties:

- 1. Central peak at (0, 1)
2. Symmetric troughs (i.e., local minima) at x = ±s
3. Trough depth controlled by k ∈ [0, ∞): as k → 1+, trough depth → ∞, and as k → ∞, trough depth → 0

Due to the central hump and symmetric troughs, this potential provides short-range, finite repulsion coupled with long-range attraction to a "preferred separation" s.

The potential at position x due to a particle at position xi is

U(x, xi) = [1 - exp(-k/2 * ((x-xi)/s)^2)] * exp(-(x-xi)^2/l^2) (2)

We suppose that n particles, indexed 1 through n, have one-dimensional positions xi and influence each other through their modified Ricker potential via the first order dynamical

基于 CATIA 软件的道路三维建模方法

张波

(中国电建集团贵阳勘测设计研究院有限公司, 贵阳 550081)

【摘要】 CATIA 作为一款功能强大的三维协同设计软件在水利水电工程领域已得到广泛应用。进场道路、场内施工道路的设计是水利水电工程三维协同设计的重要组成部分, 本文根据某水电站工程进场道路的建模, 介绍了一种以二维平面设计成果为基础, 应用 CATIA 软件建立道路三维模型的方法。
【关键词】 CATIA; 道路; 三维模型; 水利水电工程; 参数化
【中图分类号】 U41 **【文献标识码】** A **【文章编号】** 1674-7461(2016)01-0071-04
【DOI】 10.16670/j.cnki.cn11-5823.tu.2016.01.12

1 引言

水利水电工程具有投资规模大、设计建设周期长、参与设计专业众多、系统构造复杂等特点。为提高设计效率和水平、增加企业核心竞争力, 水利水电设计行业正逐步完成从传统的二维平面设计到多专业三维协同设计的转变。水利水电工程建设中, 进场公路、施工道路、营地公路串联整个工程建设区, 对于一个完整的水利水电项目三维设计, 道路三维设计精度必不可少, 相比传统的平面设计仅依靠平、纵、横二维数据来表达道路的空间结构和位置, 道路三维设计精度更高, 设计成果更加直观可视。

目前, 国内外已有多种软件具备道路三维建模功能, 如德国 IB&T 软件公司的 CARD1、美国 Autodesk 公司的 AutoCAD Civil 3D、法国达索公司的 CATIA、西安经天交通工程研究所的纬地道路设计软件、南京狄诺尼科技有限责任公司开发的 EICAD、鸿业科技的鸿业 Roadleader 软件等。CARD1、纬地、EICAD、鸿业设计软件可实现道路三维模型的建立及图纸、表格资料的输出, 其利用道路几何设计的基础数据(地形数据、可建道路横断面、纵、横、竖、桥隧等构造物的三维实体模型。这三种专业的道路设计软件结合规范紧密, 具有参数化、模板功能, 在单一的道路三维建模方面具有优势。

【作者简介】 张波(1985-), 男, 工程师, 硕士, 主要研究方向: 公路、桥梁设计。

万方数据

基于 CATIA 软件的道路三维建模方法

张波

(中国电建集团贵阳勘测设计研究院有限公司, 贵阳 550081)

【摘要】 CATIA 作为一款功能强大的三维协同设计软件在水利水电工程领域已得到广泛应用。进场道路、场内施工道路的设计是水利水电工程三维协同设计的重要组成部分, 本文根据某水电站工程进场道路的建模, 介绍了一种以二维平面设计成果为基础, 应用 CATIA 软件建立道路三维模型的方法。

【关键词】 CATIA; 道路; 三维模型; 水利水电工程; 参数化

【中图分类号】 U41 **【文献标识码】** A **【文章编号】** 1674-7461(2016)01-0071-04

【DOI】 10.16670/j.cnki.cn11-5823.tu.2016.01.12

1 引言

水利水电工程具有投资规模大、设计建设周期长、参与设计专业众多、系统构造复杂等特点。为提高设计效率和水平、增加企业核心竞争力, 水利水电设计行业正逐步完成从传统的二维平面设计到多专业三维协同设计的转变。水利水电工程建设中, 进场公路、施工道路、营地公路串联整个工程建设区, 对于一个完整的水利水电项目三维设计, 道路的三维建模必不可少, 相比传统的平面设计仅依靠平、纵、横二维数据来表达道路的空间结构和位置, 道路三维设计精度更高, 设计成果更加直观可视。

目前, 国内外已有多种软件具备道路三维建模功能, 如德国 IB&T 软件公司的 CARD1、美国 Autodesk 公司的 AutoCAD Civil 3D、法国达索公司的 CATIA、西安经天交通工程研究所的纬地道路设计软件、南京狄诺尼科技有限责任公司开发的 EICAD、鸿业科技的鸿业 Roadleader 软件等。CARD1、纬地、EICAD、鸿业设计软件可实现道路三维模型的建立及图纸、表格资料的输出, 其利用道路几何设计的基础数据和地形数据, 可快速准确的构建地面、道路、桥隧等构造物的三维实体模型。这三种专业的道路设计软件结合规范紧密, 具有参数化、模板功能, 在单一的道路三维建模方面具有优势。

但这些软件的参数化关联设计及地形曲面处理功能有限^[1], 也无法满足水利水电等大型复杂工程的多专业协同设计的要求。AutoCAD Civil 3D 是一款专业的三维设计软件, 可完成道路工程、排水管网系统以及场地规划等设计, 它的道路建模功能可以将水平和垂直几何图形与定制的横断面相结合, 为公路和其它交通运输系统创建参数化定义的动态三维模型。但其在建筑模型、机电装配等设计中需结合其他软件, 在水利水电工程施工总布置三维设计中存在不足^[2]。

CATIA 是法国达索公司开发的大型高端 CAD/CAE/CAM 一体化设计软件, 其能将地质、工程枢纽、施工布置、场内交通、金属结构及机电装配等专业结合在一起进行水利水电工程三维设计, 利用其协同设计平台 VPM 可将零散的各自设计转变集中在线设计, 并实现设计模型、结构、骨架、参数、关联信息的有效管理^[3]。CATIA 具有强大的参数化设计功能及完备的知识工程功能, 可建立道路横断面、附属结构的通用模板库, 实现知识重用及模型的关联更新。由于 CATIA 软件在水利水电工程多专业协同设计以及道路三维建模方面具有诸多优势, 其已广泛应用于水利水电工程项目的总体设计中。本文根据国内某水电站项目三维协同设计中进场道路的建模, 介绍了一种以二维道路专业设计成果为基础, 应用 CATIA 软件建立道路三维模型的方法。

【作者简介】 张波(1985-), 男, 工程师, 硕士, 主要研究方向: 公路、桥梁设计。

基于 CATIA 软件的道路三维建模方法

张波

(中国电建集团贵阳勘测设计研究院有限公司, 贵阳 550081)

【摘要】 CATIA 作为一款功能强大的三维协同设计软件在水利水电工程领域已得到广泛应用。进场道路、场内施工道路的设计是水利水电工程三维协同设计的重要组成部分, 本文根据某水电站工程进场道路的建模, 介绍了一种以二维平面设计成果为基础, 应用 CATIA 软件建立道路三维模型的方法。

【关键词】 CATIA; 道路; 三维模型; 水利水电工程; 参数化

【中图分类号】 U41 **【文献标识码】** A **【文章编号】** 1674-7461(2016)01-0071-04

【DOI】 10.16670/j.cnki.cn11-5823.tu.2016.01.12

1 引言

水利水电工程具有投资规模大、设计建设周期长、参与设计专业众多、系统构造复杂等特点。为提高设计效率和水平、增加企业核心竞争力, 水利水电设计行业正逐步完成从传统的二维平面设计到多专业三维协同设计的转变。水利水电工程建设中, 进场公路、施工道路、营地公路串联整个工程建设区, 对于一个完整的水利水电项目三维设计, 道路的三维建模必不可少, 相比传统的平面设计仅依靠平、纵、横二维数据来表达道路的空间结构和位置, 道路三维设计精度更高, 设计成果更加直观可视。

目前, 国内外已有多种软件具备道路三维建模功能, 如德国 IB&T 软件公司的 CARD1、美国 Autodesk 公司的 AutoCAD Civil 3D、法国达索公司的 CATIA、西安经天交通工程研究所的纬地道路设计软件、南京狄诺尼科技有限责任公司开发的 EICAD、鸿业科技的鸿业 Roadleader 软件等。CARD1、纬地、EICAD、鸿业设计软件可实现道路三维模型的建立及图纸、表格资料的输出, 其利用道路几何设计的基础数据和地形数据, 可快速准确的构建地面、道路、桥隧等构造物的三维实体模型。这三种专业的道路设计软件结合规范紧密, 具有参数化、模板功能, 在单一的道路三维建模方面具有优势。

但这些软件的参数化关联设计及地形曲面处理功能有限^[1], 也无法满足水利水电等大型复杂工程的多专业协同设计的要求。AutoCAD Civil 3D 是一款专业的三维设计软件, 可完成道路工程、排水管网系统以及场地规划等设计, 它的道路建模功能可以将水平和垂直几何图形与定制的横断面相结合, 为公路和其它交通运输系统创建参数化定义的动态三维模型。但其在建筑模型、机电装配等设计中需结合其他软件, 在水利水电工程施工总布置三维设计中存在不足^[2]。

CATIA 是法国达索公司开发的大型高端 CAD/CAE/CAM 一体化设计软件, 其能将地质、工程枢纽、施工布置、场内交通、金属结构及机电装配等专业结合在一起进行水利水电工程三维设计, 利用其协同设计平台 VPM 可将零散的各自设计转变集中在线设计, 并实现设计模型、结构、骨架、参数、关联信息的有效管理。CATIA 具有强大的参数化设计功能及完备的知识工程功能, 可建立道路横断面、附属结构的通用模板库, 实现知识重用及模型的关联更新。由于 CATIA 软件在水利水电工程多专业协同设计以及道路三维建模方面具有诸多优势, 其已广泛应用于水利水电工程项目的总体设计中。本文根据国内某水电站项目三维协同设计中进场道路的建模, 介绍了一种以二维道路专业设计成果为基础, 应用 CATIA 软件建立道路三维模型的方法。

基于 CATIA 软件的道路三维建模方法

张波

(中国电建集团贵阳勘测设计研究院有限公司, 贵阳 550081)

【摘要】 CATIA 作为一款功能强大的三维协同设计软件在水利水电工程领域已得到广泛应用。进场道路、场内施工道路的设计是水利水电工程三维协同设计的重要组成部分, 本文根据某水电站工程进场道路的建模, 介绍了一种以二维平面设计成果为基础, 应用 CATIA 软件建立道路三维模型的方法。

【关键词】 CATIA; 道路; 三维模型; 水利水电工程; 参数化

【中图分类号】 U41 **【文献标识码】** A **【文章编号】** 1674-7461(2016)01-0071-04

【DOI】 10.16670/j.cnki.cn11-5823.tu.2016.01.12

1 引言

水利水电工程具有投资规模大、设计建设周期长、参与设计专业众多、系统构造复杂等特点。为提高设计效率和水平、增加企业核心竞争力, 水利水电设计行业正逐步完成从传统的二维平面设计到多专业三维协同设计的转变。水利水电工程建设中, 进场公路、施工道路、营地公路串联整个工程建设区, 对于一个完整的水利水电项目三维设计, 道路的三维建模必不可少, 相比传统的平面设计仅依靠平、纵、横二维数据来表达道路的空间结构和位置, 道路三维设计精度更高, 设计成果更加直观可视。

目前, 国内外已有多种软件具备道路三维建模功能, 如德国 IB&T 软件公司的 CARD1、美国 Autodesk 公司的 AutoCAD Civil 3D、法国达索公司的 CATIA、西安经天交通工程研究所的纬地道路设计软件、南京狄诺尼科技有限责任公司开发的 EICAD、鸿业科技的鸿业 Roadleader 软件等。CARD1、纬地、EICAD、鸿业设计软件可实现道路三维模型的建立及图纸、表格资料的输出, 其利用道路几何设计的基础数据和地形数据, 可快速准确的构建地面、道路、桥隧等构造物的三维实体模型。这三种专业的道路设计软件结合规范紧密, 具有参数化、模板功能, 在单一的道路三维建模方面具有优势。

但这些软件的参数化关联设计及地形曲面处理功能有限^[1], 也无法满足水利水电等大型复杂工程的多专业协同设计的要求。AutoCAD Civil 3D 是一款专业的三维设计软件, 可完成道路工程、排水管网系统以及场地规划等设计, 它的道路建模功能可以将水平和垂直几何图形与定制的横断面相结合, 为公路和其它交通运输系统创建参数化定义的动态三维模型。但其在建筑模型、机电装配等设计中需结合其他软件, 在水利水电工程施工总布置三维设计中存在不足^[2]。

CATIA 是法国达索公司开发的大型高端 CAD/CAE/CAM 一体化设计软件, 其能将地质、工程枢纽、施工布置、场内交通、金属结构及机电装配等专业结合在一起进行水利水电工程三维设计, 利用其协同设计平台 VPM 可将零散的各自设计转变集中在线设计, 并实现设计模型、结构、骨架、参数、关联信息的有效管理。CATIA 具有强大的参数化设计功能及完备的知识工程功能, 可建立道路横断面、附属结构的通用模板库, 实现知识重用及模型的关联更新。由于 CATIA 软件在水利水电工程多专业协同设计以及道路三维建模方面具有诸多优势, 其已广泛应用于水利水电工程项目的总体设计中。本文根据国内某水电站项目三维协同设计中进场道路的建模, 介绍了一种以二维道路专业设计成果为基础, 应用 CATIA 软件建立道路三维模型的方法。

Original Document

说明书 7/7页

配合物	λ_{abs}/nm	摩尔吸光系数 $Log\epsilon/M^{-1}cm^{-1}$	λ_{em}/nm (液体)	Φ (液体)	λ_{em}/nm (固体)
1	385	4.43	441	0.81	454
2	381	4.20	477	0.44	484
3	374	4.13	464	0.37	487
4	363	4.00	---	<0.01	---
5	382	3.98	482	0.13	---
6	387	4.06	492	0.37	489
7	382	4.23	464	0.57	469
8	394	4.44	458	0.96	502

[0094] 注1:光谱性质均在室温下的二氧甲烷溶液中测定;
 [0095] 注2:荧光量子产率 Φ 以硫酸奎宁($\Phi = 0.55, 0.5mM$ 硫酸水溶液)为参照物,采用稀溶液比较法进行测定。
 [0096] 由表1中数据可见,上述配合物,除酞环上含有吸电子取代基的配合物外,其余的配合物在紫外光照射下其有机溶液和固体呈现出强烈的荧光。紫外吸收波长在363nm-394nm范围,荧光发射波长在441nm-502nm范围,荧光量子产率在0.13-0.96范围。
 [0097] 当酞环上连有吸电子取代基时,配合物的荧光性削弱得十分显著,这可以从相应配合物的量子产率数据上得到体现,进而使得其固体荧光无法测量,甚至当取代基为硝基时,配合物已经完全没有了荧光性能。尽管咪唑环上引入吸电子基也引起了配合物量子产率的降低,但效果没有酞环上那么强烈。无论在咪唑环还是在酞环上,引入斥电子基都有利于配合物荧光性能的增强,但似乎酞环上的斥电子基有着更大的荧光增强效应,尤其当斥电子基处于酞氧原子的间位时。由此可见,酞环上取代基电性的变化对配合物整体荧光性能的影响更为显著。由于在酞环或咪唑环上引入取代基增大了空间位阻,使得分子间无法产生致密堆积,减小了诸如 $\pi-\pi$ 吸引等分子间相互作用,再加上大幅Stock's位移而消除了自淬灭作用,因此导致配合物产生强烈的固体荧光发射。

10

Uni-Parser

配合物	λ_{abs}/nm	摩尔吸光系数 $Log\epsilon/M^{-1}cm^{-1}$	λ_{em}/nm (液体)	Φ (液体)	λ_{em}/nm (固体)
1	385	4.43	441	0.81	454
2	381	4.20	477	0.44	484
3	374	4.13	464	0.37	487
4	363	4.00	---	<0.01	---
5	382	3.98	482	0.13	---
6	387	4.06	492	0.37	489
7	382	4.23	464	0.57	469
8	394	4.44	458	0.96	502

[0094] 注1:光谱性质均在室温下的二氧甲烷溶液中测定;
 [0095] 注2:荧光量子产率 Φ 以硫酸奎宁($\Phi = 0.55, 0.5mM$ 硫酸水溶液)为参照物,采用稀溶液比较法进行测定。
 [0096] 由表1中数据可见,上述配合物,除酞环上含有吸电子取代基的配合物外,其余的配合物在紫外光照射下其有机溶液和固体呈现出强烈的荧光。紫外吸收波长在363nm-394nm范围,荧光发射波长在441nm-502nm范围,荧光量子产率在0.13-0.96范围。

[0097] 当酞环上连有吸电子取代基时,配合物的荧光性削弱得十分显著,这可以从相应配合物的量子产率数据上得到体现,进而使得其固体荧光无法测量,甚至当取代基为硝基时,配合物已经完全没有了荧光性能。尽管咪唑环上引入吸电子基也引起了配合物量子产率的降低,但效果没有酞环上那么强烈。无论在咪唑环还是在酞环上,引入斥电子基都有利于配合物荧光性能的增强,但似乎酞环上的斥电子基有着更大的荧光增强效应,尤其当斥电子基处于酞氧原子的间位时。由此可见,酞环上取代基电性的变化对配合物整体荧光性能的影响更为显著。由于在酞环或咪唑环上引入取代基增大了空间位阻,使得分子间无法产生致密堆积,减小了诸如 $\pi-\pi$ 吸引等分子间相互作用,再加上大幅Stock's位移而消除了自淬灭作用,因此导致配合物产生强烈的固体荧光发射。

PP-StructureV3

配合物	λ_{abs}/nm	摩尔吸光系数 $Log\epsilon/M^{-1}cm^{-1}$	λ_{em}/nm (液体)	Φ (液体)	λ_{em}/nm (固体)
1	385	4.43	441	0.81	454
2	381	4.20	477	0.44	484
3	374	4.13	464	0.37	487
4	363	4.00	---	<0.01	---
5	382	3.98	482	0.13	---
6	387	4.06	492	0.37	489
7	382	4.23	464	0.57	469
8	394	4.44	458	0.96	502

[0094] 注1:光谱性质均在室温下的二氧甲烷溶液中测定;
 [0095] 注2:荧光量子产率 Φ 以硫酸奎宁($\Phi = 0.55, 0.5mM$ 硫酸水溶液)为参照物,采用稀溶液比较法进行测定。
 [0096] 由表1中数据可见,上述配合物,除酞环上含有吸电子取代基的配合物外,其余的配合物在紫外光照射下其有机溶液和固体呈现出强烈的荧光。紫外吸收波长在363nm-394nm范围,荧光发射波长在441nm-502nm范围,荧光量子产率在0.13-0.96范围。
 [0097] 当酞环上连有吸电子取代基时,配合物的荧光性削弱得十分显著,这可以从相应配合物的量子产率数据上得到体现,进而使得其固体荧光无法测量,甚至当取代基为硝基时,配合物已经完全没有了荧光性能。尽管咪唑环上引入吸电子基也引起了配合物量子产率的降低,但效果没有酞环上那么强烈。无论在咪唑环还是在酞环上,引入斥电子基都有利于配合物荧光性能的增强,但似乎酞环上的斥电子基有着更大的荧光增强效应,尤其当斥电子基处于酞氧原子的间位时。由此可见,酞环上取代基电性的变化对配合物整体荧光性能的影响更为显著。由于在酞环或咪唑环上引入取代基增大了空间位阻,使得分子间无法产生致密堆积,减小了诸如 $\pi-\pi$ 吸引等分子间相互作用,再加上大幅Stock's位移而消除了自淬灭作用,因此导致配合物产生强烈的固体荧光发射。

MinerU2.5

配合物	λ_{abs}/nm	摩尔吸光系数 $Log\epsilon/M^{-1}cm^{-1}$	λ_{em}/nm (液体)	Φ (液体)	λ_{em}/nm (固体)
1	385	4.43	441	0.81	454
2	381	4.20	477	0.44	484
3	374	4.13	464	0.37	487
4	363	4.00	---	<0.01	---
5	382	3.98	482	0.13	---
6	387	4.06	492	0.37	489
7	382	4.23	464	0.57	469
8	394	4.44	458	0.96	502

[0094] 注1:光谱性质均在室温下的二氧甲烷溶液中测定;
 [0095] 注2:荧光量子产率 Φ 以硫酸奎宁($\Phi = 0.55, 0.5mM$ 硫酸水溶液)为参照物,采用稀溶液比较法进行测定。
 [0096] 由表1中数据可见,上述配合物,除酞环上含有吸电子取代基的配合物外,其余的配合物在紫外光照射下其有机溶液和固体呈现出强烈的荧光。紫外吸收波长在363nm-394nm范围,荧光发射波长在441nm-502nm范围,荧光量子产率在0.13-0.96范围。
 [0097] 当酞环上连有吸电子取代基时,配合物的荧光性削弱得十分显著,这可以从相应配合物的量子产率数据上得到体现,进而使得其固体荧光无法测量,甚至当取代基为硝基时,配合物已经完全没有了荧光性能。尽管咪唑环上引入吸电子基也引起了配合物量子产率的降低,但效果没有酞环上那么强烈。无论在咪唑环还是在酞环上,引入斥电子基都有利于配合物荧光性能的增强,但似乎酞环上的斥电子基有着更大的荧光增强效应,尤其当斥电子基处于酞氧原子的间位时。由此可见,酞环上取代基电性的变化对配合物整体荧光性能的影响更为显著。由于在酞环或咪唑环上引入取代基增大了空间位阻,使得分子间无法产生致密堆积,减小了诸如 $\pi-\pi$ 吸引等分子间相互作用,再加上大幅Stock's位移而消除了自淬灭作用,因此导致配合物产生强烈的固体荧光发射。